Twisting, Binding, and Probing Matter Waves in a Rubidium Cavity QED System

by

Chengyi Luo

B.S., Sun Yat-sen University, 2017

A thesis submitted to the

Faculty of the Graduate School of the

University of Colorado in partial fulfillment

of the requirements for the degree of

Doctor of Philosophy

Department of Physics

2024

Committee Members:

James K. Thompson, Chair

Ana Maria Rey

Joshua Combes

Adam Kaufman

Jun Ye

Luo, Chengyi (Ph.D., Physics)

Twisting, Binding, and Probing Matter Waves in a Rubidium Cavity QED System

Thesis directed by Prof. James K. Thompson

In this thesis work, I have explored a novel platform for quantum metrology and many-body physics by realizing matter-wave interferometric controls in a high finesse cavity. By correlating the internal states of the atoms to the external degrees of freedom, we demonstrated direct entanglement generation on the momentum states of the atoms with two distinct approaches, quantum non-demolition measurement and one-axis twisting dynamics. After injecting the squeezed momentum states into a matter-wave interferometer, we realized an entanglement-enhanced matter-wave interferometer for the first time.

Decoupling the momentum states from the internal states with all atoms in the same atomic spin state, we realized a novel cavity-mediated collective momentum-exchange interaction in which pairs of atoms swap their momenta by exchanging photons through the cavity. The momentum-exchange interaction leads to an observed all-to-all Ising-like interaction in a matter-wave interferometer, which is useful for entanglement generation. A many-body energy gap also emerges, effectively binding interferometer matter-wave packets together to suppress Doppler dephasing with analogies to Mössbauer spectroscopy. In the same system, by adding new laser frequency control for driving pair creation/annihilation processes, we realized Hamiltonian engineering of collective XYZ spin models between two momentum states and the first demonstration of the long-sought two-axis counter-twisting dynamics.

The entanglement-enhanced matter-wave interferometer experiment shed new light on improving future atom interferometers by reducing the fundamental quantum source of imprecision. The momentum-exchange interaction provides new options for interacting momentum states enabled by the cavity. The Hamiltonian engineering realized here not only enables new dynamics for entanglement generation but also offers new possibilities for quantum simulation with atomic

momentum states. All these opportunities arise from coupling the atoms to a high-finesse cavity, known as cavity quantum electrodynamics systems. Combining the matter-wave interferometric control and cavity QED, our system provides a new platform for the study of quantum metrology, quantum simulation and many-body physics with qubits based on atomic momentum states.

Acknowledgements

My time in graduate school has been fun, mainly owing to James. He is for sure a fantastic (if not the best) advisor and my role model for research. I have greatly benefited from his patience. I still remember, during my first month in the lab, he would even give hands-on advise on how to turn the knobs. Later in the Ph.D., he was also very understanding when I got distracted from the original plan or when I felt like more time for dealing with technical issues. Apart from giving helpful suggestions, he would allow me with a lot of freedom by saying "Do whatever makes sense to you." I always enjoyed the moment when he came in the lab, dropped down his laptop and coffee, and said "Hey, I have an idea/question." Some of our late night discussions are now turning into actual experimental results.

Though one year younger, Dylan Young joined the group only a few months later than I did. He is undoubtedly the kindest person in the lab, and I'm very glad to have overlapped with him the most. Unfortunately, we worked on different sides of the room, it would have been so cool to directly collaborate with him. On the Rb experiment, Baochen Wu and Graham Greve are the ones who put me on track at the beginning. Vanessa Koh provided significant help with the momentum-exchange project and preparing the new lab space. I wish her all the best with her new career. Chitose Maruko joined our experiment during my last year. She is by far the brightest first-year student I have ever seen, and I regret not having more time to work with her. I'm also in debt to her for bravely taking over recovering the experiment during my unforeseen sudden absence, right after the big lab move. I believe she will be able to bring the experiment to a new level.

One unique aspect of JILA is that you get to work with brilliant theorists like Ana Maria

Rey, who has deep understanding of both theory and experiment. I'm grateful to have worked with Haoqing Zhang, Anjun Chu from Rey group and John Wilson from Murray Holland's group. In particular, I spent a lot of time discussing with Haoqing through the second half of my Ph.D.. There are even days he actually came down to the lab, watched me taking new data, readjusted his simulation and fed me new ideas. You just can't beat this bandwidth! The support from JILA machine shop is also fantastic. I would like to thank James and Calvin for such a great job with the move. To quantify how successful the move was, the lasers are still well coupled to the cavity after we turned them back on.

Before joining graduate school, I was very lucky to work with many great scientists as well. Prof. Jiahao Huang and Prof. Chaohong Lee introduced me to quantum metrology during my undergraduate studies. Jiahao was a senior Ph.D. student at the time, but he was also patient enough to give very detailed guidance on derivation and paper writing to a second-year undergraduate student. Prof. Wes Campbell offered me my first opportunity to work in an AMO lab, and his passion has influenced me to choose experiment for graduate school. During my last year in college, I had the privilege of working with Dr. Tao Shi. Although I have forgotten most of the theoretical techniques he taught me, his childlike curiosity about physics continues to inspire me.

I would like to thank my parents for their unconditional support for me to pursue research. I still remember one of the defining moments for me to choose physics as college major is when my dad handed me the public information about the 2012 Nobel prize in physics. I was mostly brought up by my grandfather who passed away a few years ago. Hopefully, I have inherited some of his qualities. They might be best described by two Cantonese catchphrases "是但啦" and "顶硬上", which roughly correspond to "be less opinionated" towards trivial things but "can bite the bullet" when facing challenges. Lastly, I would like to thank my partner Wenqin for always being encouraging, and for accompanying me through all the ups and downs of our Ph.D. times. I look forward to exploring more in life with her in the future.

Contents

Chapter

Tables

Table

Figures

Figure

Chapter 1

Motivation and overview

Wave-particle duality, the concept that matter can exhibit both particle-like or wave-like properties, plays a central role in quantum mechanics since its development. Originated from the theory for describing electrons by Louis de Broglie [2], this concept has been generalized to and verified in many systems, including cold atoms as studied in this thesis. Going beyond the study of fundamental quantum theory, matter waves are now being applied in quantum sensing [3, 4], which holds great promise for providing new insights into nature, and for searching for undiscovered physics [5, 6].

To understand how matter waves help improve measurements, it is helpful to take a moment and think about how do we measure lengths in daily life. We measure the lengths of any objects with a ruler or measuring tape by counting the ticks on the ruler. Ignoring the details about how one position the ruler and the objects, the precision of the measurements is limited by how finely and evenly spaced the ticks are. The finest spacing is typically 1 mm[1] . The need of better length measurements motivate the invention of optical interferometer [7, 8]. Visible lights have characteristic wavelengths of $\lambda \approx 1\mu$m. By separating the light into two paths and recombining them, the interference pattern changes between bright and dark when the differential path length changes by $\lambda/2$. With this new "ruler", the "ticks" are now separated by about 1μm, which is about three orders of magnitude better than almost any rulers one can buy.

With matter waves, the wavelength of a particle (de Broglie wavelength) is determined by

[1] Or 1/16 of an inch if you live in the U.S.

$\lambda = \frac{h}{mv}$, here h is the Planck constant, m and v are the mass and velocity of the particle. Take an atom as an example, for a rubidium atom moving at 5 m/s, the de Broglie wavelength is about $\lambda_{Rb} \approx 1$ nm. This is another factor of 1000 better than the optical interferometers, which indicates the potential of matter-wave interferometer for performing measurements with high precision.

Staring at the de Broglie wavelength formula, one might ask: "Wait a minute. If I throw a baseball (roughly 0.1 kg) at 10 m/s, doesn't that give me an even smaller wavelength?" The caveat is that the baseball is hot! As compared to the absolute zero, room temperature (roughly 300 °K) is hot enough such that different particles inside the baseball move at different velocities (let alone the difference in mass.) Or in other words, there are many tiny "rulers" with different tick spacing, which thus blur out the ticks and make it impossible to read. Going back to the case with atoms, in order to keep the "atomic ruler" visible, we need keep all the atoms moving at the same speed. To reduce the random motions of the atoms, we need to cool the particles down. Only after being cooled to a certain degree[2] , typically < 1 μK, can the atoms start exhibiting quantum feature.

Going into the quantum regime, an extra bonus for precision measurement is the new resource called entanglement, or *"spooky action at a distance"* according to Einstein. This is another central concept in quantum mechanics describing correlation between objects. To give an intuition for understanding the benefit, we can go back to the "atomic ruler" example. Assuming there are N atoms in an ensemble, every atom can serve as an individual ruler. When the length does not align with any tick, every individual measurement with single atom has an error of 1 mm (tick spacing.) When performing N different measurements, the uncorrelated error for individual measurement can be reduced by $\sqrt{N}$ times. Establishing entanglement between atoms can lead to correlation between measurements and reduce the error even more. For example, before every measurement, the atoms "know" the error in the former measurement and compensate it by changing its reading, and therefore can lead to even better precision.

Apart from precision measurements, the quantum mechanical features can also enable the study of quantum simulation. By designing certain properties and interactions, matter waves can

[2] Pun intended.

mimic the behaviors of quantum magnets, superconductors [9] and even black holes [10]. For both quantum metrology and simulation, we need to understand how to manipulate matter waves, how to establish interactions between different matter waves and how to perform measurements on matter waves.

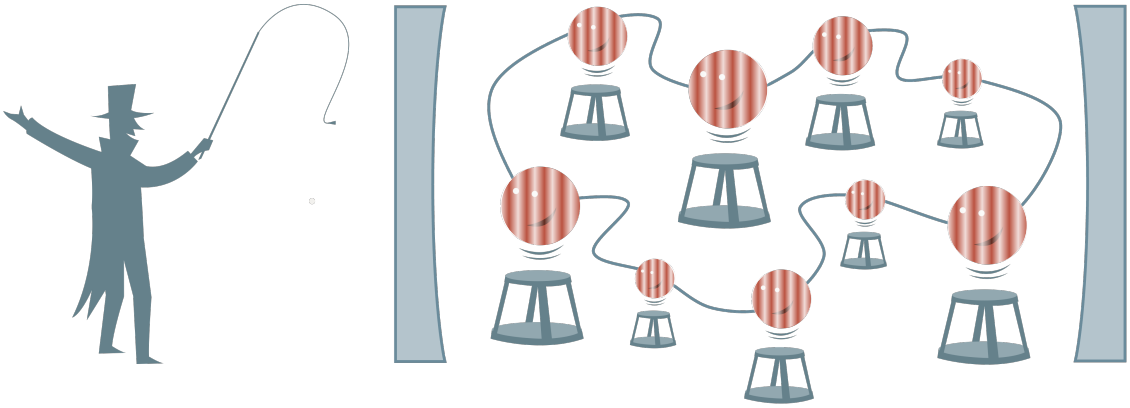

Figure 1.1: Controlling matter waves with an optical cavity. Adapted from original graphic in the public information for 2012 Nobel prize in physics [1]. In this thesis, we explore how to generate interactions between matter waves by coupling them to a high-finesse cavity formed by two mirrors.

In this thesis, I will present our approach for solving these questions with a platform in which matter waves are coupled to a high-finesse cavity. In this system, we are able to use the cavity for entangling momentum states [11][G] [3] , applying one/two-axis (counter) twisting dynamics between momentum state and binding matter-wave packets together to suppress the Doppler dephasing with a novel collective recoil mechanism [12, 13][G]. As the motivations for these experiments, in this chapter, I will start by highlighting a few concepts including quantum metrology, cavity quantum electrodynamics and matter waves by answering what they are and why they are interesting. In the end, I will give an outline of the whole thesis.

1.1 Quantum metrology

Recent developments in quantum science have enabled precision measurements assisted by quantum mechanics [14]. A classic paradigm is sensing with two-level systems. The key to the

[3] [G]: papers from the group (Thompson lab.)

precision is the encoding of information in the phase ϕ that appears in the superposition of the two levels. The two levels could be two different atomic internal states such as in atomic clocks or two momentum states in matter-wave interferometers. This phase must be estimated from quantum measurements to extract the desired information. For N atoms, the phase estimation is fundamentally limited by the independent quantum collapse of each atom to an rms angular uncertainty $\Delta\theta_{\mathrm{SQL}} = 1/\sqrt{N}$ rad known as the standard quantum limit (SQL) [15].

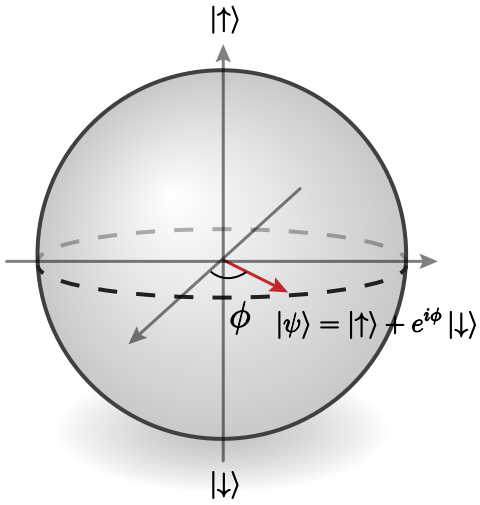

Figure 1.2: The quantum state or a two-level system represented by a Bloch vector on a Bloch sphere. The azimuthal angle on the Bloch sphere corresponds to the relative phase between the two levels.

Reducing this fundamental quantum source of imprecision would provide a new resource that can be exploited to directly enhance measurement precision, bandwidth, and accuracy or operate at reduced size. The only way to surpass the standard quantum limit set by the quantum collapse of independent atoms is to correlate atoms to each other, also known as quantum entanglement. In this thesis, I'll focus on one of the most metrologically useful entangled states, the spin squeezed state [16, 17]. Specifically, the squeezing generation between matter waves and the application in enhancing the precision of matter-wave interferometer. In Chapter 2 and Chapter 4, I will present two different approaches for generating squeezed state: one-axis twisting (OAT) dynamics and quantum non-demolition (QND) measurement. The more traditional approach for squeezing

generation is to induce a certain many-body interaction such as OAT, and let the system evolve into a entanglement state. In contrast, QND measurement takes advantage of the other aspect of quantum mechanics, by performing certain measurements on the system, one can project an un-entangled quantum state into a squeezed state. I will here give a minimal example for understanding this process.

Consider an isolated quantum system with two atoms labeled as 1 and 2, where each has two possible spin states $|\uparrow\rangle$ and $|\downarrow\rangle$. By preparing both atoms in equal superpositions of the two states $|\psi\rangle_{1,2} = \frac{|\uparrow\rangle+|\downarrow\rangle}{\sqrt{2}}$, the initial state of the system is thus

$$|\psi\rangle_i = |\psi\rangle_1 \bigotimes |\psi\rangle_2 = \frac{|\uparrow_1\uparrow_1\rangle + |\uparrow_1\downarrow_2\rangle + |\downarrow_1\uparrow_2\rangle + |\downarrow_2\downarrow_2\rangle}{2}, \tag{1.1}$$

which is a superposition of all four possible measurement outputs. Let's assume one can prepare many copies of the same quantum system and measure the atom number $N_\uparrow$ in $|\uparrow\rangle$. On average, there is only one atom in $|\uparrow\rangle$. However, each individual measurement could give $N_\uparrow$ =0, 1 and 2, resulting from the uncorrelated random collapses of the two atoms into the measurement operator projects each atoms into either $|\uparrow\rangle$ or $|\downarrow\rangle$.

Instead of directly measuring the individual state of the two particles, if one performs a pre-measurement on the system of the total atom number in $|\uparrow\rangle$ and gets a result of 1, the initial quantum state will then be projected to

$$|\psi\rangle_s = \frac{|\uparrow_1\downarrow_2\rangle + |\downarrow_1\uparrow_2\rangle}{\sqrt{2}}. \tag{1.2}$$

This is an entangled state with the two atoms always in different spin states. The second or final measurements on the system will always give $N_\uparrow = 1$ with no fluctuation.

Apart from showing how does entanglement reduce the measurement noise, this example also highlights that, squeezing with QND measurement relies on asking the right question (how many atoms in $|\uparrow\rangle$) without collapsing the whole system (which atom is in $|\uparrow\rangle$.) Later, we will show how to satisfy both requirements by using an optical cavity.

1.2 Matter waves and atom interferometry

One central concept of quantum mechanics are superposition and coherence, which leads to another spooky feature of quantum mechanics: delocalization. As described earlier, a single atom can be in more than one place at the same time, and different parts of the wave function can interfere with each other. A classic example of quantum sensing with delocalized atoms is the atom interferometer [18]. By exploiting the wave nature of particles, we are now able to use the interference of de Broglie waves to perform state-of-the-art measurements of gravity [19], rotation[4], fine structure constant [20, 21] and even dark matter and dark energy [22, 6].

The space-time trajectories of Mach-Zehnder matter-wave interferometers are shown in Fig. 1.3. A single wave packets can be spitted into two, which later spatially separate from each other while free falling under gravity. The relative phase ϕ between the two matter waves is determined by the kinetic energies or the difference in couplings to the environment, see Chapter 2 and 4 for details. The accumulated phase shift can be measured by the population difference between the two wave packets after applying additional laser pulse when the two wave packets overlap.

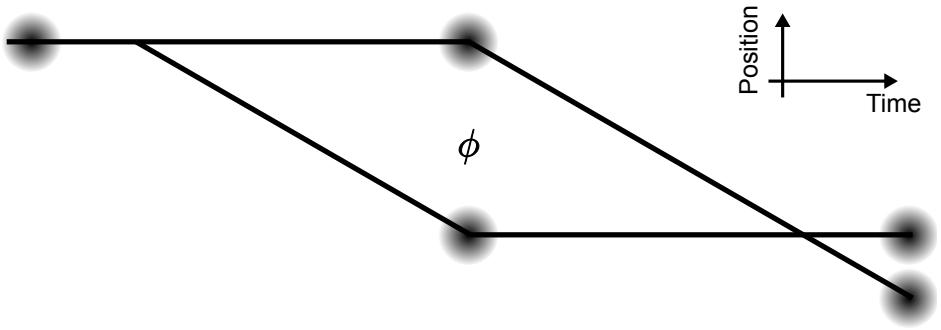

Figure 1.3: A matter-wave interferometer is realized by splitting and recombining the wave packets. Here, the blurry blobs represent the wave packets for different momentum states. The goal is to measure the accumulated phase ϕ between different trajectories which depends on gravity.

In this thesis, I will present the first entanglement enhanced matter-wave interferometer by generating squeezing between matter-wave packets.

1.3 Cavity quantum electrodynamics with cold atoms in an optical cavity

Before getting into the details, I will start by motivating with discussions on what is cavity quantum electrodynamics (QED) and why is it interesting. Cavity QED is a broad concept for the study of the interaction between matter and quantized electromagnetic fields. Such systems generally describe an atom that emits light (or in our case many atoms) coupled to a resonator. This concept can be generalized to include ions trapped in an optical cavity, superconducting qubits couple by electrical resonators [23], rare-earth ion doped in photonic crystal [24], etc.

The squeezing between matter wave packets is realized in a cavity quantum electrodynamics platform with ^{87}Rb trapped inside a high-finesse Fabry-Perot cavity formed by two macroscopic mirrors. Such system havs succeeded in generating the most amounts of directly observed entanglement [25, 26] of any experimental platform, including degenerate gases [27, 28, 29], trapped ions [30, 31, 32] to superconducting qubits [23], etc.

Apart from entanglement generation, with the atoms strongly coupled to the photons inside the cavity, cavity QED systems allow one to exploit all possible tools offered by quantum mechanics: unitary evolution, quantum measurement, and dissipation. Unitary dynamics or many-body interactions between atoms can be mediated by the common cavity mode that couples all the atoms. Measurements of the atomic states can be achieved by measuring the photonic state, since all atoms are coupled to the cavity. Dissipation can be induced by engineering cavity field (bath), such that the atomic information is lost due to photon leaking out of the cavity. All these capabilities also make cavity QED an appealing platform for quantum simulation.

1.4 Outline of thesis work

This thesis is organized as follows: In Chapter 2 I will first introduce the theory for understanding the atom-cavity coupled system and the basics of spin squeezing and atom interferometry. In Chapter 3, I will review the design and construction of our apparatus. In Chapter 4, I will discuss an experiment for generating entanglement between atomic momentum states for realizing an

entanglement-enhanced matter-wave interferometer. In Chapter 5, I will discuss a novel many-body interaction directly between two atomic momentum states and a collective recoil mechanism that arises from this interaction. In Chapter 6, I will discuss an experiment that generalize the interactions between momentum states and realizes Hamiltonian engineering of atomic momentum states. With the tunable all-to-all Heisenberg XYZ model, the long-sought two-axis counter-twisting dynamics are witnessed at the mean-field level for the first time. In Chapter 7, I will conclude by identifying a few promising future directions, as well as challenges and possible solutions.

The following are abstracts for the three experiments that highlight our efforts to better understand and control interactions between matter waves. Going from establishing many-body interactions using the atomic spin state, we can now directly induce interactions between momentum states with the same spin, and even design arbitrary interactions with quadratic Hamiltonians to realize more interesting and useful dynamics.

1.4.1 Entanglement-enhanced matter-wave interferometer

By tagging the momentum state to atomic internal states, we realize cavity-QED entanglement of external degrees of freedom to realize a matter-wave interferometer of 700 ^{87}Rb atoms in which each individual atom falls freely under gravity and simultaneously traverses two paths through space while also entangled with the other atoms [11]$^{[G]}$. We demonstrate both quantum non-demolition measurements and cavity-mediated spin interactions for generating squeezed momentum states with directly observed metrological gain $3.4^{+1.1}_{-0.9}$ dB and $2.5^{+0.6}_{-0.6}$ dB below the standard quantum limit respectively. An entangled state is for the first time successfully injected into a Mach-Zehnder light-pulse interferometer with $1.7^{+0.5}_{-0.5}$ dB of directly observed metrological enhancement. Reducing the fundamental quantum source of imprecision provides a new resource that can be exploited to directly enhance measurement precision, bandwidth, and accuracy or operate at reduced size.

1.4.2 Cavity-mediated momentum-exchange interactions

Without the atomic internal degrees of freedom, we can also induce exchange interactions between momentum states through the interplay between the atomic density grating and the cavity. In this experiment, we realize for the first time momentum-exchange interactions in which atoms exchange their momentum states via collective emission and absorption of photons from a common cavity mode [12][G]. The momentum-exchange interaction leads to an observed all-to-all Ising-like interaction in a matter-wave interferometer, which is useful for entanglement generation. A many-body energy gap also emerges, effectively binding interferometer matter-wave packets together to suppress Doppler dephasing, akin to Mössbauer spectroscopy. The tunable momentum-exchange interaction provides a new capability for quantum interaction-enhanced matter-wave interferometry and for realizing exotic behaviors including simulations of superconductors and dynamical gauge fields.

1.4.3 Hamiltonian engineering of atomic momentum states

In Chapter 6, we show that we can create more complex cavity-mediated interactions, and eventually realize Hamiltonian engineering of XYZ models between momentum states [13][G]. This is achieved by adding a second dressing laser tone and carefully controlling it amplitude and phase relative to the first dressing laser tone. We demonstrate the tunability of the Hamiltonian by explicitly mapping out the evolution of Bloch vectors on the Bloch sphere at the mean-field level and witness the two-axis counter-twisting dynamics for the first time. Our work paves the way towards quantum simulation of more complex systems and fast robust entanglement generation with momentum states for future quantum enhanced metrology.

Chapter 2

Introduction and theory

This thesis is focused on a system with matter waves coupled to a high-finesse cavity. In order to establish a basic theory framework for the experiments, this chapter aims to provides introduction on atom-cavity coupling, spin squeezing, and atom interfrometry. I will first introduce the language for understanding atom-cavity coupling. Secondly, I will discuss quantum sensing with two level systems, the standard quantum limit, and the concept of spin squeezing. Finally, I will introduce matter-wave interferometry, and present the mapping from the momentum states to effective spin states and an intuitive picture for understanding matter-wave interferometers using a Bloch vector representation of the two paths that the matter-wave packets take as they traverse the interferometer. Parameters relevant for the experiment will be presented during the discussion with a table given in the end for summarizing them.

2.1 ^{87}Rb atoms coupled to an optical cavity

As mentioned before, cavity QED systems can allow for unitary dynamics, quantum measurements and dissipations. Here, I will use our experimental system with ^{87}Rb atoms trapped in a two-mirror Fabry-Perot cavity (as shown in Fig. 2.1) as an example, to give a unified picture for understanding the cavity-mediated interactions [33] and non-demolition measurements [34, 35] realized in cavity QED systems. Dissipation is not a core focus of this thesis, but will be discussed in Chapter 5.

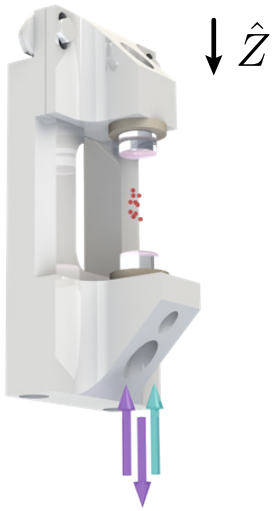

Figure 2.1: Rb atoms in a two-mirror high-finesse cavity vertically oriented along $\hat{Z}$.

A simplified energy diagram for ^{87}Rb is shown in Fig. 2.2A on the right (detailed level diagrams [36] will be given in later chapters when relevant.) The optical excited state is labeled as $|e\rangle \equiv \left|5^2P_{3/2}, F = 3\right\rangle$. The two ground states $|\uparrow\rangle \equiv \left|5^2S_{1/2}, F = 2\right\rangle$ and $|\downarrow\rangle \equiv \left|5^2S_{1/2}, F = 1\right\rangle$ are separated by a hyperfine spiting $\omega_{HF} \approx 2\pi \times 6.834$ GHz. The frequency for the optical transition connecting the ground state $|\uparrow\rangle$ and the excited state $|e\rangle$ is labeled as ω_a with a natural linewidth of $\Gamma = 2\pi \times 6.06$ MHz[36] determined by the decay rate of the excited state. The corresponding wavelength is $\lambda = 780$ nm.

For the high-finesse cavity studied in this thesis (Fig. 2.2A, left), the two mirrors are separated by $L_{cav} = 2.02$ cm, giving a free-spectral range (FSR) $\omega_{FSR} = 2\pi \times 6.788$ GHz. The FSR is chosen to roughly match the hyperfine splitting for driving two-photon transitions (see Chapter. 4 for details.) For the atomic transition wavelength $\lambda = 780$ nm, the transmission coefficients of the top and bottom mirror are roughly $T_1 \approx 2$ ppm and $T_2 \approx 40$ ppm, which leads to a finesse of $\mathcal{F} = 130,000$ after accounting for additional scattering loss (about 2 ppm per mirror.) The cavity linewidth is $\kappa = \omega_{FSR}/\mathcal{F} \approx 2\pi \times 52$ kHz. The cavity mode waist is $w_0 = 72$ μm. For an atom at the anti-node of the cavity mode, the maximal atom-cavity coupling is $g_0 = 0.48$ MHz (for the cycling transition $|F = 2, m_F = 2\rangle \rightarrow |F' = 3, m'_F = 3\rangle$), which leads to a single atom cooperativity

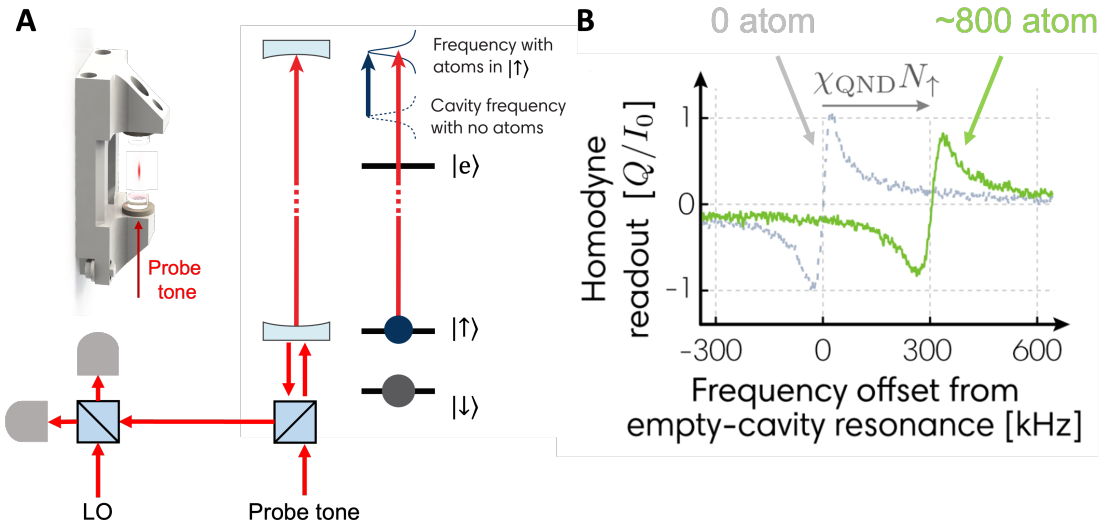

Figure 2.2: Homodyne detection of dressed cavity resonance. (A) Homodyne detection is performed by scanning the frequency of the incident photon in to the cavity and overlap with an local oscillator beam to measure the cavity induced phase shift. (B) Dressed cavity resonance (green) is shifted by an amount proportional to the number of atoms in the spin up $N_\uparrow$ inside the cavity. Here in this plot, there are 800 atoms all prepared in $|\uparrow\rangle$ in the cavity. Bare cavity resonance is shown by gray lines.

of $\mathcal{C} = \frac{g^2}{\kappa\Gamma}$ of order 1, depending on the specific atomic transitions of interest. For the cycling transition $|F = 2, m_F = 2\rangle \rightarrow |F' = 3, m'_F = 3\rangle$ with the highest Clebsch–Gordan coefficient, the cooperativity is $C_0 = 0.73$, assuming all atoms are at the anti-nodes of the cavity mode. A cavity mode frequency ω_c is detuned from $|\uparrow\rangle \rightarrow |e\rangle$ transition ω_a by $\Delta_a = \omega_a - \omega_c$.

For the experiments presented in this thesis, the atom-cavity detuning is typically set to be $\Delta_a < 2\pi \times 500$ MHz, much smaller as compared to the hyperfine spplitting ω_{HF}. Up to small energy shift on $|\downarrow\rangle$, we can ignore the coupling between $|\downarrow\rangle$ and $|e\rangle$ for simplicity. With N atoms in the cavity, the system is described by the Tavis-Cummings Hamiltonian

$$\hat{H}_{TC} = \hbar\omega_c \hat{a}^\dagger \hat{a} + \sum_{i=1}^{N} \omega_e \left|e\right\rangle_i \left\langle e\right|_i + \hbar g_0 \sum_{i=1}^{N} \left(\hat{a} \left|e\right\rangle_i \left\langle\uparrow\right|_i + \hat{a}^\dagger \left|\uparrow\right\rangle_i \left\langle e\right|_i\right), \tag{2.1}$$

where the three terms correspond to quantized cavity field, atomic state, and the coupling between the two. Here, $\hat{a}^\dagger$ and $\hat{a}$ are the creation and annihilation operators for the cavity mode, i is the index for the i^{th} atom.

For simplicity, all atoms are assumed to have the same coupling coefficient g_0 with the cavity.

Other than trapping atoms in a commensurate lattice, this can also be achieved by performing side selection on the atoms [37][G]. The spatial dependence of the atom-cavity coupling can modify the effective atom number, atom-cavity coupling and induce opto-mechanical effect. Here, the opto-mechanical effects (cavity field changing atomic motion) are unwanted in many experiment, but in contrast, it is crucial for the momentum-exchange interaction and will be discussed in Chapter 5.

We rewrite the Hamiltonian in the rotating frame of the cavity field at ω_c, with the Hamiltonian by $\hat{H}_r = \hbar\omega_c \left(\hat{a}^\dagger\hat{a} + \sum_i^N |e\rangle_i \langle e|_i\right)$. In this rotating frame, under the transformation given by the unitary $\hat{U} = \exp\left(i\hat{H}_r t\right)$, the Hamiltonian $\hat{H}' = \hat{U}^\dagger \hat{H}_{TC} \hat{U} + i\hbar\frac{\partial \hat{U}^\dagger}{\partial t}\hat{U}$ takes the form:

$$\hat{H}' = \hbar\Delta_a \sum_{i=1}^{N} |e\rangle_i \langle e|_i + \hbar g \sum_{i=1}^{N} \left(\hat{a} |e\rangle_i \langle\uparrow|_i + \hat{a}^\dagger |\uparrow\rangle_i \langle e|_i\right). \tag{2.2}$$

We can then drive the equation of motion for the operator $|e\rangle_i \langle\uparrow|_i$

$$\frac{d\left(|e\rangle_i \langle\uparrow|_i\right)}{dt} = i\hbar\left[|e\rangle_i \langle\uparrow|_i, H'\right] = i\hbar\left[-\Delta_a |e\rangle_i \langle\uparrow|_i + g\left(\hat{a} |e\rangle_i \langle e|_i - \hat{a}^\dagger |\uparrow\rangle_i \langle\uparrow|_i\right)\right]. \tag{2.3}$$

In the large detuned limit with $\Delta_a \gg \Gamma, \kappa, g_0$, the excited states are not populated and thus could be adiabatically eliminated with $\langle |e\rangle_i \langle e|_i \rangle \approx 0$. Solving for the steady state response with $\frac{d\left(|e\rangle_i \langle\uparrow|_i\right)}{dt} = 0$, we have $|e\rangle_i \langle\uparrow|_i = \frac{g\hat{a}^\dagger |\uparrow\rangle_i \langle\uparrow|_i}{\Delta_a}$. Substituting this back to the original Hamiltonian Eq. 2.2 gives an effective Hamiltonian

$$\hat{H}_{eff} = \hbar\chi_{QND} \sum_{i}^{N} |\uparrow\rangle_i \langle\uparrow|_i \hat{a}^\dagger\hat{a} = \hbar\chi_{QND}\hat{N}_\uparrow\hat{a}^\dagger\hat{a}, \tag{2.4}$$

with $\chi_{QND} = g^2/\Delta_a$. Here, a constant single particle term proportional to $\sum_i^N |e\rangle_i \langle e|_i$ has been neglected. The collective population operator is defined as $\hat{N}_\uparrow = \sum_i^N |\uparrow\rangle_i \langle\uparrow|_i$, which measures the total atom number in $|\uparrow\rangle$.

This effective Hamiltonian enables the quantum nondemolition (QND) measurements by introducing an interaction between the sub-system that needs to be measured (atomic state) and the measurement apparatus (photonic state of the optical cavity.) With finite population $N_\uparrow = \langle\hat{N}_\uparrow\rangle$ in the cavity, the effective Hamiltonian can be intuitively understood as the cavity resonant frequency being shift by $\chi N_\uparrow$, which is exactly proportional to the population in $|\uparrow\rangle$ as counted by the operator

$N_\uparrow$, with χ_{QND} being the cavity frequency shift induced by a single atom. Therefore, by measuring the cavity frequency shift, we can then measure the collective atomic population. For typical numbers in this thesis, the single atom frequency shift is $\chi_{QND} \approx 2\pi \times 175$ Hz.

Having this picture in mind, we can now design an experiment to perform atom number measurements by probing the cavity resonances. As shown in Fig. 2.2,A the cavity resonance is probed using homodyne detection. By scanning the frequency of the photon incident at the cavity, collecting the retro-reflected photon and measuring the relative phase shift against a local oscillator (LO), an example experimental homodyne signal is shown in Fig. 2.2 with the Q-quadrature response [38][G]. With no atoms in the cavity, the cavity resonance is centered at zero (gray line). The cavity frequency is then shifted by about 300 kHz with 800 atoms (green line.) For this experimental data, atoms are prepared in $|F = 2, m_F = 0\rangle$ state, the cavity is detuned by 175 MHz from the atomic transition and is probed by light with σ^+ polarization.

The cavity-mediate interaction between atoms can be understood with the same Hamiltonian. We again consider the same experiment, but now apply a pump laser tone with a fixed detuning δ_{pump} ($\Delta_a \gg \delta_{pump} > \kappa/2$) from the dressed cavity resonance instead of scanning the frequency across the resonance. With the pump laser amplitude α_{pump} (in unit of $\sqrt{\text{photons/second}}$), the driven cavity Hamiltonian now become

$$\hat{H}_{pump} = \hbar\chi_{QND}\hat{N}_\uparrow\hat{a}^\dagger\hat{a} + \hbar\left(\alpha_{pump}e^{i\delta_{pump}t}\hat{a}^\dagger + \alpha^*_{pump}e^{-i\delta_{pump}t}\hat{a}\right), \tag{2.5}$$

with the jump operator $\hat{L} = \sqrt{\kappa}\hat{a}$ describing the photon loss of the cavity.

In an empty cavity with no atom inside ($\langle\hat{N}_\uparrow\rangle = 0$), we can solve for the steady state intra-cavity amplitude $\alpha_{cav} = \frac{\alpha_{pump}}{1+i\frac{\delta_{pump}}{\kappa/2}}$ by going into the rotating frame of the pump photon frequency. With N atoms inside the cavity prepared in equal superpositions of $|\uparrow\rangle$ and $|\downarrow\rangle$, the steady-state intra-cavity amplitude then becomes

$$\alpha_{cav} = \frac{\alpha_{pump}}{1 + i\frac{\delta_{pump}+\chi_{QND}\left(N/2+\hat{J}_z\right)}{\kappa/2}}, \tag{2.6}$$

where $\hat{J}_z = \left(\hat{N}_\uparrow - \hat{N}_\downarrow\right)/2$ is the population difference operator. With equal superpositons between

the two spin states, we can then perform an expansion of the amplitude around $\langle \hat{J}_z \rangle = 0$ and get $\langle \hat{a}^\dagger \hat{a} \rangle \approx \frac{|\alpha_{pump}|^2}{1+\frac{\left(\delta_{pump}+\chi_{QND}N/2\right)^2}{\kappa^2/4}} + \chi_{OAT}\hat{J}_z$.

In the presence of atoms inside the cavity, the laser-cavity detuning thus depends on the atom number, which then changes the intra-cavity photon number. In other words, the photon number established inside the cavity now depends on the atomic population difference $\hat{a}^\dagger \hat{a} \propto \hat{J}_z$ (up to a constant term.) After substituting back into Eq. 2.4 and ignoring the constant term, the effective Hamiltonian becomes

$$\hat{H}_{OAT} = \hbar \chi_{OAT} \hat{J}_z^2, \tag{2.7}$$

which describes a many-body interaction such that the relative phase between the two spin state accumulates at a rate proportional to the population difference $\langle \hat{J}_z \rangle$ at the mean-field level. This is exactly the quadratic Hamiltonian gives rise to the one-axis twisting dynamics [16] for squeezing generation. See Chapter 4 for details.

2.2 Quantum metrology and spin squeezing

Having discussed the basics of cavity-QED, I will now turn to introduce one of its applications (specifically, entanglement generation) in quantum metrology, starting with quantum sensing and the definition of standard quantum limit.

The basic principle for quantum sensing with two-level systems is to encode an information of interest (time, magnetic field, gravity, etc.) into the relative phase between the two levels and measure this phase. As an example, the two hyperfine ground state of rubidium atoms can be utilized for sensing time because finite energy difference ($\hbar\omega_{HF}$) between them. For pseudo-spin systems formed by two levels, it is helpful to understand the representation of quantum states on Bloch spheres. As an example, the north and south poles of the Bloch sphere can be defined by the two hyperfine ground states $|\uparrow\rangle$ and $|\downarrow\rangle$. Quantum states (for a single atom or many atoms) are represented by a Bloch vector $\vec{J} = \langle \hat{J}_x \rangle \hat{x} + \langle \hat{J}_x \rangle \hat{y} + \langle \hat{J}_x \rangle \hat{z}$ in a fictitious coordinate space. Here, the collective spin projection operators are defined as $\hat{J}_z = \left(\hat{N}_\uparrow - \hat{N}_\downarrow\right)/2$, $\hat{J}_x =$

$\sum_{i=1}^{N}\left(|\uparrow\rangle_i\langle\downarrow|_i+|\downarrow\rangle_i\langle\uparrow|_i\right)/2$ and $\hat{J}_y=\sum_{i=1}^{N}\left(|\uparrow\rangle_i\langle\downarrow|_i-|\downarrow\rangle_i\langle\uparrow|_i\right)/(2i)$. In this picture, a specific quantum state $|\psi\rangle=\cos(\theta/2)|\uparrow\rangle+\sin(\theta/2)\,e^{i\phi}|\downarrow\rangle$ is represented by a Bloch vector with a polar angle θ (opening angle from the north pole) and an azimuthal angle ϕ.

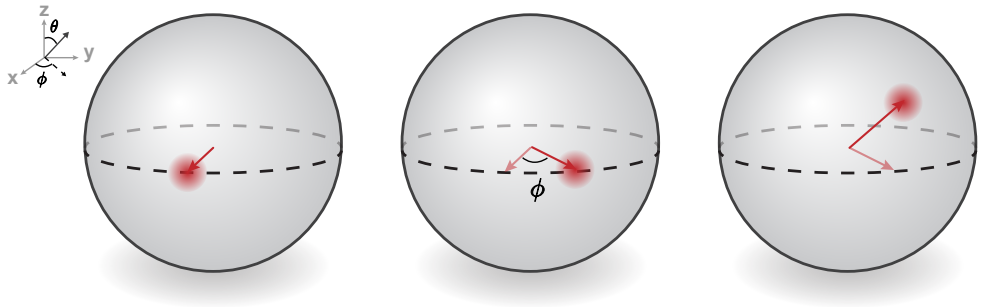

Figure 2.3: Ramsey sequence on Bloch spheres. Starting with an initial state on the equator, the energy difference between the two levels changes the relative phase. The accumulated phase shift is turned into population difference with a $\pi/2$-pulse for readout.

A classic method for phase measurement is the Ramsey sequence. Let's first start with all atoms in the $|\downarrow\rangle$. Applying a $\pi/2$-pulse (with microwave or two-photon transition), one can prepare an initial state into $|\psi\rangle=(|\uparrow\rangle+|\downarrow\rangle)/\sqrt{2}$, represented by a Bloch vector pointing along x-axis on the equator. Due to the energy difference, the relative phase between the two state change by $\phi=\omega_{HF}T$ after certain evolution time T. By applying another $\pi/2$-pulse along y-axis, the phase information is now turned into population difference. By measuring the population difference, we can then extra relative phase and thus estimated the evolution time T.

In Fig. 2.3, the blurry blob around the Bloch vector represent the quantum noise distribution due to the random collapse of individual atoms when one makes a measurement of the populations to determine the spin projection J_z. For example, with a Bloch vector prepared on the equator, the spin projection J_z measurements give an average of zero. But, the individual measurements vary shot-to-shot by $\sqrt{N}/2$. In the large number limit $N\gg 1$, the resulting angular uncertainty for estimating the polar angle θ is then $\Delta\theta=\Delta J_z/J=1/\sqrt{N}$, which defines the standard quantum limit.

With QND measurements or OAT dynamics, we can create spin squeezed states with reduced

noise along one of the quadratures, represented by the elliptical distribution as shown in Fig. 2.4. By preparing the initial state of Ramsey sequence to be a squeezed state along the phase quadrature, we can explicitly see how squeezing reduces the noise in the readout process, and thus reduce the uncertainty in estimating the accumulated phase.

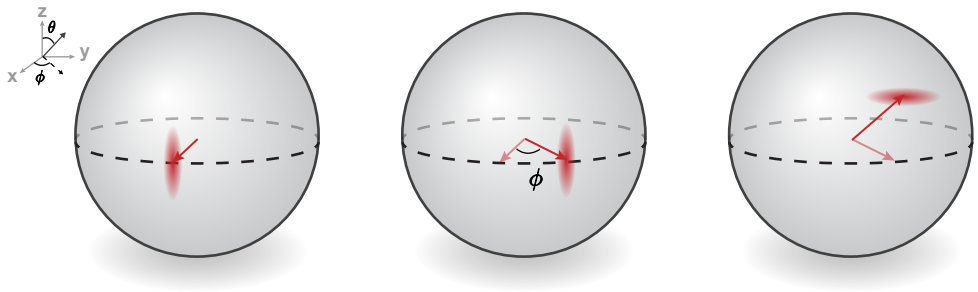

Figure 2.4: Ramsey sequence with squeezed state along phase quadrature. Starting with the azimuthal phase-squeezed state, the noise for the final population measure measurement is reduced.

A detailed comparison between QND and OAT can be found in [39][G]. As a result, for any cavity-QED systems with properly define quantum efficiency $\eta > \frac{3}{16}$, QND is fundamentally better than OAT for squeezing generation. However, we note that which approach is best to use truly depends strongly on additional technical constraints and imperfections in an experiment.

2.3 Matter-wave interferometer

Apart from two-level systems based on atomic internal states, one can also prepare quantum superposition with motional states or external degrees of freedom and realize a matter-wave interferometer. An atom interferometer is a technique that really exploit the wave nature of particles. Just like optical interferometer, atoms can also be spitted, recombined and interfered. Because atoms are massive, they are sensitive to inertial quantities unlike photons. They can perform some of the most precise measurements thanks to the ultra-short de Broglie wavelengths.

A simplified diagram for understanding the matter-wave interferometer is shown in Fig.2.5. Atoms are all in a single momentum state to begin with. A laser pulse prepares the atoms in a quantum superposition of two different momentum states, corresponding to having kicked by

photons or not. Due to the finite spread in momentum distributions, the two wave packets start to separate from each other. At the same time, a relative phase starts to accumulate. An extra pulse of laser is applied to flip the momenta of the two wave packets, such that they start to recombine. By the time they re-overlap, a final laser pulse is applied for reading out the interference.

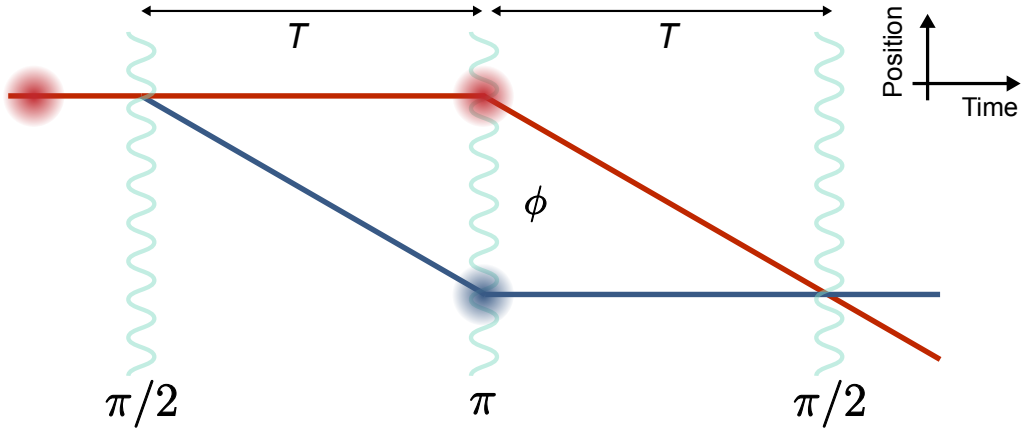

Figure 2.5: Mach-Zehnder matter-wave interferometer sequence. Horizontal axis is time, vertical axis is spatial position. The slopes represent different momentum states. Different colors label the two paths of wave packets.

There are different (however equivalent) interpretations of the accumulated phases. In one picture, one can consider the first laser pulse imprints an optical phase to the atomic density grating. When the two wave packets recombine at the different location, the interference then serves as a phase memory for comparing to the local laser phase when the readout pulse is applied [40][G]. In other words, the atomic wave function works as a ruler for measuring the optical phase of the laser field when traveling through space.

An alternative way for understanding the phase is by tacking the kinetic energy difference between the two wave packets. Let's consider the initial momentum state of the wave packet is $|p_0 - \hbar k\rangle$. The two-photon transition prepare equal superposition between $p_0 \pm \hbar k$. However, both wave packet are free-falling under gravity, which results in time-varying momentum $p_0 \pm \hbar k + mgt$. Here, g is the gravitation acceleration, m is the mass of the atom and t is the time. The difference

in kinetic energy at time t is thus

$$\Delta E\left(t\right)=\frac{\left(p_0+\hbar k+mgt\right)^2}{2m}-\frac{\left(p_0-\hbar k+mgt\right)^2}{2m}=2\hbar k\left(v_0+gt\right), \tag{2.8}$$

where $v_0 = p_0/m$ is the average initial velocity of the two wave packet. This differential kinetic energy can also be understood as the Doppler shift due to the falling atoms. In order to resonantly drive the two-photon transition connecting the two momentum states $|p_0 \pm \hbar k + mgt\rangle$, the frequency separation between the two photons needs to be chirped at a rate $\alpha = 2kg \approx= 2\pi \times 25.1$ kHz/ms. Assuming the two lasers tone are separated by ω_0 at $t = 0$, this separation become $\omega_0 + \alpha t$ at time t.

For the Mach-Zehnder interferometer sequence shown in Fig. 2.5, the duration T of phase accumulated is the same before and after applying the π-pulse for refocusing the wave packets. At any instantaneous time T' through the sequence, the relative phase between the two laser tones for driving the two-photon transition is

$$\phi\left(T'\right)=\int_0^{T'}\left(\omega_0+\alpha t\right)dt \tag{2.9}$$

The total phase shift between the two wave packets is

$$\phi=\phi\left(0\right)-2\phi\left(T\right)+\phi\left(2T\right)=2kgT^2, \tag{2.10}$$

which scales quadratically with the accumulation period T.

In the experiment, we scan the phase of the final $\pi/2$-pulse when the two wave packets overlap with each other and measure the population in the two momentum states. The population difference varis depending on the readout phase and give rise to the fringe of the interferometer.

2.3.1 Interferometric sequence on a Bloch sphere

The Bloch sphere representation of quantum sensing is a powerful way to understand the quantum sensors, and for understanding how squeezed states can improve the sensitivity of such interferometers. There exists a one-to-one mapping between the rotations on the Bloch sphere and the laser pulses in matter-wave interferometer sequence. The matter-wave Mach Zehnder

interferometer can be understood as a $\pi/2 - \pi - \pi/2$ spin echo sequence [41] with pseudo-spin states.

The initial $\pi/2$-pulse that prepares equal superposition of two momentum states corresponds to the $\pi/2$ rotation that prepares a Bloch vector on the equator. The relative phase accumulated between the wave packets is exactly the change in azimuthal phase on the Bloch sphere. The π-pulse that recombines the wave packets together can be understood as a echo π-pulse on the Bloch sphere that cancel the inhomogeneity that arises from the finite spread in momentum.

2.3.2 Effective spin 1/2 system with momentum states

In this thesis, different Bloch spheres are defined with different choices of two levels. The specific definitions will be explained in each chapter. Here in Fig. 2.6, we summarized three different interferometers with different two levels.

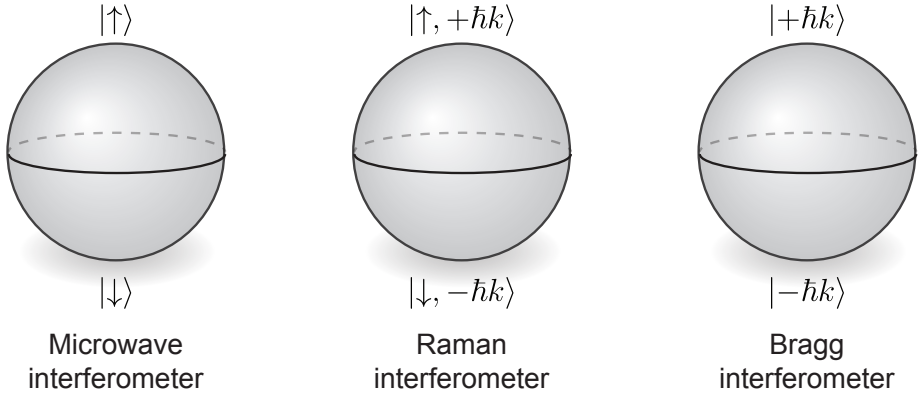

Figure 2.6: **Bloch spheres defined with different two levels.** A microwave interferometer can be realized with atomic internal two levels, such as the hyperfine states $|\uparrow\rangle$ and $|\downarrow\rangle$. A Raman matter-wave interferometer is based on spin-momentum states $|\uparrow, +\hbar k\rangle$ and $|\downarrow, -\hbar k\rangle$. A Bragg matter interferometer involves only the atomic momentum states $|+\hbar k\rangle$ and $|-\hbar k\rangle$.

In a Bragg interferomter where atoms are in the same internal states, the interference of the wave packets (when overlapped) also leads to a spatially varying atomic density distribution. Here, I'll discuss the connection between the pointing of the Bloch vector and the atomic density grating.

For the works in Chapter 5 and 6 on momentum-exchange interactions and tunable XYZ

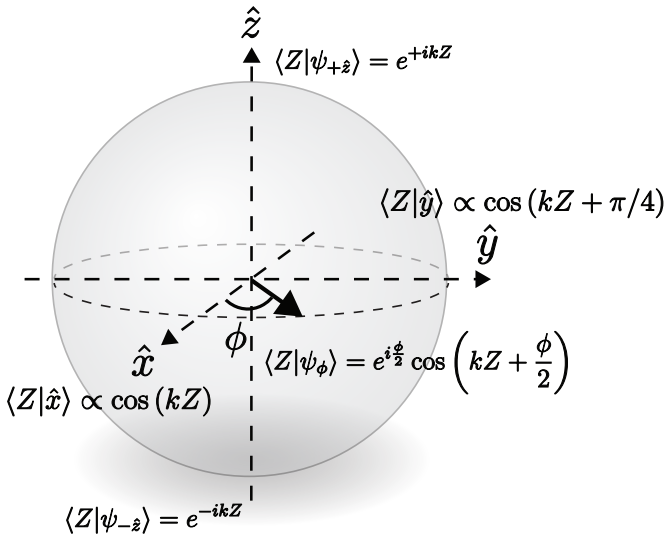

Figure 2.7: **Bloch sphere formed by momentum states.** The corresponding wave functions are given for different Bloch vectors on the equator.

models, the atoms are prepared in the same internal states. The effective spin-1/2 system is then defined by two momentum states $|\pm\hbar k\rangle$ (ignoring the average momentum), which correspond to the north and south poles of the Bloch sphere. The polar angle is still determined by the population difference between the two momentum states. The azimuthal angle again corresponds to the relative phase between the two momentum states, which also defines the spatial phase of the atomic wave function in the context of a Bragg interferomter. As shown in Fig. 2.7, the north/south poles are $|\uparrow\rangle \equiv |\psi_+\rangle \equiv |+\hbar k\rangle$ and $|\downarrow\rangle \equiv |\psi_-\rangle \equiv |-\hbar k\rangle$. The corresponding atomic wave functions are $\langle Z|\psi_\pm\rangle = e^{\pm ikZ}$. Here, $|Z\rangle$ is the position operator, $\langle Z|\psi_\pm\rangle$ is the wave function in position space, and Z labels the position along the cavity axis.

For a Bloch vector on the equator, the quantum state is $|\psi_\phi\rangle = \left(e^{i\phi/2}|\uparrow\rangle + e^{-i\phi/2}|\downarrow\rangle\right)/\sqrt{2}$ with the corresponding wave function $\langle Z|\psi_\phi\rangle = e^{i\phi/2}\cos(kZ + \phi/2)$. Therefore, the azimuthal phase of the Bloch vector also determines the spatial phase of the atomic density grating. This is an important intuition for understanding the momentum-exchange interaction experiment.

2.3.3 Momentum states coupled to cavity

The spatial dependence of the atom-cavity coupling was ignored previously, but we will now revisit this feature after introducing atomic momentum states and the idea that superpositions of momentum states give rise to atomic density gratings. Depending on the positions, the atom-coupling coupling coefficient g_i of an specific atom i is $g_i = g_0 \cos(kx_i)$, where g is the maximal coupling at the anti-node, k is the wave vector of the cavity field and x_i is the position of the i^{th} atom along the cavity axis. Allowing for the spatially varying atom-cavity coupling, the effective Hamiltonian Eq. 2.4 thus becomes

$$\hat{H}_{eff} = \hbar \sum_i^N \frac{g_0^2 \cos(kx_i)}{\Delta_a} |\uparrow\rangle_i \langle\uparrow|_i \hat{a}^\dagger \hat{a} = \hbar \sum_i^N \frac{g_0^2 \left(e^{2ikx_i} + e^{-2ikx_i} + 1\right)}{2\Delta_a} |\uparrow\rangle_i \langle\uparrow|_i \hat{a}^\dagger \hat{a}. \tag{2.11}$$

The Hamiltonian now depends on the spatial distribution of the atoms. In the far detuned limit, all atoms are in the ground state, and therefore $\hat{H}_{eff} = \hbar \sum_i^N \frac{g_0^2\left(e^{2ikx_i} + e^{-2ikx_i} + 1\right)}{2\Delta_a} \hat{a}^\dagger \hat{a}$.

In the pseudo-spin system defined by the two momentum states $|p_0 \pm \hbar k\rangle$, the real space wave functions of the two spin states are $\langle x|p_0 \pm \hbar k\rangle = e^{i(p_0/\hbar \pm k)x_i}$ for the i^{th} atom. The $e^{\pm 2ik\hat{x}_i}$ are exactly the momentum displacement operators that change the atomic momentum by $\pm 2\hbar k$. Specifically, $e^{\pm 2ik\hat{x}_i} |p_0 \mp \hbar k\rangle = |p_0 \pm \hbar k\rangle$. Equivalently, they manifest as the raising and lower operators $e^{\pm 2ik\hat{x}_i} \equiv \hat{j}_{i,\pm}$ for the pseudo-spin system. Collective operators can be defined $\hat{J}_\pm = \sum_i^N \hat{j}_{i,\pm} = \sum_i^N e^{\pm 2ikx_i}$, $\hat{J}_x = \frac{\hat{J}_+ + \hat{J}_-}{2}$, $\hat{J}_y = \frac{\hat{J}_+ + \hat{J}_-}{2i}$ and $\hat{J}_z = \sum_i^N \exp^{+ikx_i} - \exp^{-ikx_i}$. By applying a Bragg $\pi/2$-pulse, one can prepare all atoms in superpositions of the two momentum states with the same relative phase, such that the length of the Bloch vector $|\vec{J}| = \left|\left(\langle \hat{J}_x\rangle, \langle \hat{J}_y\rangle, \langle \hat{J}_z\rangle\right)\right| = N/2$.

Substituting the collective operators back to the effective Hamiltonian, we have

$$\hat{H}_{eff} = \hbar \frac{g_0^2 \left(\hat{J}_+ + \hat{J}_- + 1\right)}{2\Delta_a} \hat{a}^\dagger \hat{a}. \tag{2.12}$$

Here, the cross terms between collective raising and lowering operators give rise to different cavity-mediated interaction between momentum states. Details will be discussed later. Specifically, in Chapter 5, we will focus on the momentum-exchange interaction (described by $\hat{J}_+ \hat{J}_-$) where pairs of atoms exchange their momenta by exchanging photons. In Chapter 6, we will incorporate the

pair creation $\hat{J}_+\hat{J}_+$ and pair annihilation processes $\hat{J}_-\hat{J}_-$ to realize tunable XYZ models.

Chapter 3

Apparatus

This chapter aims to introduce the apparatus for realizing matter-wave inerferometry in a high-finesse cavity. I took part in building the whole setup with two other graduate students Baochen Wu and Graham Greve. Additional details of the setup can be found in their theses [42, 43][G]. We started building the apparatus in 2018, and the major parts were completed in 2021. The whole setup was moved from JILA X1B21 to X1B30 in early 2024.

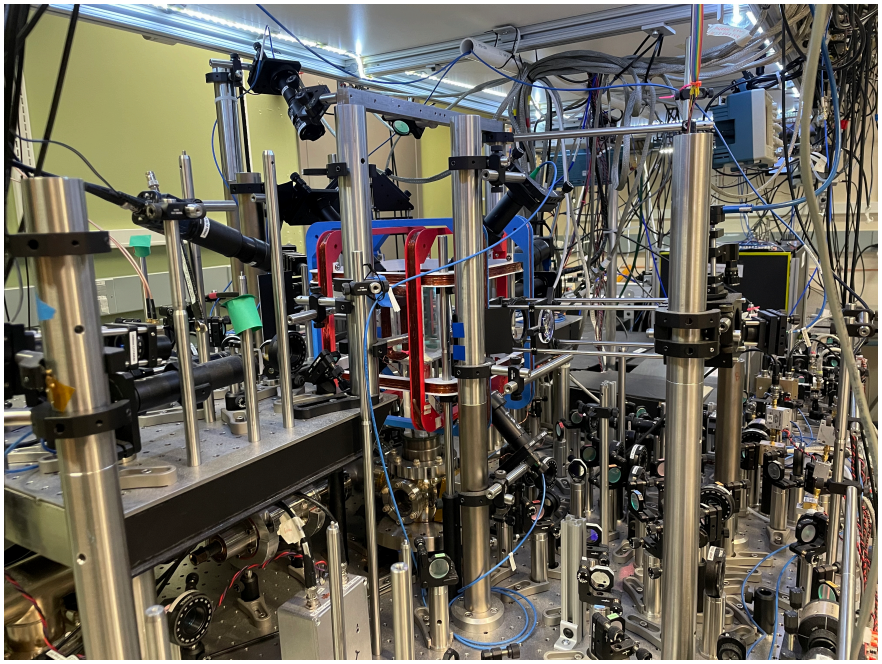

Figure 3.1: A picture of the main system after the move.

The whole experimental apparatus can be roughly divided into mainly three sub-systems to accomplish different requirements for studying science. The first one is the ultra-high-vacuum

system. We need to keep the atoms in a low-pressure environment for reducing the collisions or chemical reactions between the atoms of interest (rubidium in our experiment) and the background gases of molecules, such that the atoms can have long enough lifetime to be trapped and manipulated. The second key subsystem are the various lasers of different wavelengths and spectral properties that we use to trap/cool the atoms, manipulate the atomic internal/external states and to perform measurements on the cavity and the atoms. The third key sub-system is the electronic system for controlling frequencies and powers of all the lasers, and for direct manipulation of atomic state with microwaves. In this chapter, we will begin by high lighting the typical experimental sequence and then provide detailed descriptions of the three key sub-systems.

3.1 Experimental sequence

I will start by giving an overview of the experimental sequence for preparing the atomic states before the matter-wave interferometer, which will highlight different requirements for and capabilities of the apparatus.

For every run of the experiment, we start by cooling and trapping atoms in a two-dimensional magneto-optical trap (MOT) [44] in one of the glass cells (source cell.) At the same time, the atoms are also continuously pushed by a laser beam (on resonance with ^{87}Rb $|F = 2\rangle \rightarrow |F' = 3\rangle$ transition) from the source cell into the main science glass cell. The atoms are then recaptured, cooled and trapped in a three-dimensional MOT which is positioned at the center of the high-finesse cavity. The source glass cell and the science glass cell are connected using a long glass tube with a tiny pinhole at the center. With this configuration, we are able to reduce the rubidium vapor pressure in the science glass cell to prevent coating the high-finesse mirror with rubidium atoms.

Given the small mode waist ($w_0 = 71$ μm) of the cavity, the majority of the atoms in the 3D-MOT are not well coupled to the cavity. We apply polarization gradient cooling (PGC) by jumping the frequencies of two cooling laser by few hundreds of MHz and to load around 10^5 atoms into a 1D red-detuned lattice. The lattice is formed by exciting a cavity longitudinal mode with an 813 nm laser. After lowering the red-detuned lattice depth from 1 mK down to 100 μK,

we apply gray molasses cooling to further lower the atomic temperature down to 5 μK. An extra stage of two-dimensional degenerate Raman sideband cooling is applied to reduce the atomic radial temperature down to 1 μK[1] . We then adiabatically ramp off the red-detuned lattice to transfer the atoms into a blue-detuned 1D dipole trap (trapped depth 50μK) formed by a 760 nm laser. This dipole trap is always on during the sequence for radially confining the atoms while allowing them to free-fall.

After free-falling for 20 ms, the average atomic momentum is given by $p_0 = mv_0$ with an averaged velocity v_0 =20 cm/s. We then optically pump the atoms into $|F = 2, m_F = 0\rangle$ state and perform velocity selection by driving velocity-dependent two-photon Raman transitions connecting $|F = 2, m_F = 0, p_0 + \hbar k\rangle \rightarrow |F = 1, m_F = 0, p_0 - \hbar k\rangle$. Here, $\hbar$ is the reduced Planck constant and k is the wave number of the Raman laser used to drive this transition. By adjusting the duration and Rabi frequency of the pulse, a small group of atoms (typically around 1000 atoms) with narrow momentum distribution (RMS momentum $\sigma_p < 0.05\hbar k$) are transferred to $|F = 1\rangle$. The un-selected atoms are blown away out of the cavity mode with a laser beam (resonant with $|F = 2\rangle \rightarrow |F' = 3\rangle$ transition) applied from the side of the cavity.

At this point, all atoms are prepared in the same atomic internal and external state, while homogeneously coupled to the cavity. The specific sequences for the Raman or Bragg interferometer may vary between different experiments, and will be discussed in Chapter 4, 5 and 6.

3.2 Vacuum glass cell

As explained before, atoms needs to be prepared in ultra-high vacuum for longer lifetime. The complete vacuum setup includes an atomic source glass cell (where we form a two-dimensional magneto-optical trap), a science glass cell which houses the high-finesse cavity (science cavity), a Titanium sublimation pump, an ion pump and some connection parts. Here I'll only focus on the science glass cell.

[1] There is no additional cooling for axial temperature. We rely on velocity selection to reduce the momentum spread along axial direction.

Compared to conventional metal chamber, glass cells have large optical access and low electrical conductance (for reducing Eddy current when changing magnetic fields.) It's however challenging to have anti-reflection (AR) coated on both sides of the cell and to have good optical quality at the surface with using traditional glass blowing technique. For these reasons, we decided to give the optical contact technique a shot.

We started with some two-side AR coated quartz plates purchased from Specialty Glass Products. For the side walls, we have "Fused Quartz Rectangle; 5" $\pm$ 0.01" $\times$ 2.165" $\pm$ 0.01" $\times$ 0.120" $\pm$ 0.01" thickness; top and bottom surfaces polished finish and AR coated centered at 780nm for $<$ 0.2% reflectance at 0 degree AOI and $<$ 0.6% reflectance at 45 degree AOI; 5" long sides polished finish; 2" long sides ground/machined finish; 3mm max rail/shadow marks due to coating". The detailed spec is the same for the top piece but with different dimensions (2.29" $\pm$ 0.01" square $\times$0.120" $\pm$ 0.01" thick). We then asked the machine shop to make a box out of it. The optical contact trick indeed worked to bond two sidewalls to each other, but failed to complete the whole box. Hans then tried to use silicate bonding to "glue" all edges together. The picture and the drawing are shown in Fig. 3.2.

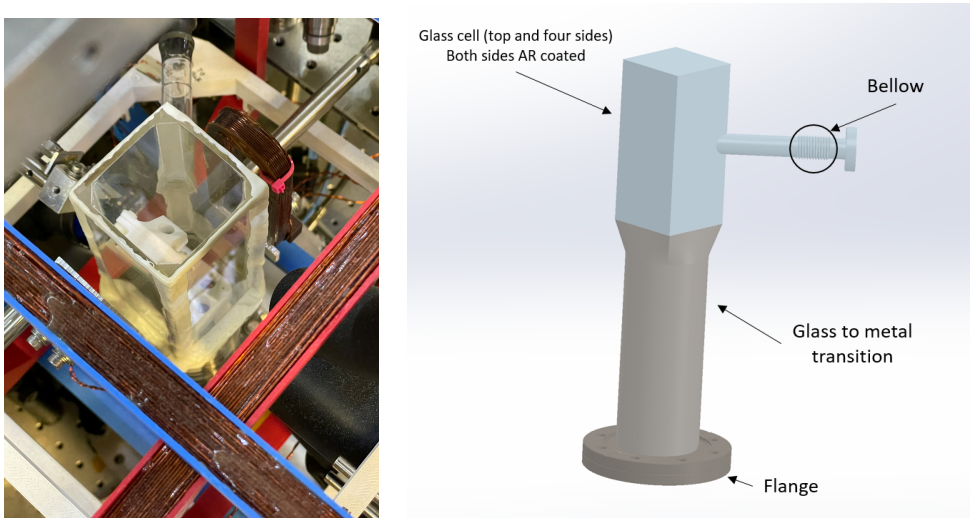

Figure 3.2: Picture and drawing for the glass cell

It was working at the beginning but then started to leak. Thin layers of epoxy (Hysol 1C-LV,

not recommended due to the low glass-to-metal transition temperature) are applied around all edges to seal the leaks. We successfully pumped down the system and baked it up to 100 Celsius degree (which is unfortunately around the glass-to-metal transition temperature of this specific epoxy). When cooling down from the bake, leaks started to develop. We had to use the same epoxy (to avoid reaction or any incompatibility with other epoxy) to seal the leaks again (Nov. 2018.) After sealing the leaks, the pressure became acceptable (1.0-2.0$\times 10^{-8}$ Torr) to perform experiments that last typically less than one second. We then moved on with other construction and eventually the experiments.

But four years later (Jun. 2022), the pressure rose to 8.5$\times 10^{-8}$ Torr and the MOT size reduced by a lot. Luckily, we were able to fix it again by repeating the same leak checking and sealing process. The predominant leak point is found to be around the connection between the slim glass tube and the corner of the glass cell. The pressure went back to normal and even survived the moving of the apparatus from the X1B21 lab to the X1B30 lab across the hall.

Though expensive, there are new companies that can make customized optical contact glass cells. But since we have verified it ourselves that epoxy-glued [2] glass cell can still work, new parts are already purchased for making a new cell to prepare for any future failure.

[2] Make sure you use Torr Seal!

3.3 Science cavity

As shown in Fig. 3.3, the science cavity is form by two mirrors with 5 cm radius of curvature separated by L =2.02 cm. The free spectral range of the cavity is measured to be 6.787893(1) GHz. The linewidth of the cavity is measured to be 52(2) kHz, which corresponds to a cavity finesse of $\mathcal{F} \approx 130000$ at 780 nm.

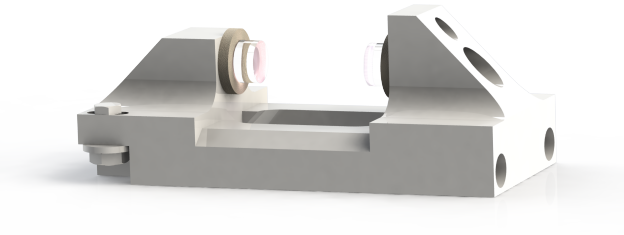

Figure 3.3: A rendered image of the science cavity..

The mode waist of the cavity is calculated to be $w_0 = 71.8$ μm, with the associated Rayleigh range of the cavity field $z_R = 2.07$ cm for $\lambda = 780$ nm. The mode column of the cavity is 8.934×10^{-11} m^3, which gives the peak atom-cavity coupling $g_0 = 0.485$ MHz. For an atoms at the anti-node of the cavity, the maximal atom-cavity Rabi coupling is $2g_0 = 0.970$ MHz.

3.4 Laser system

In the experiments, we use different lasers to cool/trap atoms, to perform matter-wave interferometric control and to probe the atoms and cavity. To address these needs, we require in total nine lasers including two distributed Bragg reflector lasers (DBR) at 780 nm, three grating external cavity diode lasers (ECDL) lasers at 813 and 780 nm, one interference filter ECDL at 760 nm, and three DBR lasers with linewidth narrowed by optical feedback. This is a fairly complex system. For comparison, the number of lasers is comparable to what are considered to be laser-intense experiments on molecules.

3.4.1 Overview of all lasers and the locking chain

Starting with a grating ECDL laser locked to atomic transition, we stabilized two DBR lasers to REF laser with offset phase lock for different laser cooling techniques. An interference filter ECDL at 760 nm is locked to a reference cavity with the Pound-Drever-Hall (PDH) technique [45]. The science cavity is locked to the 760 nm laser such that an intra-cavity dipole trap can be formed for confining the atoms radially while allowing them to under-go free fall along the cavity axis. An 813 nm Littrow-style grating ECDL is PDH-locked to the science cavity for creating a one-dimensional red detuned optical lattice for trapping the atom. A narrowed DBR laser named cavity probe is PDH locked to the science cavity to serve as a tracer beam. Another two narrowed DBR lasers (atomic probe and Raman lasers) are phase locked to the cavity to have a well-defined detuning with the cavity for probing the atomic population and driving Raman transitions inside the cavity. Apart from the lasers described above, there are two extra tampered amplifiers (TA) for amplifying for the MOT and Raman sideband cooling laser to achieve high enough optical power for trapping and cooling.

We frequency stabilize the lasers using the chain below, and we will explain each of these elements in the following sections. A complete drawing of the locking chain is shown in Fig. 3.4.

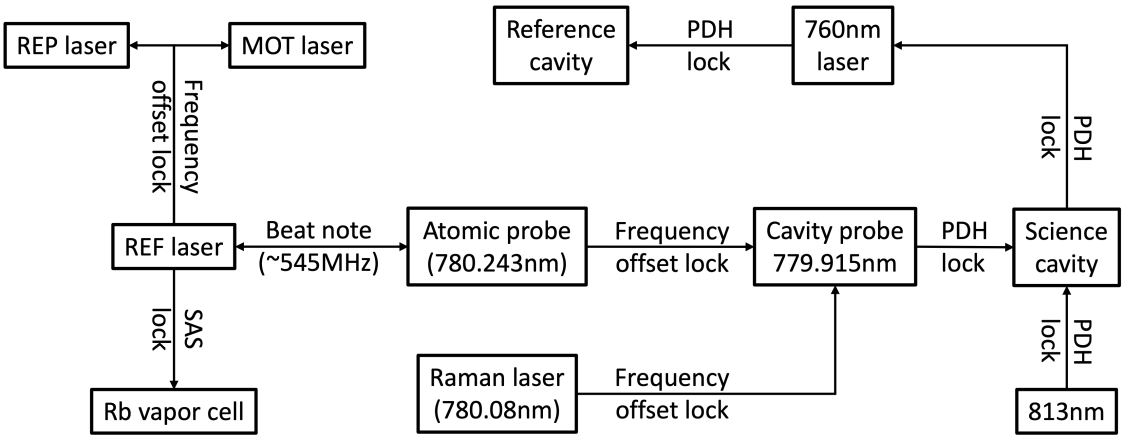

Figure 3.4: Locking chain for stabilizing all laser frequency.

3.4.2 REF, MOT and REP lasers for laser cooling

The REF laser is frequency stabilized to the ^{85}Rb $|F = 3\rangle \rightarrow |F' = 4\rangle$ transition with modulation transfer spectroscopy [46]. The laser is a grating ECDL to which we apply both current and piezo tuning. We then stabilize MOT and REP lasers to the REF laser with frequency offset locks. For the error signal of the frequency offset lock, we first overlap two lasers on a fast photodiode (Hamamatsu G4176 [3]) to measure the beatnote, and send the beatnote into a phase-frequency detector (PFD) with a RF frequency reference generated by direct digital synthesizer (DDS.) The PFD (TJ-005)is made by JILA electronic shop, based on HMC-440.

One of the lasers (MOT laser) is mainly for driving the cooling transition connecting $|F = 2\rangle$ ground state and the excited states. The other (REP laser) is mainly connecting $|F = 1\rangle$ to excited states for re-pumping. By using offset frequency locks, we can flexibly tune the laser frequencies by changing the reference RF frequency sent into the PFD. For reference, the laser frequencies can jump by 500 MHz and the lock can recapture within 50 μs. With this agile frequency tuning ability, we can tune the two laser frequencies for various purposes (Doppler cooling, polarization gradient cooling, optical pumping, blowing atoms away, etc.)

3.4.3 813 nm laser for red-detuned lattice

We use a red-detuned 813 nm 1D lattice to load the atoms from the MOT into the lattice, such that all the atoms in the lattice are maximally coupled to the cavity mode. We directly lock a 813 nm laser to the science to create this 1D red lattice.

The 813 nm laser is a grating-style ECDL. In order not to heat up the atoms after releasing the lattice, we need to adiabatically ramp down the lattice depth, which is realized by a intensity servo as shown in Fig. 3.5. We use the transmission photodiode signal as the error signal for the intensity lock and feedback on an AOM that controls the power going into the cavity to ramp up or down the lattice depth.

[3] This product is now obsolete. We are now using a EO-4000 photodiode for the new phase lock setup.

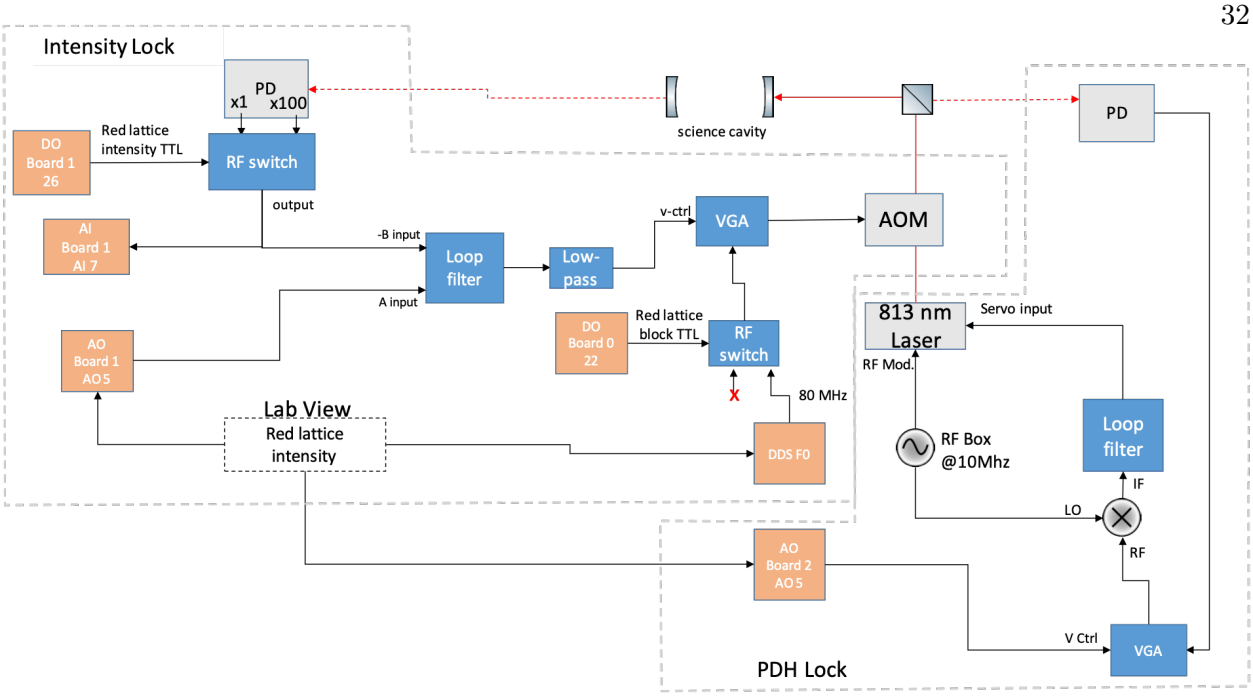

Figure 3.5: Optics for 813 nm laser.

3.4.4 760 nm laser for blue-detuned dipole trap

After releasing the atoms from the red-detuned lattice, we use a 760 nm laser to create a 1D dipole for trapping the atoms radially while allowing them to free fall. With a blue-detuned laser, the radial confinement is achieved by exciting the Laguerre-Gauss (1,0) mode [47], which looks like a donut with atoms trapped at center where there is no light. The "dipole trap" is realized by exciting multiple cavity longitudinal modes (separated by FSR), which cancel the standing wave when only exciting single cavity resonance. The same laser also serves as the frequency reference for the science cavity. The 760 nm laser is first stabilized to a passive reference cavity with PDH technique. The science cavity is then frequency locked to this 760 nm laser, such that the cavity resonances are stabilized.

We need only a few mW of optical power for establishing reasonable trap depths and performing PDH lock. However, this wavelength is not a popular option for commercial lasers, so we decided to try out a new ECDL design based on interference filter [48] and build it ourselves. This was an exciting project for me as a new graduate student who had very little experimental

experience. The diode was purchased from Eagleyard (RWE-0760-02010-1500-SOT12-0000) and a custom frequency filter (centered at 760 nm with 0.3 nm bandwidth) is purchased from Iridian. Here is the CAD drawing for the design:

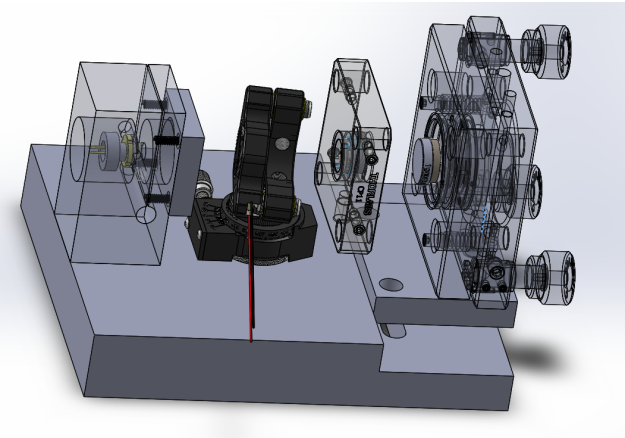

Figure 3.6: CAD drawing for 760 nm laser. The laser diode is installed in the diode holder on the left. The output light then pass through the interference filter mounted in the half-inch Thorlabs kinematic mount in the middle. This kinematic mount is installed on a rotational mount for adjusting the angle. The light is focused on an output-coupler (a mirror with 70% transmission) which then get collimated again, which improves the robustness against beam misalignment. The base is about 4-inches long for reference.

As the first interference filter ECDL built in JILA, the performance is satisfying and it has served till today. The mode-hop-free tuning range can go up to 23 GHz with the PZT driven by a high-voltage amplifier. Practically, we directly drive the PZT with the "PZT output" from the JILA loop filter, and can still get 7 GHz of mode-hop-free tuning range. I did a rough phase noise measurement on this laser. This is done by coupling and parking the laser on the side of the transmission peak of a 10 MHz linewidth cavity. The frequency (phase) noise of the laser is converted into the amplitude noise of the transmitted power. We can then analyze the power spectral density of the transmission signal to extract the frequency noise of the laser. With this approach, I was able to extract a Lorentzian linewidth of 40 kHz.

For exciting the donut-shape trap, we first modify the spatial mode of the laser with a fork-patterned phase plate before coupling into the cavity. The two diffracted beams out of the phase plate are both LG(1,0) mode. To verify the generation of the LG(1,0) mode, we overlap the LG

beam with a fundamental Gaussian mode colinearly , the interference pattern is shown in Fig. 3.7 with a spiral pattern resulting from the radial phase distribution of the LG beam.

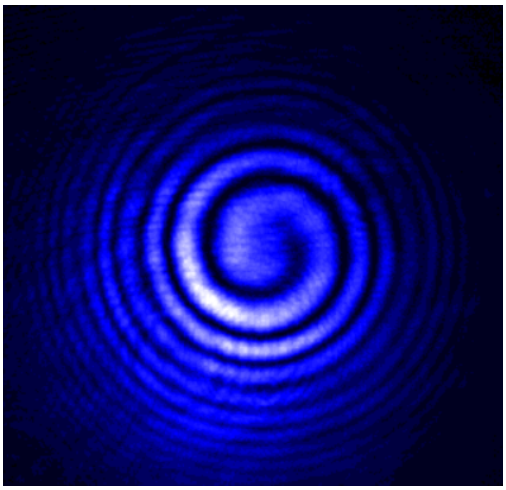

Figure 3.7: Interference between LG(1,0) mode and a Gaussian mode.

In reality, the spatial eigen mode of the cavity are Hermite–Gaussian (HG) modes instead of the Laguerre-Gauss modes, which originates from the deformation of the mirrors likely due to stress in how the mirrors are mounted.. In a perfect cylindrically symmetric cavity, LG(1,0) mode is a superposition of HG(1,0) and HG(0,1) mode [49] which have the same frequency.

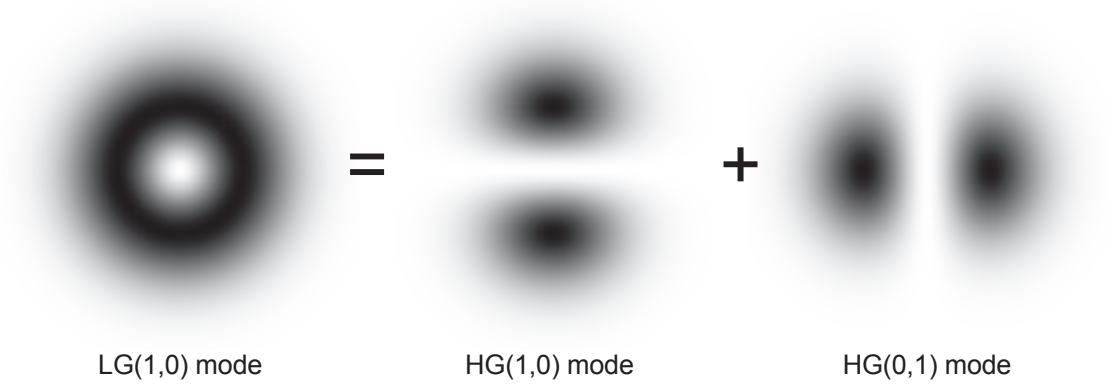

Figure 3.8: LG(1,0) mode is a superposition of HG(1,0) and HG(0,1) modes.

In our science cavity, the two HG modes are separated by about 350 kHz. In order to still create the donut-trap, we couple both diffracted beam from the phase plate to the cavity to

individually excite both the HG(1,0) and (0,1) mode. To compensate for the 350 kHz frequency splitting, one of the beams passes through two different AOMs. One AOM shifts the frequency up by 80 MHz, the other shifts the frequency back down by 79.65 MHz to introduce a 350 kHz frequency difference from the other beam. To create the PDH error signal, the other beam pass through an EOM to create sidebands, and the polarization is rotated by 90°. The two beams with orthogonal polarizations are combined with a polarizing beam splitter (PBS) before being coupled into the science cavity. For canceling the standing wave, we use a fiber EOM to create sidebands with frequency separation matching the cavity free-spectral range (FSR). By exciting multiple cavity longitudinal mode [50][G], we are able to cancel the axial variation of the trap depth around the center of the cavity to allow the atoms free-fall while being guided at all time. All associated optics are shown below.

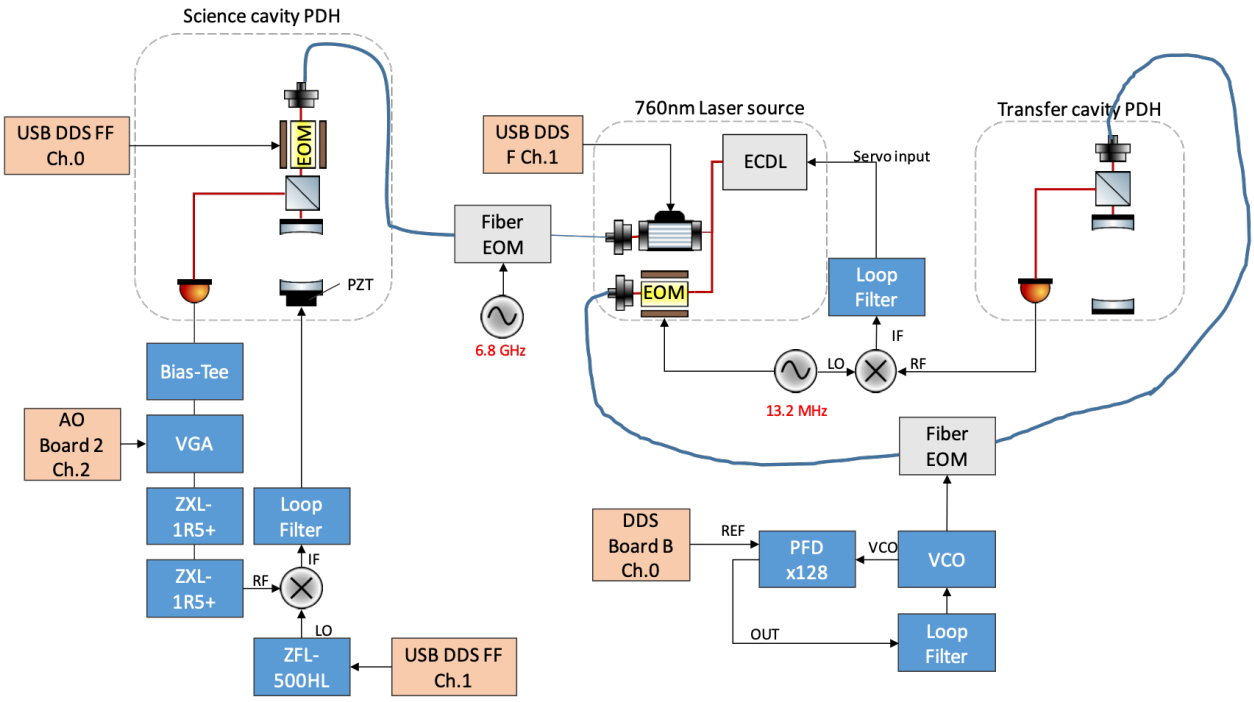

Figure 3.9: All optics for 760 nm laser.

3.4.5 Narrowing laser linedwith with optical feedback

The linewidth of our high-finesse cavity is about 50 kHz which is narrower than most of the lasers either commercially or home made. Over the years, we have learned our lessons that injecting a broader laser into a narrow cavity is always a bad idea. It can cause problems from driving parametric heating to low-efficiency probing and exciting unwanted two-photon transition, etc. Eventually, we identify three different lasers that we really need to narrow down the linewidth. They are atomic probe, cavity probe and the Raman lasers.

The specific use of these lasers will be described later. I will first focus on the technique we use for narrowing the linewidth. This trick is also called self-injection-locking which has been re-discovered by many people overtime. We first learned it from Vuletić group [51, 52]. The main idea is picking off some of the optical power and then sending it back to the laser diode. In this setup, one can intuitively (although not rigorously) understand it as building an extra cavity for further selecting (narrowing) the lasing mode. The laser frequency is then dominated by the external cavity length (with higher pulling coefficient) but not the laser current, and therefore we need to feedback on the optical feedback path length for stabilizing the laser frequency.

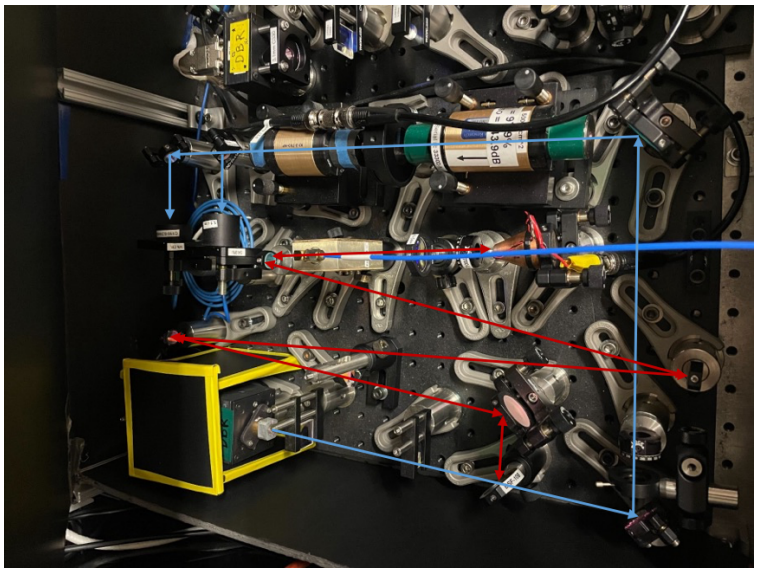

Figure 3.10: Atomic probe optical feedback narrowing setup. Blue lines label the output path, red lines label the feedback path.

To achieve wide dynamic range while maintaining fast actuation, we decide to use a piezo-actuated mirror for slow feedback and a free-space EOM for fast feedback. An example setup is shown in Fig. 3.10. The PZT-actuated mirror is formed by gluing a tiny hand-cut mirror [4] to a fast PZT (Thorlabs: PA3CKW) and a lead-filled copper mount [53] to increase the bandwidth, as shown in Fig. 3.11.

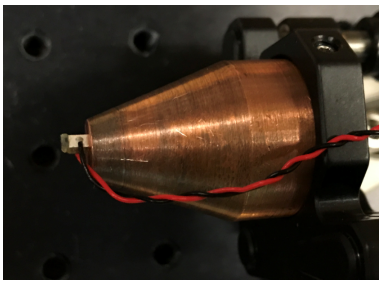

Figure 3.11: PZT-actuated mirror for reflecting the picked off light.

To verify the performance, the transfer function (i.e. bandwidth and detrimental mechanical resonances) can be easily measured by a Michelson interferometer.

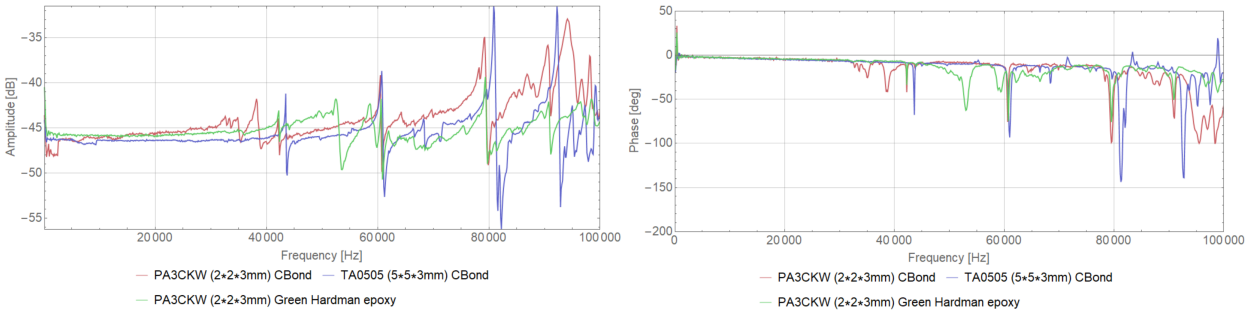

Figure 3.12: Transfer function for the PZT-actuated mirror with the amplitude response on the left and the phase response on the right. Different colors correspond to different choices of piezo and bonding technique with CBond stands for crystal bond. Gluing PA3CKW piezo to the mount with the Hardman epoxy gives the best performance with no obvious resonance up to 50 kHz.

The most tricky part is to accommodate the fast feedback on the EOM and the slow feedback on the PZT-actuated mirror. For that, I need to individually estimate the effective gain (frequency change given feedback voltage) for both the EOM and PZT-mirror, and tune the relative ratio

[4] A new batch of tiny mirrors (1 mm by 1 mm by 1 mm in size) are cut by the clean room with a dicing machine.

between the two with a homemade voltage divider and frequency filter to eventually have a stable feedback loop.

For characterizing the linewidth of the narrowed lasers, we first form a beanote between two narrowed lasers and send the beannote into a microwave delay line interferomter to turn the frequency noise on the input signal into output voltage noise and measure the voltage power spectral density. The Lorentzian linewidth is measured to be about 900 Hz [5] , which roughly agrees with direct linewidth measurement fitted from the beatnote spectrum.

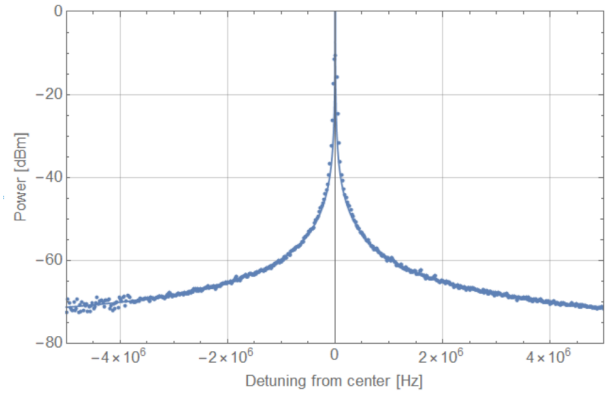

Figure 3.13: Beatnote between two different narrowed lasers.

3.4.5.1 Active stabilization for improving stability

Though having narrow linewidth, this optical feedback setup is not very stable. The reason is due to the free-running laser diode. Because the laser current/temperature is not being stabilized, the gain profile of the laser might drift overtime. If the drift is big enough as compared to the FSR of the "feedback cavity", different lasing mode will start to compete with each other and eventually drop the lock. Practically, the three narrowed lasers can stay locked for about 30 minutes after re-locking.

One way to improve the stability is to feedback/feedforward on the laser current such that the laser gain profile can follow the lasing mode selected by the "feedback cavity". Inspired by the

[5] The relative linewidth between the two lasers are measured to be 1800 Hz. The two lasers are assumed to performs the same.

PDH technique, we came up with a novel scheme for this active stabilization of the laser current. The setup is shown in Fig. 3.14. The rough idea is that, one can modulate the laser current at high frequency (70 MHz in our case, 150 MHz is the FSR of "feedback cavity"), pick off some of the light reflected by the feedback mirror, detect the signal on the photodiode and demodulate it with a local oscillator to get the error signal.

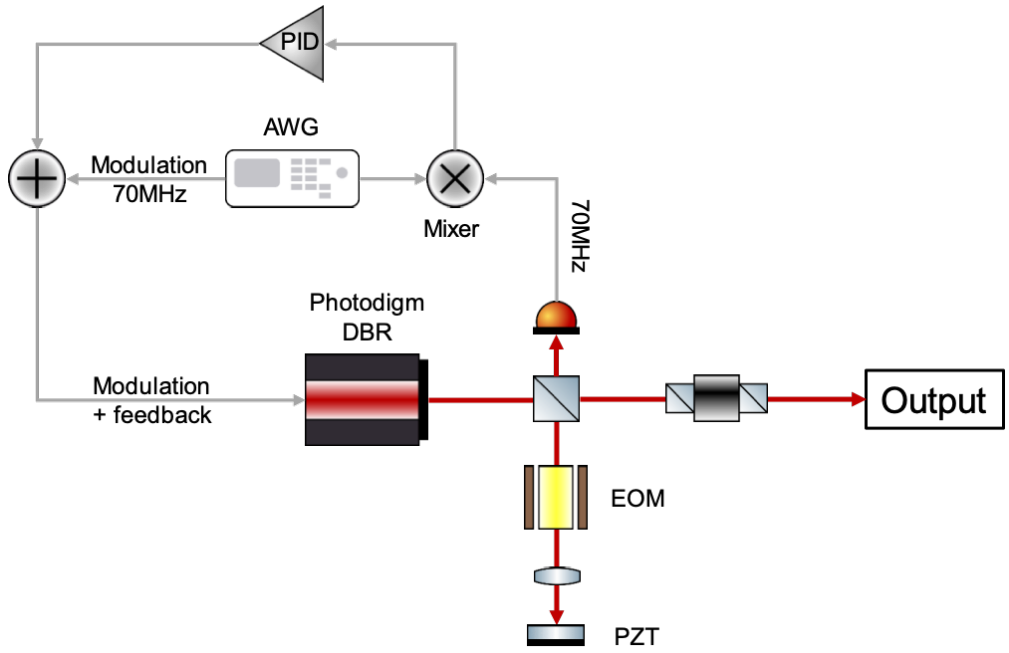

Figure 3.14: Setup for active stabilization

By scanning the laser current, an error signal (Fig. 3.15) can be found for active stablization of the the DBR free running laser frequency (via tuning the current) to the resonance frequency of the external feedback path.

For centering the gain profile to the resonance of the "feedback cavity", we need to lock the laser current to the zero-crossing of the error signal. One might also ask, what happens if one does not lock to the zero of the error signal? To answer this question, we lock to different offset voltage and realize the laser linewidth will increase when not locking to the center.

Apparently, the laser linewidth change with the alignment between the gain profile and the "feedback caity resonances". Another test for showing improved stability is to perturb the

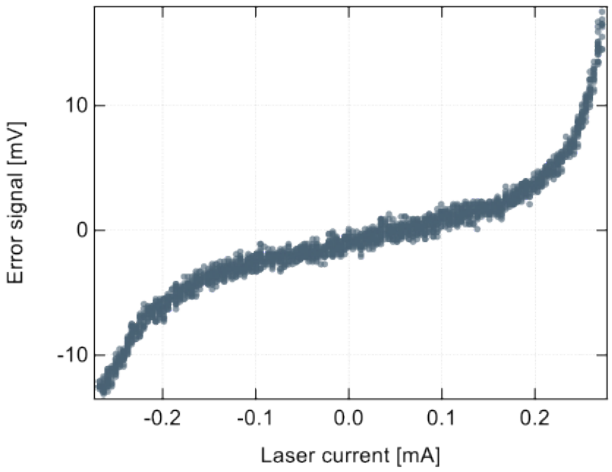

Figure 3.15: Error signal for active stabilization.

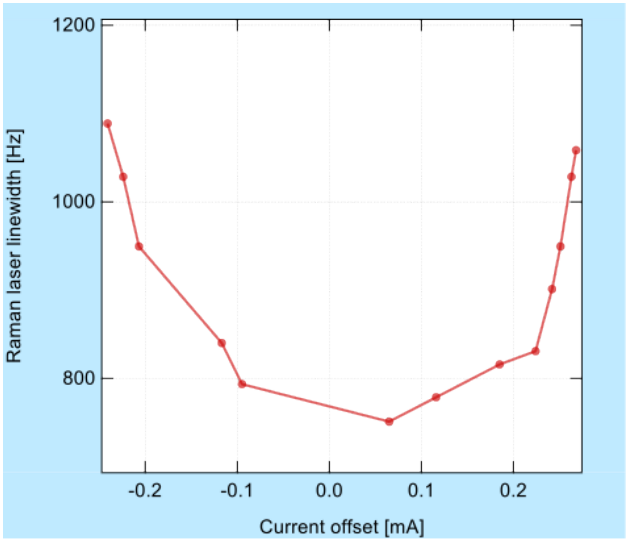

Figure 3.16: Measured laser linewdith when locking to different offset.

current/temperature of the laser and see the response of the laser with and without the active stabilization. As shown in Fig. 3.17, the robustness against temperature change is improved by 30 times. Without the stabilization, the laser will drop lock under a change of 0.016 degree Celsius. This number is improved to 0.5 degree. About the same amount of improvement can also be seen by the change of laser current. Now the laser can stay locked over 12 mA change of laser current as compared to only 0.3 mA before.

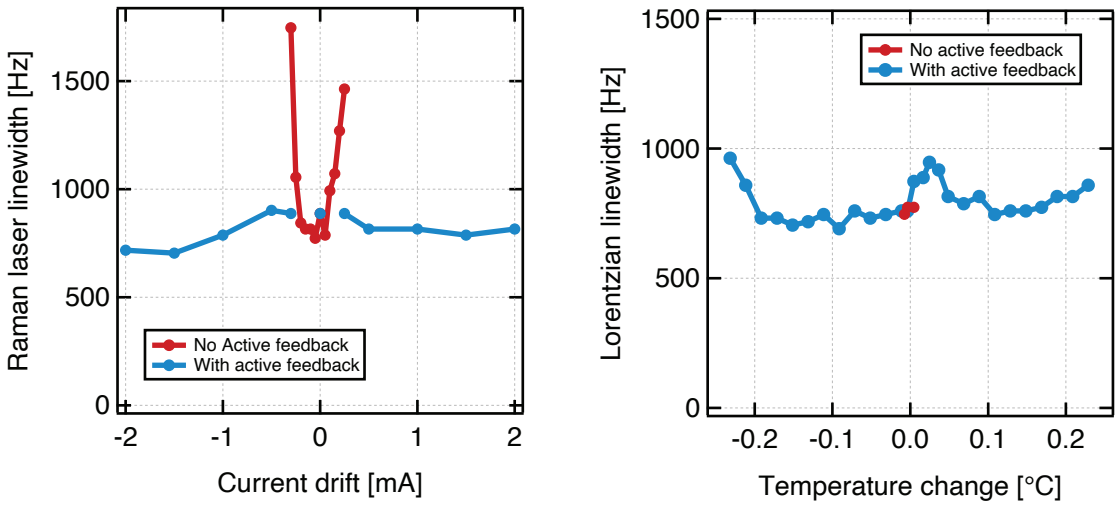

Figure 3.17: Laser linewidth response to change in current/temperature with/without active feedback.

This extra active stabilization can keep the narrowed laser locked almost indefinitely while maintained being narrowed. However, this technique is not being applied at the moment limited by the space and resources. In the future, one could integrate a low-frequency loop filter circuit and a VCO (frequency source) into a small box to further simplify the setup.

3.4.6 Cavity Probe: tracking bare cavity resonance

We need to send multiple laser tones that are close to atomic resonance into the science cavity for manipulating or probing the atomic states. These laser tones are only applied for short amounts of time (25 μs to few ms), otherwise they will cause unwanted scattering or AC Stark shift on the atomic states. However, they need to be frequency stabilized to the cavity throughout the whole sequence. In our experiment, we solve this problem by locking a laser (cavity probe) to a cavity mode that is far from atomic transition, and then stabilize the other close-detuned lasers to the cavity probe.

The complete optics setup for cavity probe laser is shown below in Fig. 3.18.

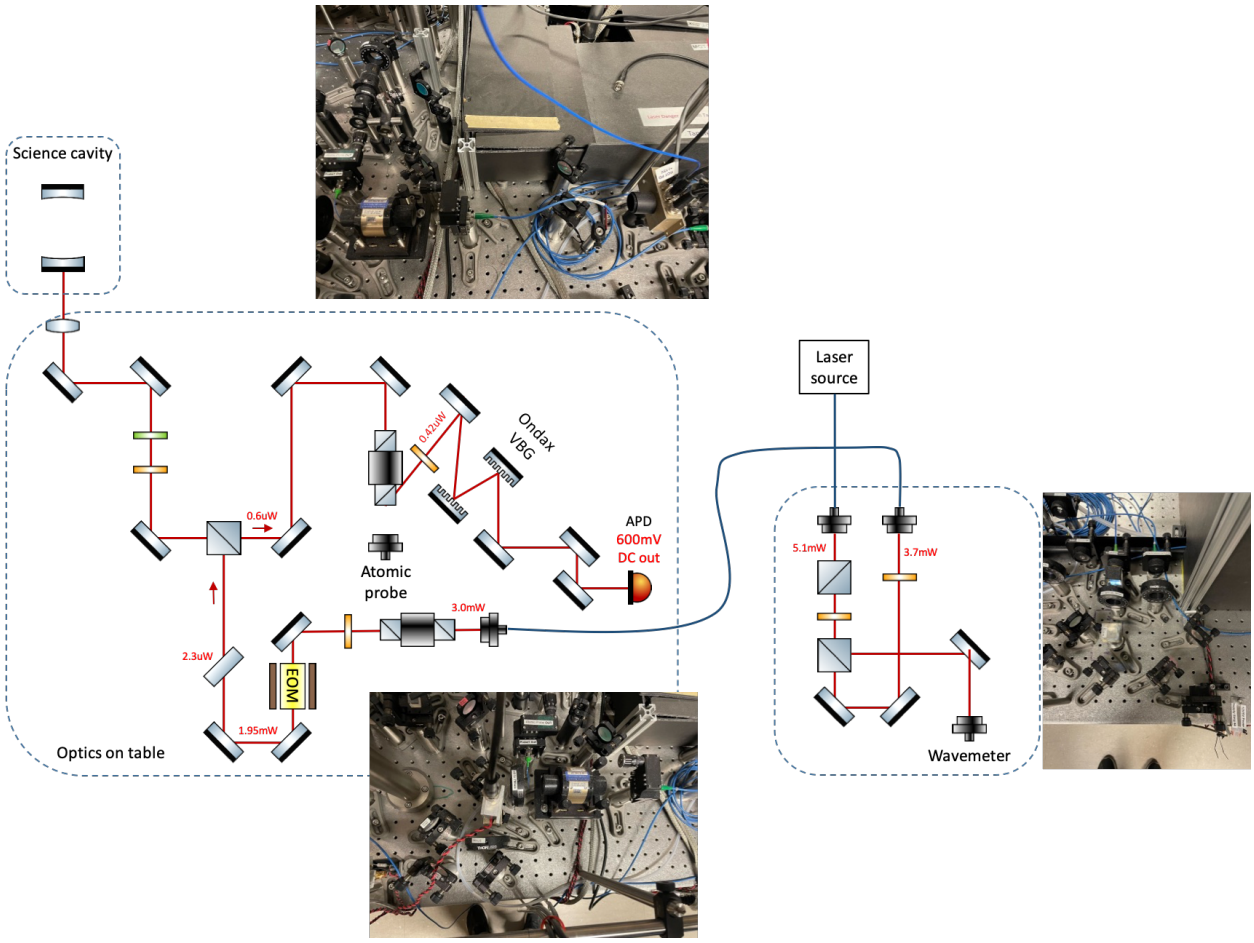

Figure 3.18: All optics for cavity probe laser.

The cavity probe wavelength is chosen to be 779.915 nm (160 GHz away from atomic tran-

sition) to reduce the perturbation on the atoms. The frequencies of cavity probe, atomic probe and Raman laser are summarized in Fig. 3.19. For bridging the huge frequency gap (>100GHz) between cavity probe and atomic probe or Raman lasers, we first send the cavity probe laser into a fiber-coupled EOM. The EOM is driven by 13.6 GHz with high modulation index, which creates reasonable amounts of power at the 7th and 12th order sidebands. These two sidebands are closer to the atomic probe and Raman laser frequency. We then overlap the fiber EOM output with atomic probe and Raman laser to form beatnotes for the frequency offset locks.

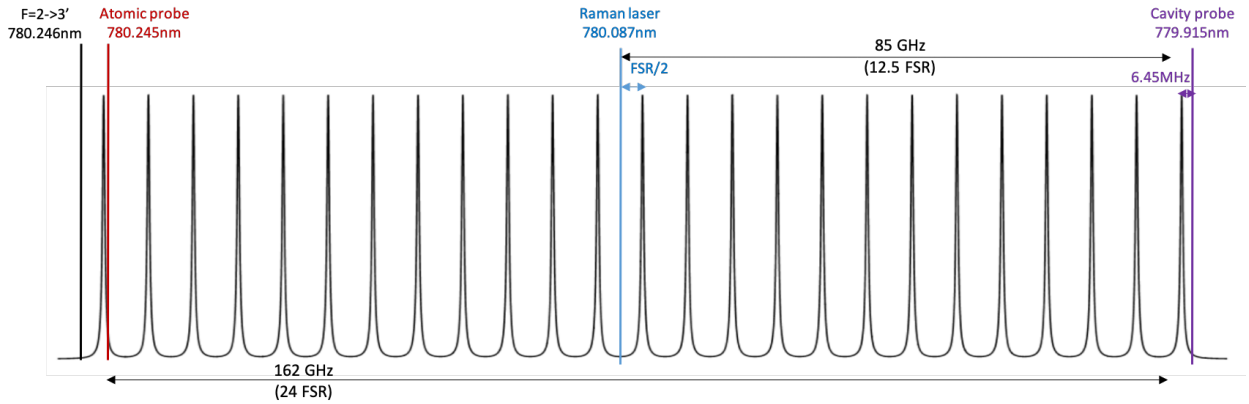

Figure 3.19: Frequencies of all three laser relative to atomic transition and cavity resonances. The 6.45 MHz is the FM modulation frequency for creating PDH sidebands on cavity probe laser.

The large detuning (160 GHz) of the cavity probe laser is chosen to reduce the differential AC Stark shift between the two hyperfine levels, and to avoid unwanted Bragg scattering off the small intracavity field. Furthermore, in order to lower the intra-cavity power of the cavity probe, we use an avalanche photodiode for detecting the retro-reflected beam and lock to the sideband created by the EOM. In conventional PDH lock setup, one locks the carrier of the laser to the cavity resonance. However, the slope of the PDH error signal at the sideband frequency is only a factor of 2 lower as compared to carrier regardless of the modulation index. By locking to the sideband, we can afford much lower intra-cavity optical power while allowing the carrier to act as a heterodyne reference that amplifies the fundamental photon vacuum noise above the technical noise floor of the photodiode. Specifically, in our setup, we send only 200 pW power into the cavity (1 μW for

carrier and 200 pW in the sideband) while having the relative frequency fluctuation between the cavity probe and the science cavity to achieve a QND readout noise floor of 1 kHz.

Here is the optical setup forming a beatnote between cavity probe and atomic probe before moving to X1B30. After moving the experiment, we decide to rebuild the beatnote setup with fiber splitter (Thorlabs, PN780R5A1) and fiber coupled photodiode (Thorlabs, DX12DF), which should in principle be much more stable.

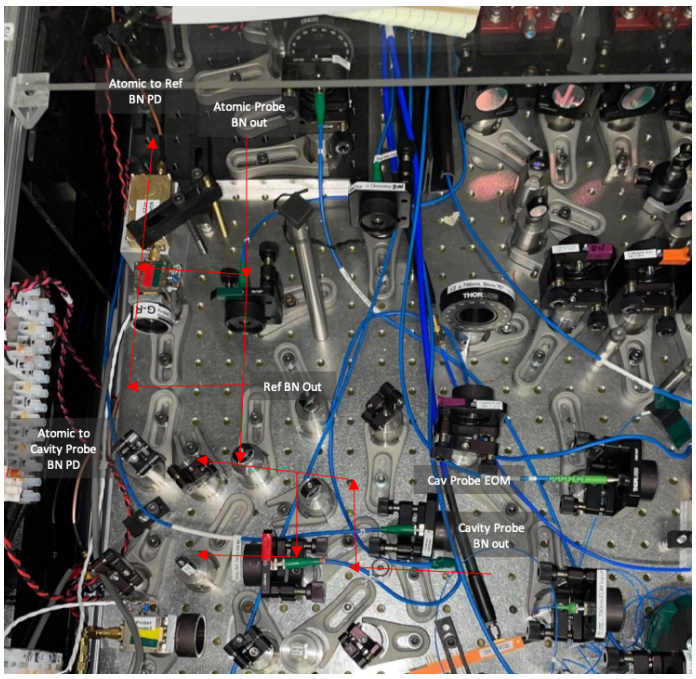

Figure 3.20: Atomic probe to cavity probe beatnote setup.

3.4.7 Atomic probe for homodyne detection

Atomic probe is the most "busy" laser in our experiment. The frequency is set to be close to ^{87}Rb $|F = 2, m_F = 2\rangle \rightarrow |F' = 3, m'_F = 3\rangle$ transition with the wavelength around 780.24 nm. We primarily use it for probing the dressed cavity resonance with a homodyne detection setup. For the momentum-exchange interaction experiment, we also use the same laser for driving Bragg rotation and the cavity-mediated interaction. The frequency of this laser is tuned with AOM, EOM or jumping frequency offset lock in different cases. The complete optical setup can be found below

in Fig. 3.21.

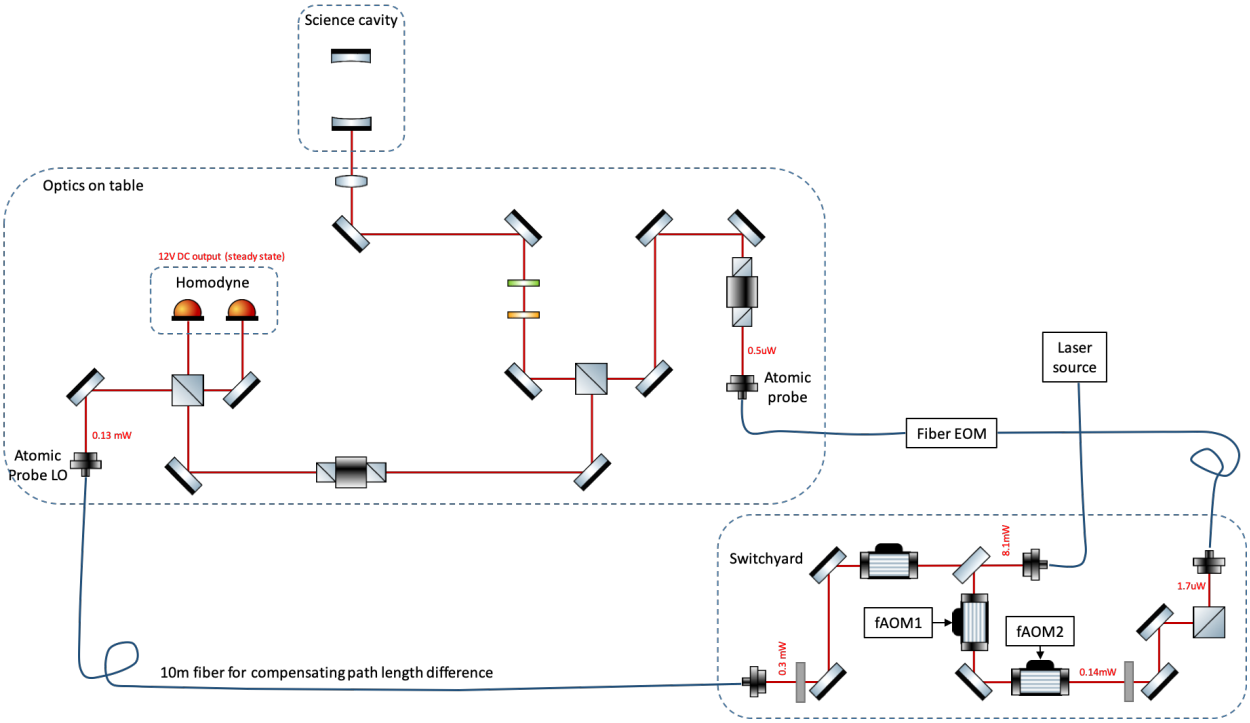

Figure 3.21: All optics for atomic probe laser.

For homodyne detection, we first split the atomic probe laser into two paths. One goes to the cavity with the retro-reflected beam overlapped with the other beam (local oscillator, LO) to form the homodyne signal at the detector. The LO beam is shifted by 80 MHz from the original atomic probe laser. For the beam going into the cavity, it first passed through a fiber-EOM driven by 80 MHz. The 80 MHz EOM sideband then forms the homodyne signal with the LO beam. The 80 MHz beatnote between the carrier tone and the LO beam is then compared with a reference 80 MHz signal, to detect the relative path length fluctuation between the two paths. The path length drift is then corrected by changing the VCO frequency (around 80 MHz) that drives the AOM for the LO beam, to keep the relative phase between the LO and atomic probe beam stable.

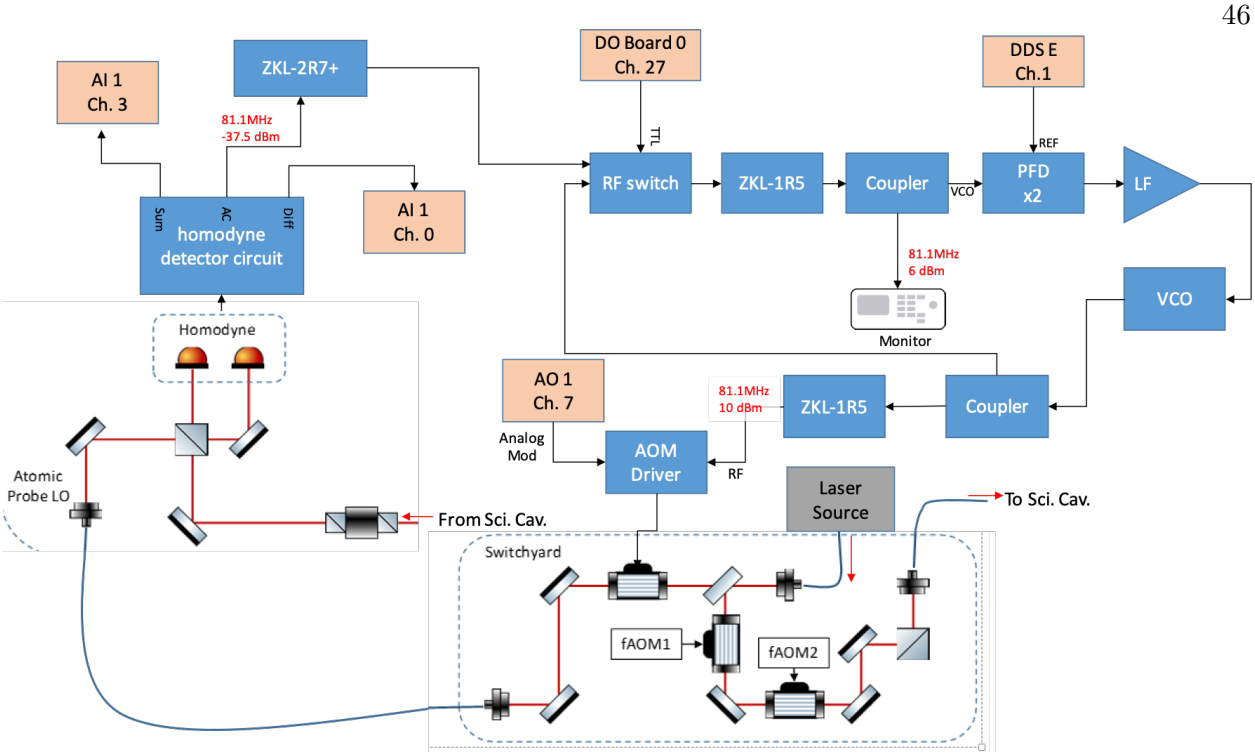

Figure 3.22: Path length stabilization for atomic probe.

3.4.8 Raman laser for driving two-photon transition

We have a dedicated laser (Raman laser) for driving the velocity-selective two-photon Raman transition connecting $|F = 1, m_F = 0, p_0 - \hbar k\rangle$ and $|F = 2, m_F = 0, p_0 + \hbar k\rangle$. The wavelength of the Raman laser is set to be 780.08 nm, which is 80 GHz from the atomic transition. This large detuning reduces the amount of free-space scattering when driving the two-photon transitions. Similar to the atomic probe laser, the Raman laser is also frequency stabilized to the cavity probe laser, such that the laser frequency is stable to within 1 kHz relative to the science cavity.

Starting from the Raman laser output, the laser light is frequency modulated by a fiber EOM at around 3.417 GHz to create two sidebands with separation matching the hyperfine splitting (6.834 GHz) plus the change in kinetic energy (about 500 kHz) between the two momentum states. With the cavity FSR=6.788 GHz close to the atomic hyperfine splitting, the two Raman laser sidebands are symmetrically detuned from two neighboring cavity longitudinal modes by ± 23 MHz to reduce FM to AM conversion, which could cause variation in the two-photon Rabi frequency

and drive unwanted Bragg transitions to other momentum states. With 5 mW of optical power incident on the cavity, we are able to achieve up to 15 kHz of Rabi frequency for the two-photon Raman transition.

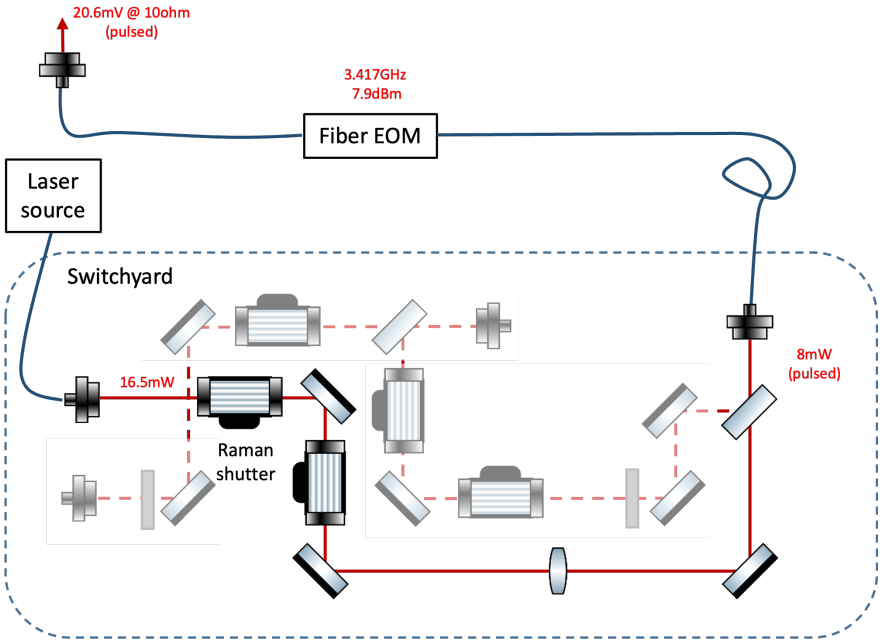

Figure 3.23: Beam path for the Raman laser.

3.5 Microwave and RF system

Other than the generic microwave signal which could be generated by direct digital synthesizer (DDS) and arbitrary waveform generator (AWG), there are three microwave signals that require special engineering. One is the low-noise microwave signal at around 6.834 GHz for driving the hyperfine transitions. The other two are around 3.417 GHz and 500 kHz for driving Raman and Bragg transition, which require agile phase/frequency control and the ability of frequency chirping. Finally, we would also like to drive microwave, Raman and Bragg transitions in a phase coherent way with respect to each other.

Driving Bragg rotations between $|p_0 - \hbar k\rangle$ and $|p_0 + \hbar k\rangle$ requires two different laser tones separated by the two-photon Doppler shift $\omega_z = 2kv_0$ where $v_0 = p_0/m$. These two tones are

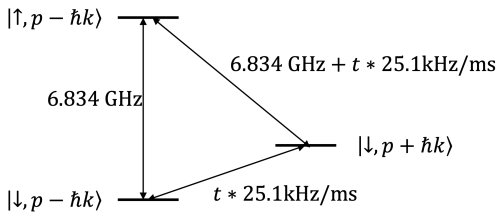

Figure 3.24: Microwave, Raman and Bragg transitions connecting three different energy levels

generated by first red shifting the atomic probe frequency by 75 MHz with one acousto-optic modulator (AOM) and then blue shifting it back with another AOM driven with two radio frequency (RF) tones at $\omega_{\mathrm{RF1}} = 75$ MHz and $\omega_{\mathrm{RF2}} = 2\pi \times 75 - \omega_z$ MHz. The phase of the Bragg rotation $\phi_{\mathrm{B}} = \phi_{\mathrm{RF2}} - \phi_{\mathrm{RF1}}$ is defined by the relative RF phases of ω_{RF2} and ω_{RF1}. To compensate the changing Doppler shift due to the free-falling, the frequency separation between the two tones are chirped by 25.11 kHz/ms with a DDS (AD9959) in linear frequency ramp mode.

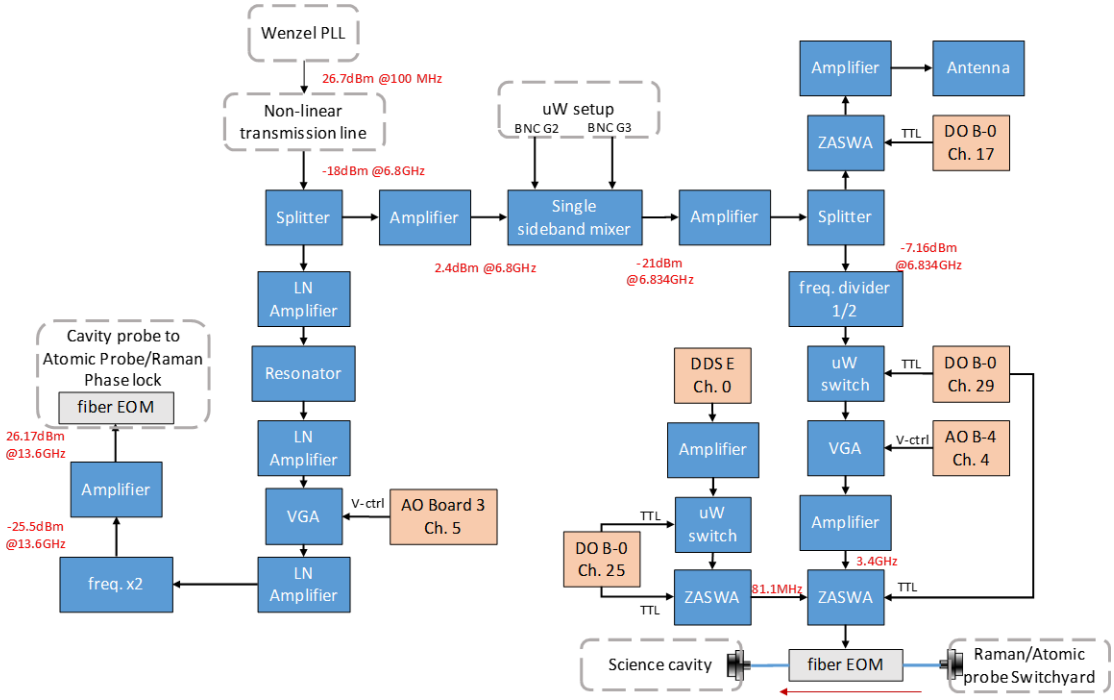

Figure 3.25: Microwave chain.

For driving the interactions, we need two tones offset by $2\omega_z$ with the separation chirped by 50.22 kHz/ms. This is again realized by first red shifting the atomic probe by 75 MHz with one

AOM and then blue shifting it back with another AOM. In this case, the second AOM is driven by two RF tones at ω_{RF1} and $\omega_{\mathrm{RF3}} = 2\pi \times 75 - 2\omega_z$ MHz. Here, $\omega_{\mathrm{RF3}} = 2\omega_{\mathrm{RF2}} - \omega_{\mathrm{RF1}}$ is generated by first frequency doubling ω_{RF2} then mixing with ω_{RF1} to shift the frequency back down after proper frequency filtering. By doing so, we maintain the differential phase $\phi_{\mathrm{int}} = \frac{\phi_{\mathrm{RF3}} - \phi_{\mathrm{RF1}}}{2} - \phi_{\mathrm{B}}$ between the Bragg rotations and the interactions stabilized. This differential phase can also be rapidly controlled by the RF phase of ω_{RF2}.

3.5.1 Generation of low-noise 6.8 GHz signal

A detailed description can be found in [54][G], the main idea is to start with a 100 MHz signal generated by a low-noise crystal oscillator (Wenzel ULN series) and then perform frequency multiplication and frequency filtering to eventually reach 6.8 GHz. The low-offset-frequency noise and the long-term stability is improved by locking the crystal oscillator to a 10 MHz Rb frequency standard (SRS FS725).

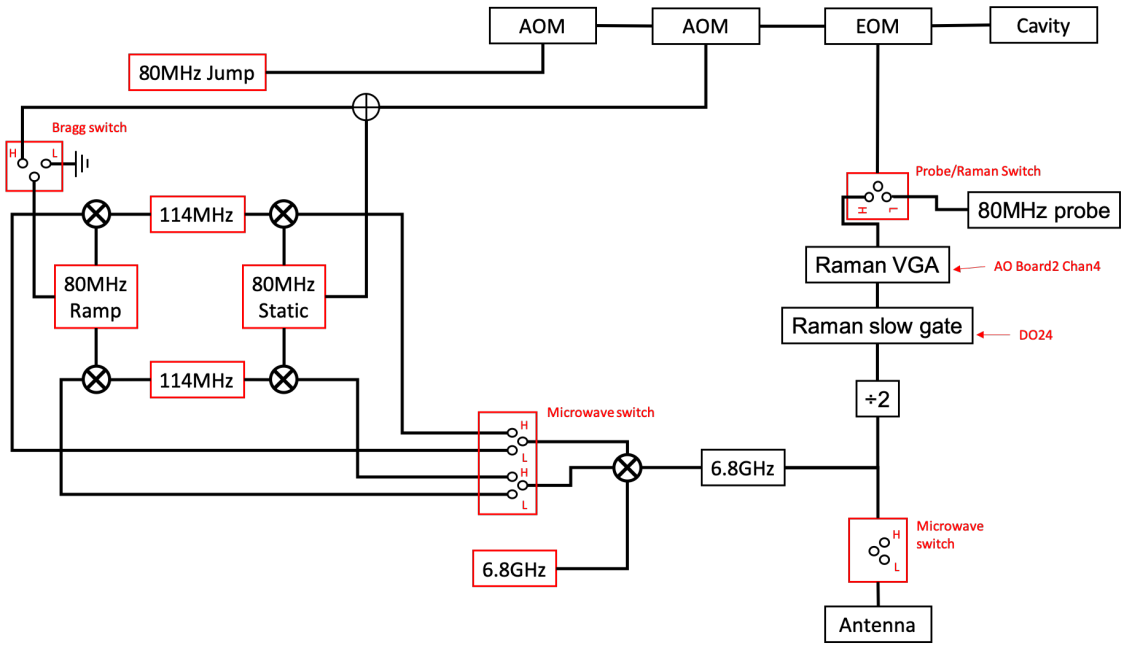

Figure 3.26: Microwave chain for coherent rotation for microwave, Raman and Bragg transiions.

3.5.2 Coherent rotations for all three transitions

In order to drive microwave, Raman and Bragg transitions all coherently with each other, we constructed a microwave frequency generation (shown in Fig. 3.26) chain to maintain the phase coherence between the three microwave signal.

3.6 Degenarate Raman side-band cooling

For cavity QED experiments, the atomic temperature is usually not a big concern since the equivalent energy is much smaller than the energy gap between the spin states. For atom interferometers, the effective axial temperature or the axial momentum distribution indeed matters a lot for the performance, which we will fix by performing velocity selection along the cavity axis. The radial temperature also turns out to be an important factor. It will affect the radial distribution of the atomic cloud and lead to a reduced atom-cavity coupling due to the spatial spread. The inhomogeneous atom-cavity coupling will then lead to an inhomogeneous Rabi frequency for driving the Raman transition along the cavity axis and causes a reduction of the interferometer contrast.

In our experiment, apart from the standard Doppler cooling, polarization gradient cooling and the Λ-enhanced gray molasses, we applied an an extra step of two-dimensional degenerate Raman sideband cooling to further reduce the atomic radial temperature to about 1 μK.

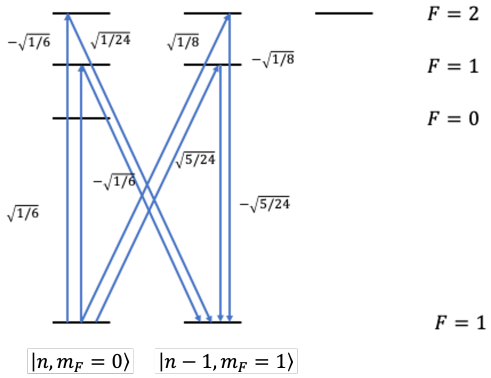

Figure 3.27: Relevant energy levels for ^{87}Rb.

Sideband cooling is a popular technique for trapped ion and optical tweezers experiments. In those systems, the strong trapping potential naturally create a harmonic trap for the atoms. The rough idea of sideband cooling is that one can use motional quanta to induce spin-flips and then use the optical pumping to serve as the dissipation process for resetting the spin state of the atom. Degenerate sideband cooling (RSBC) [55] is a version of this where the magnetic field difference between the spin states is degenerate with the trapping frequency. In our implementation, the trapping is also generated by the very same laser beams. Specifically, in our experiment, the atoms start in $|F = 1, m_F = 1\rangle$ and the cooling is done by driving a two-photon transition connecting $|F = 1, m_F = 1, n\rangle \rightarrow |F = 1, m_F = 0, n - 1\rangle$. A optical pumping beam is always on for pumping the atoms back to $|F = 1, m_F = 1\rangle$. All possible path for the two-photon transitions are shown in Fig. 3.27 with the numbers labeling the Clebsch-Gordan coefficient for each transition.

3.6.1 Polarization twisting

Optical lattices are usually formed by interfering two counter-propagating laser beams with the same polarization. However, in this configuration, the atoms are trapped at the node or anti-node of the standing wave where the electric field gradient goes to zero, which fails to drive the sideband transition that changes the parity of the motional atomic wave function.

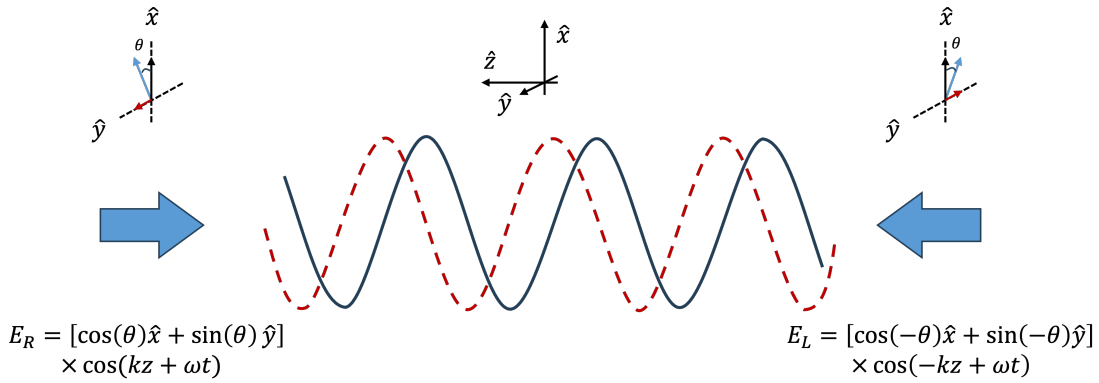

Figure 3.28: Polarization twisting for creating Raman coupling. The polarizations of the two counter propagating beams are rotated by a small angle θ (along the propagation axis) from $\hat{x}$. $\hat{y}$ is perpendicular to $\hat{x}$ and $\hat{y}$, which goes out of the paper. θ is set to be 10° in our experiment.

To fix this issue, we need to introduce polarization twisting to the two counter-propagating beams. Here is a 1D example of two counter-propagating beams with orthogonal polarization. The interference of the two beams will create two sets of lattices, one in plane and one out of the plane. For atoms trapped at the anti-node of the black standing wave, they also experience the strong electric field gradient coming from the other lattice.

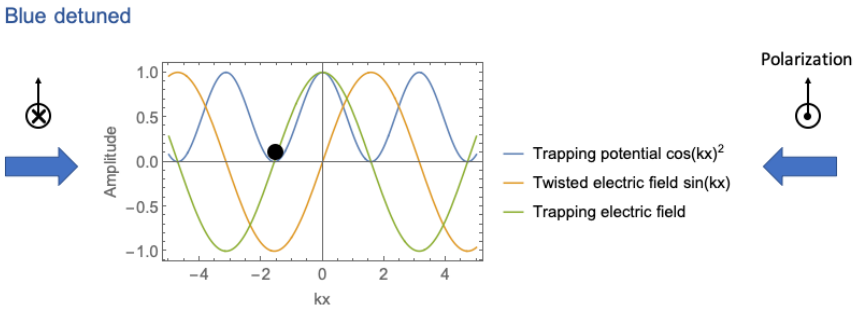

Figure 3.29: Polarization twisting for Blue-detuned beams

The example above is for red-detuning beams. Since we already have a background radial trapping from the 760 nm dipole trap, we decided to use blue-detuned beams (about 80 GHz from atomic transition) to further reduce the free-space scattering with the atoms trapped at the node of the lattice. The polarization twisting can still work for blue-detuning.

3.6.2 Two-dimensional lattice formed by three beams

In our experiment, in order to cool the atoms on both radial axes, we form a hexagonal 2D lattice with three different laser beams separated by about 120 degrees from each other, as shown in Fig. 3.30. Due to the constraint of space, we could not achieve exactly 120 degrees as the separations between beams, which could lead to a non-degenerate trapping frequency along the two axis $\hat{x}$ and $\hat{y}$. We purposefully introduce a power imbalance between the beams to balance the trapping frequencies.

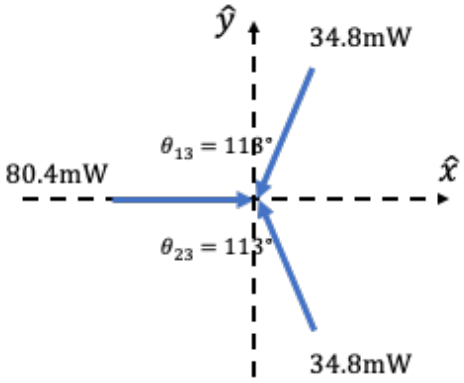

Figure 3.30: Three beams for Raman sideband cooling (RSBC.)

The pictures of the actual beam launchers (circled red) as shown in Fig. 3.31.

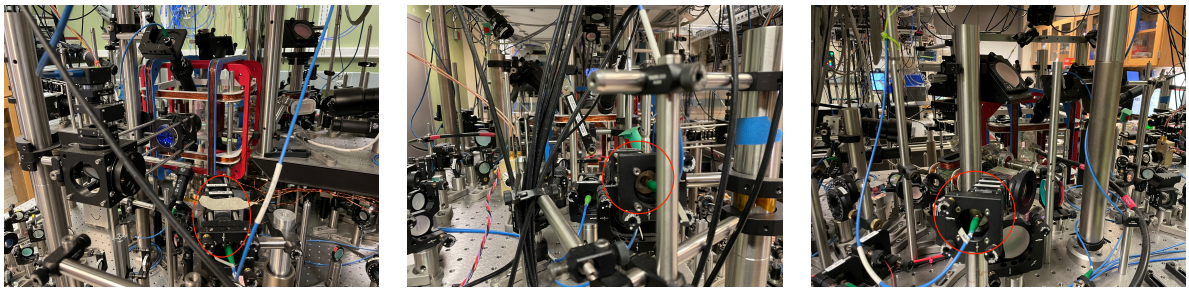

Figure 3.31: Pictures of three beams

3.6.3 Cooling sequence

Different from the free-space RSBC experiment, the atoms are also subjected to a background dipole trap in our case. After releasing the RSBC lattice, the atoms will start to accelerate towards the center of the cavity and heat up again. In other words, not only do we need to remove the kinetic energy of the atom, we also need to remove the potential energy.

As shown in Fig. 3.32 (horizontal axis is for time and vertical axis is for trap depth), we design a effective "delta-kick" sequence for increasing the on-axis density of the atom. In each cooling cycles,

(1) Raman beams create a strong lattice (compared to the radial confinement of the red lattice) to hold and cool the atoms to ground state of the lattice.

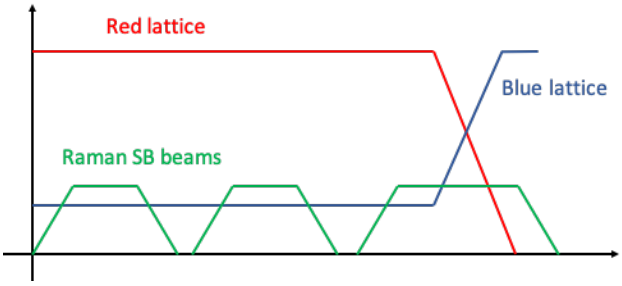

Figure 3.32: Timing sequence for RSBC.

(2) Releasing the Raman lattice adiabatically, atoms will regain kinetic energy due to the initial radial distribution.

(3) Wait a period of time that is approximately 1/4 of the radial trapping oscillation period.

(4) Adiabatically turn on the Raman lattice and sideband cool.

By repeating the above processes, we could eventually reduce both kinetic and potential energy to achieve a radial temperature of 0.7 μK which allows for better radial confinement.

3.6.4 Radial temperature measurement with dispersive shifts

The temperature measurements are usually done by time-of-flight imaging. Without relying on cameras, the high-finesse cavity can actually serve as a very high NA lens for "imaging" the radial distribution of the atom. In our experiment, we use the dispersive shift of the cavity for characterizing the radial temperature of the atoms.

Starting with all atoms trapped in the blue-detuned dipole trap, we turn off the trap and let the atoms start expanding radially. We then measured the cavity frequency shift after various delay times. Based on how fast the cavity frequency shift changes, we can estimate the radial temperature.

To derive the expression of the decaying dispersive shift, we start with the atom phase space

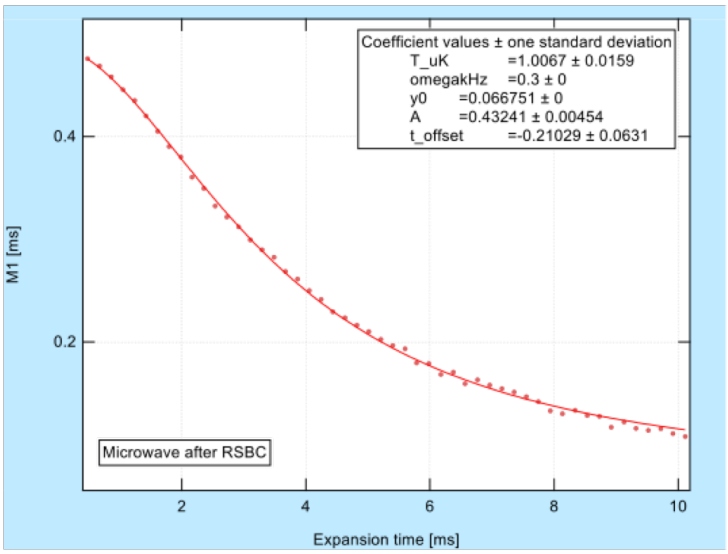

Figure 3.33: Dispersive shift decay as expansion time increases.

distribution (x, y, p_x and p_y are the positions and momentum along x, y axes)

$$P\left(x, y, p_x, p_y\right) = P_x(x)P_y(y)P_{p_x}(p_x)P_{p_y}(p_y) \tag{3.1}$$

$$= norm \exp\left(\frac{-\frac{1}{2}m\omega_r^2 x^2}{k_B T}\right) \exp\left(\frac{-\frac{1}{2}m\omega_r^2 y^2}{k_B T}\right) \exp\left(\frac{-p_x^2/2m}{k_B T}\right) \exp\left(\frac{-p_y^2/2m}{k_B T}\right), \tag{3.2}$$

where $norm$ is the normalization factor, ω_r is the radial trapping frequency, m is the mass of rubidium atom and k_B is the Boltzman constant. After time-propagating the distribution, the probability for finding an atom at position (x, y) at time t after the radial dipole trap has been turned off is

$$P(x, y, t) = \int P_x\left(x - \frac{p_x}{m}t\right) P_y\left(y - \frac{p_y}{m}t\right) P_{p_x}(p_x)P_{p_y}(p_y)dp_x dp_y = \frac{e^{-\frac{m\omega r^2}{2k_B T(1+\omega)}} m\omega^2}{2\pi k_B T(1+\omega t^2)}. \tag{3.3}$$

After integrating the atomic spatial distribution with the cavity mode profile, we have

$$f_{disp}(t) = \frac{m w_0^2 \omega^2}{4k_B T(1+\omega^2 t^2) + m w_0^2 \omega^2}, \tag{3.4}$$

where f_{disp} is the dispersive shift at time t, w_0 is the mode waist of the cavity, ω is the radial trapping frequency and T is the radial temperature of the atoms.

3.7 Relevant parameters for the experiment

The relevant parameters are summarized in the table below

Cavity Parameters	
Maximal single-atom vacuum Rabi splitting g	$2\pi \times 0.48(3)$ MHz
Bottom mirror transmission T_1	40 ppm
Top mirror transmission T_2	2 ppm
Estimated loss per mirror L	2 ppm
Linewidth κ	$2\pi \times 52(3)$ kHz
Finesse (780 nm)	130,000
Free spectral range	6.788GHz
TEM_{00} waist size w_0	72(1) μm
Cavity length	2.02 cm
Mirror radius of curvature	4.999(5) cm
Atomic Parameters	
Excited state decay rate Γ	$2\pi \times 6.06$ MHz
Ground state hyperfine splitting ω_{HF}	$2\pi \times 6.834$ GHz
Axial temperature after cooling T_{axial}	5 μK
Radial temperature before interferometer sequence T_{radial}	1.5 μK
Thermal RMS cloud radius r_{rms}	3.0(5) μm
RMS momentum spread after velocity selection σ_p	0.05 $\hbar k$

Table 3.1: Table for cavity and atomic parameters.

Chapter 4

Entanglement enhanced matter-wave interferometer

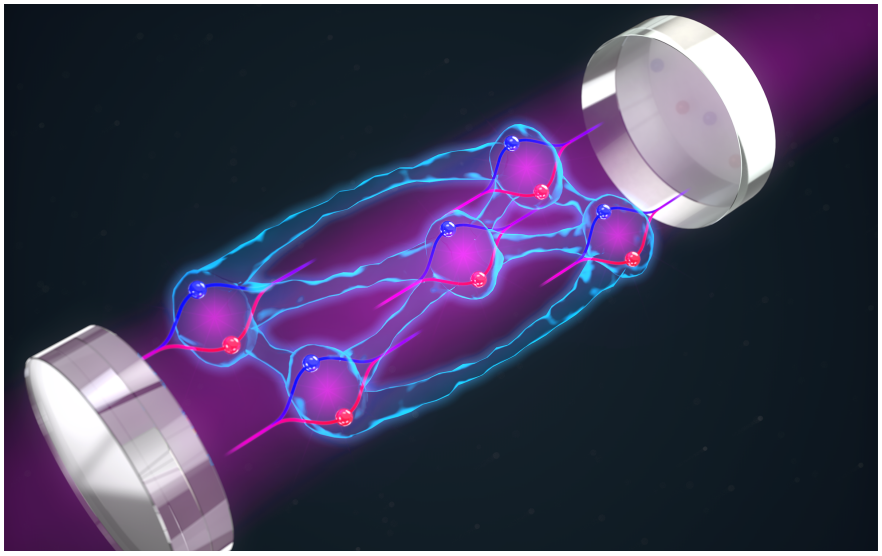

Figure 4.1: Artistic conceptualization of entanglement-enhanced matter-wave interferometer. Atoms (blurry blobs) are entangled to each other. Each atom can be spitted into two paths (colored as red and blue) and get recombined later. Credit: Steven Burrow

Light-pulse matter-wave interferometers exploit the quantized momentum kick given to atoms during absorption and emission of light in order to split atomic wavepackets so that they traverse distinct spatial paths at the same time. Additional momentum kicks then return the atoms to the same point in space to interfere the two matter-wave packets. Such matter-wave interferometers are exquisitely precise and accurate quantum sensors for a vast range of applications including inertial sensing and navigation [56, 19, 57], searching for dark matter[6, 5] and dark energy[22, 58], determination of fundamental constants and the most precise test of a physical theory to date [20,

21], geodesy, geophysics and mineral and hydrocarbon exploration[59], exploring general relativity with quantum probes [60, 61, 62], and detecting gravitational waves [63, 40, 64].

Quantum entanglement between the atoms allows the atoms to conspire together to reduce their total quantum noise relative to their total signal during the phase estimation process [16, 17]. Such entanglement has been generated between atoms and ions using direct collisional [27, 28, 65, 66, 67, 68, 69] or Coulomb [70, 32] interactions, with applications to entangled spatial interferometry in trapped geometries [27, 69] and mapping of internal entanglement onto momentum states[71].

We demonstrate for the first time, the realization of cavity-QED entanglement generation between the external momentum states of different atoms using two distinct approaches that both rely on the strong collective coupling between the atoms and an optical cavity. In the first approach, we realize cavity-enhanced quantum non-demolition measurements [25, 26, 72, 34] to essentially measure and subtract out the quantum noise. In the second approach, we utilize the cavity to mediate unitary interactions between the atoms to realize so-called one-axis twisting [16, 73, 74, 75, 76] or an all-to-all Ising interaction. Both approaches have been realized for generating as much as 18.5 dB of entanglement [26, 25], but only between **internal** states of atoms and with only the realization of directly observed enhancements in entangled microwave clocks [77, 78] and magnetometers [79].

4.1 Experimental setup and overview

Strong collective coupling to the cavity $NC \gg 1$ is the key requirement for both approaches to generate entanglement, where C is the single particle cooperativity parameter [38, 74, 80]. Previously, an interferometer was operated in a low finesse cavity [81, 82], to provide power build-up, spatial mode filtering, and precise beam alignment. Here, we achieve matter-wave interferometric control [3, 83] simultaneously with strong collective coupling $NC \approx 500$ by operating inside a high cavity finesse $\mathcal{F} = 1.3 \times 10^5$ with small mode waist $w_0 = 72\mu$m.

Our two-mirror cavity is vertically-oriented along $\hat{Z}$ (Fig. 4.2). The cavity has a power decay rate $\kappa = 2\pi \times 56(3)$ kHz, mirror separation $L = 2.2$ cm, and free spectral range $\omega_{\mathrm{FSR}} =$

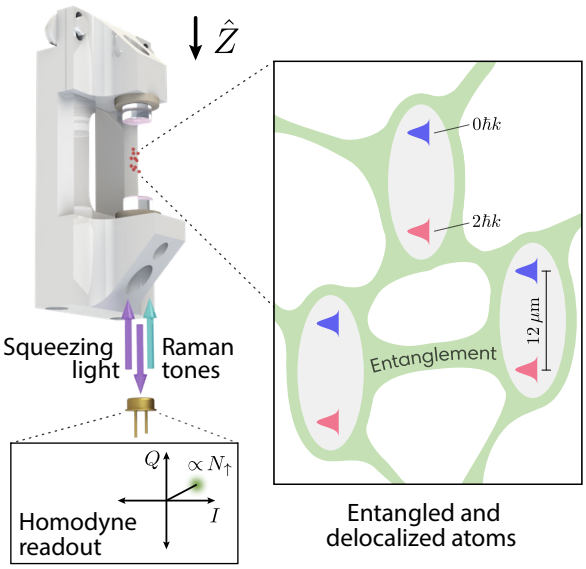

Figure 4.2: **Laser cooled rubidium atoms are trapped inside a high-finesse cavity.** The atomic wavepackets are split and recombined by driving two-photon Raman transitions to provide quantized momentum kicks to the atoms. **(inset)** Intracavity atomic probe light generates entanglement between the atoms via either one-axis twisting dynamics or quantum non-demolition measurements made by detecting the reflected atomic probe field with a homodyne detector.

$2\pi \times 6.7879$ GHz. Rubidium atoms are loaded into a red-detuned 813 nm standing-wave intracavity lattice and laser-cooled to a radial temperature of $0.7(3)\mu$K. The lattice is adiabatically reduced to allow the atoms to accelerate under gravity for a duration T_{fall}, guided tightly along the cavity axis by a hollow (Laguerre-Gauss LG_{01}-like) blue-detuned optical dipole guide[50] with thermal rms cloud radius of $r_{\text{rms}} = 3.0(5)\ \mu\text{m} \ll w_0$.

The generation and injection of the entanglement into a Mach-Zehnder matter-wave interferometer are shown by the space-time and Bloch sphere depictions in Fig. 4.3. Squeezing is first generated in the population basis, and then a Raman beam splitter pulse orients the squeezing for enhanced interferometer phase sensitivity. The two paths (red and blue) accrue a relative phase ϕ over time T_{evol}, the mirror pulse serves to reoverlap the wavepackets, and the readout beam splitter pulse creates interference that is read out as a population difference with sub-standard quantum limit sensitivity. Representative noise distributions are depicted on the Bloch sphere for various

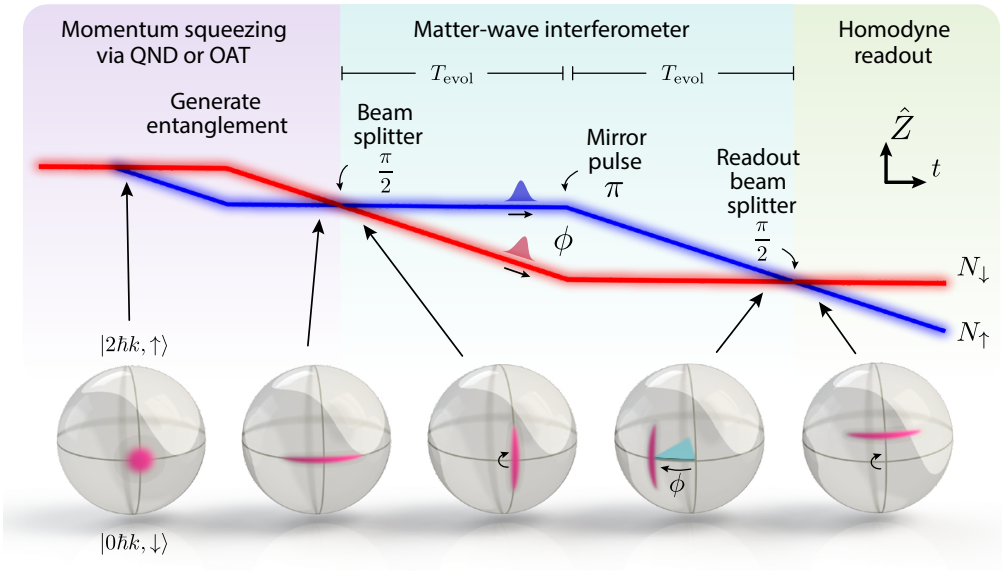

Figure 4.3: Space-time diagram and the corresponding Bloch sphere depictions for the entangled matter-wave interferometer.

points in the interferometer.

4.2 Manipulating atomic momentum states.

We manipulate matter-wave wavepackets using velocity-sensitive two-photon transitions with wavelength $\lambda = 780$ nm. The combined absorption and stimulated emission of photons imparts $2\hbar k$ momentum kicks along the cavity axis, where $k = 2\pi/\lambda$ and $\hbar$ is the reduced Planck constant.

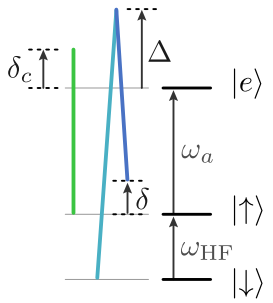

Figure 4.4: The empty-cavity resonance (green) is detuned by δ_c from the $|\uparrow\rangle \rightarrow |e\rangle$ transition ω_a. The Raman tones (blue) injected into the cavity drive a spin-changing $|\uparrow\rangle \leftrightarrow |\downarrow\rangle$ transition with two-photon detuning δ defined in a falling reference frame.

For Raman transitions in which both momentum and spin states are changed, we utilize the magnetically-insensitive ^{87}Rb clock states, $|\downarrow\rangle \equiv |F = 1, m_F = 0\rangle$ and $|\uparrow\rangle \equiv |F = 2, m_F = 0\rangle$, separated by the hyperfine transition frequency $\omega_{\mathrm{HF}} \approx 2\pi \times 6.835$ GHz. The driving laser's frequency is stabilized between two TEM_{00} longitudinal modes approximately $\Delta = 2\pi \times 85$ GHz blue-detuned of $|\uparrow\rangle \rightarrow |e\rangle \equiv \left|5^2\mathrm{P}_{3/2}, F = 3\right\rangle$. The cavity free spectral range is tuned such that two sidebands at $\pm\omega_R$ are approximately ± 23 MHz from resonance with the closest TEM_{00} mode when $2\omega_R = \omega_{HF}$. This configuration allows enough light to nonresonantly enter the cavity for a two-photon Rabi frequency $\Omega = 2\pi \times 10$ kHz. By injecting the Raman tones non-resonantly and with opposite detunings, we greatly suppress laser frequency noise from being converted into phase and amplitude noise inside the cavity. Such noise manifests as noise in the Raman rotations and undesired Bragg scattering to other momentum states.

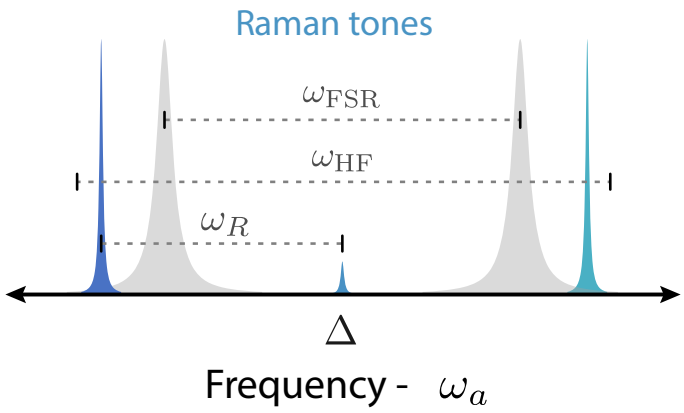

Figure 4.5: The Raman tones are derived from a laser locked between two adjacent TEM_{00} modes (grey) and modulated at $\omega_R \sim \omega_{\mathrm{HF}}/2$, leaving them detuned from the cavity resonances by ± 23 MHz, close enough to resonance to allow light to enter the cavity while also sufficiently detuned to avoid strong laser FM to intracavity AM and PM conversion that would interfere with manipulating the matter-waves with a precision below the standard quantum limit.

As the atoms fall under gravity inside the cavity, the relative Doppler shift for light propagating upwards versus downwards chirps linearly in time. We compensate this effect by linearly ramping the instantaneous frequency of the sidebands as $2\omega_R = \omega_{\mathrm{HF}} + \delta - b(t - t_{\mathrm{vs}})$ with

$b = 2kg = 2\pi \times 25$ kHz/ms with the local acceleration due to gravity $g = 9.8\text{m/s}^2$, δ the two-photon detuning in the falling frame of reference, and t_{vs} the time at which we will apply the first π pulse for velocity selection described below (see Fig. 4.5).

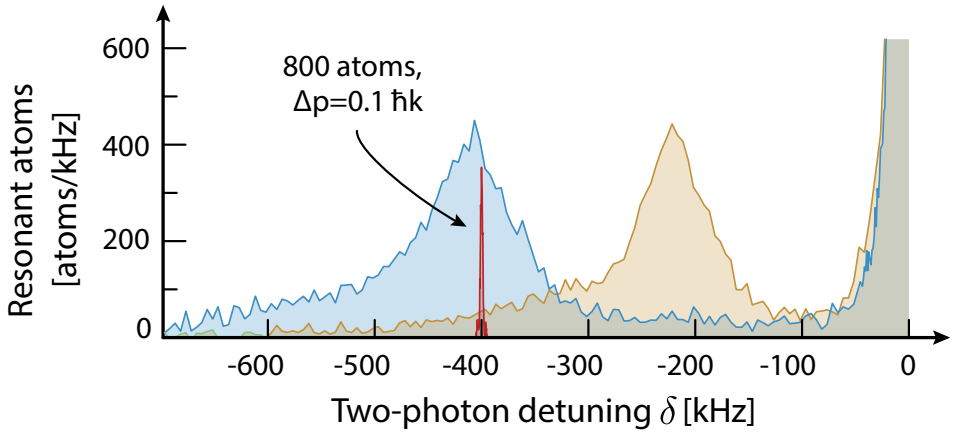

Figure 4.6: Atoms are prepared in $|\downarrow\rangle$ and allowed to fall for a duration $T_{\text{fall}} = 7.5$ ms (orange) or 15 ms (blue). The Raman coupling is applied at a fixed detuning δ, after which the number of atoms in $|\uparrow\rangle$ is measured, revealing the axial velocity distribution. The full-width half-maximum of both distributions corresponds to a momentum spread of $5\hbar k$, too broad for interferometry. During velocity selection, a group of about 800 atoms with rms momentum spread $\Delta p = 0.1\hbar k$ (red) are kept from the latter distribution while the rest are removed with transverse radiation pressure.

In Fig. 4.6, we show the initial axial velocity spectrum of the atoms as mapped out by inducing velocity-dependent spin flips. We use this same process to select atoms within a narrow range of initial velocities for coherent manipulation of matter-waves in the remainder of this work. After falling for $T_{\text{fall}} = 15$ ms, atoms are optically-pumped to $|\uparrow\rangle$, and the two-photon detuning is set to $\delta_{\text{vs}} = -400$ kHz to transfer a group of atoms to $|\downarrow\rangle$ from the center of the axial velocity distribution [84]. Atoms in $|\uparrow\rangle$ are removed by a transverse radiation pressure force. The velocity-selected atoms are returned to $|\uparrow\rangle$ with a Raman π pulse and the selection process is repeated, resulting in approximately $N_0 = 800 - 1200$ atoms in $|\downarrow\rangle$ with rms momentum spread $\Delta p = 0.1\hbar k$ set by choice of the two-photon Rabi frequency $\Omega = 2\pi \times 1.4$ kHz.

In Fig. 4.7 we demonstrate the quantized nature of the momentum kicks imparted by the intracavity Raman transitions. After velocity selection, a $\pi/2$ pulse is followed by a second Raman

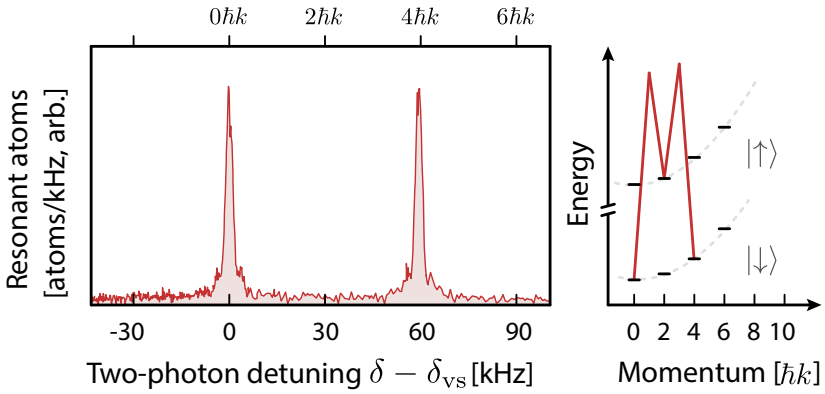

Figure 4.7: After velocity selection, a pair of Raman transitions can be used to place atoms into a superposition of $|0\hbar k, \downarrow\rangle$ and $|4\hbar k, \downarrow\rangle$. Raman spectroscopy is used to verify the discrete velocity distribution.

π pulse to place the atoms into a superposition of $|0\hbar k, \downarrow\rangle$ and $|4\hbar k, \downarrow\rangle$ in the falling frame of reference. We observe this as two distinct peaks separated in the subsequent velocity spectrum. Though not leveraged here, future interferometers might evolve in such superpositions so as to minimize systematic errors and dephasing due to environmental couplings to the spin degree of freedom.

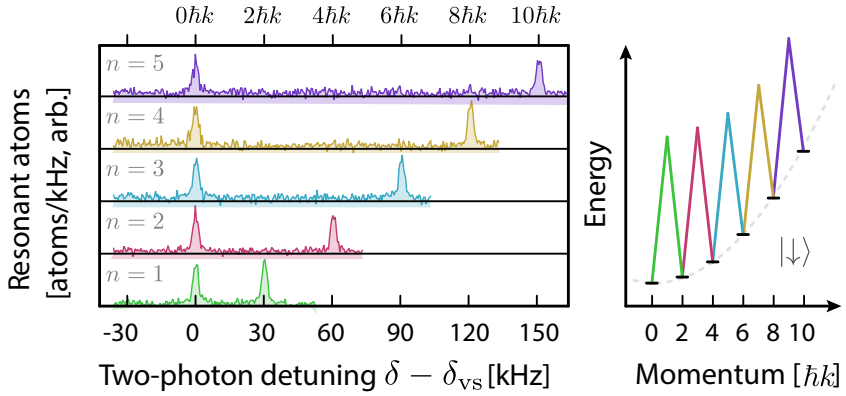

Figure 4.8: **Large momentum transfer with sequential Bragg pulses.** Bragg transitions can be driven by adding amplitude modulation to the Raman tones. Here, a Bragg $\pi/2$ pulse splits the wavepacket, and consecutive π pulses transfer additional momentum to create a superposition $|0\hbar k, \downarrow\rangle$ and $|2n\hbar k, \downarrow\rangle$ with the momentum difference as large as $10\hbar k$ shown here.

Complementary to hyperfine spin-state changing Raman transitions, we also demonstrate

intracavity Bragg transitions in this high finesse and high cooperativity cavity. The Bragg coupling connects states $|n\hbar k\rangle \leftrightarrow |(n+2)\hbar k\rangle$ with no change in the spin degree of freedom, as shown in Fig. 4.8. The Bragg transitions are driven by two laser tones derived from the same laser with difference frequency $\omega_B = \delta_{\rm vs} - b\,(t - t_{\rm vs})$. After velocity selection, the wavepacket is coherently split by a Bragg $\pi/2$ pulse, followed by successive π pulses to transfer momentum to one of the wavepacket components for a momentum difference of up to $10\,\hbar k$. Access to Bragg transitions opens the door to both large momentum transfer operations for greater sensitivity and to improved coherence times in future work.

4.3 Squeezing on momentum states.

With the ability to manipulate matter-waves in our cavity, we turn our attention to creating entanglement between atoms that includes this **external** degree of freedom. We describe the collective state of our matter-wave interferometer using a Bloch sphere with average Bloch vector $\vec{J} = \langle \hat{J}_x\hat{x} + \hat{J}_y\hat{y} + \hat{J}_z\hat{z}\rangle$ of length $J \equiv \left|\vec{J}\right| \leq N_0/2$ in a fictitious coordinate space[85]. The collective pseudospin projection operators are defined as $\hat{J}_z \equiv \frac{1}{2}\left(\hat{N}_\uparrow - \hat{N}_\downarrow\right)$ with collective population projection operators $\hat{N}_\uparrow = \sum_i^{N_0} |a\rangle_{i\,i}\langle a|$ and $\hat{N}_\downarrow = \sum_i^{N_0} |b\rangle_{i\,i}\langle b|$, and similarly for other pseudospin projections. In this work, $|a\rangle_i = |2\hbar k, \uparrow\rangle_i$ and $|b\rangle_i = |0\hbar k, \downarrow\rangle_i$ for the ith atom.

We use a Raman $\pi/2$ pulse to nominally prepare all atoms in an unentangled coherent spin state $|\psi\rangle = \Pi_i^{N_0} \frac{1}{\sqrt{2}}\left(|a\rangle_i + |b\rangle_i\right)$ described by the Bloch vector $\vec{J} = J\hat{x}$. The quantum noise that will appear in a measurement manifests in the non-zero variance of the spin projection operators $(\Delta J_z)^2 = \langle \hat{J}_z^2\rangle - \langle \hat{J}_z\rangle^2 \neq 0$, etc. and is visualized on the Bloch sphere as a quasi probability distribution of the orientation of the Bloch vector from trial to trial. It is the ratio of rms spin projection noise amplitude to the length of the Bloch vector that sets the standard quantum limit in the quantum phase estimation of the polar and azimuthal angles.

The Wineland parameter characterizes the phase enhancement of a squeezed state with phase

uncertainty $\Delta\theta$ that is certified to arise from entanglement between the atoms [17]

$$W = \left(\frac{\Delta\theta}{\Delta\theta_{\mathrm{SQL}}}\right)^2. \tag{4.1}$$

Physically, it is the reduction in the angular noise variance of the phase estimation relative to the standard quantum limit $\Delta\theta_{\mathrm{SQL}} = 1/\sqrt{N}$ one would have for a pure state with a Bloch vector length $J_c = N/2$ equal to that of the actually prepared mixed or partially decohered state absent the squeezing operation.

We prepare squeezed momentum states through two separate cavity-based interactions: quantum non-demolition (QND) measurements [38, 25, 26] and one-axis twisting (OAT) [16, 73, 74]. In both cases, quantum noise is reduced in one spin-momentum projection at the expense of increased quantum noise along the orthogonal projection.

Population readout is achieved through collective or QND measurements of the free falling atomic samples that ideally give information about the fraction of the atoms in different spin-momentum states without revealing single-particle information [38, 50][G]. The two momentum states interact differently with the optical cavity because they carry distinct spin labels. We tune a TEM_{00} cavity mode with resonance frequency ω_c to the blue of the $|\uparrow\rangle \rightarrow |e\rangle$ transition ω_a by $\delta_c = \omega_c - \omega_a$. After adiabatically eliminating the excited state $|e\rangle$ and ignoring mean-field light shifts that will be spin-echoed away, the effective Hamiltonian[74] describing the atom-cavity QND interaction can be expressed in a rotating frame at the atomic transition frequency as

$$\hat{\mathcal{H}}_{\mathrm{QND}} = \left(\delta_c + \chi_{\mathrm{QND}}\hat{N}_{\uparrow}\right)\hat{c}^{\dagger}\hat{c} \tag{4.2}$$

where the cavity field is described by creation and annihilation operators $\hat{c}^{\dagger}$ and $\hat{c}$. The QND interaction generates entanglement between the cavity field and the collective population $N_{\uparrow}$ in $|\uparrow\rangle$ so that measuring the phase of the field that emerges from the cavity allows us to determine the population $N_{\uparrow}$. Alternatively, atoms in $|\uparrow\rangle$ create a round trip phase shift of the intracavity light that causes the cavity resonance to shift by an amount $\chi_{\mathrm{QND}} = 2\pi \times 336(2)$ Hz per atom in $|\uparrow\rangle$ at a detuning $\delta_c = 2\pi \times 175$ MHz and accounting for interaction of the cavity mode with all excited state hyperfine levels.

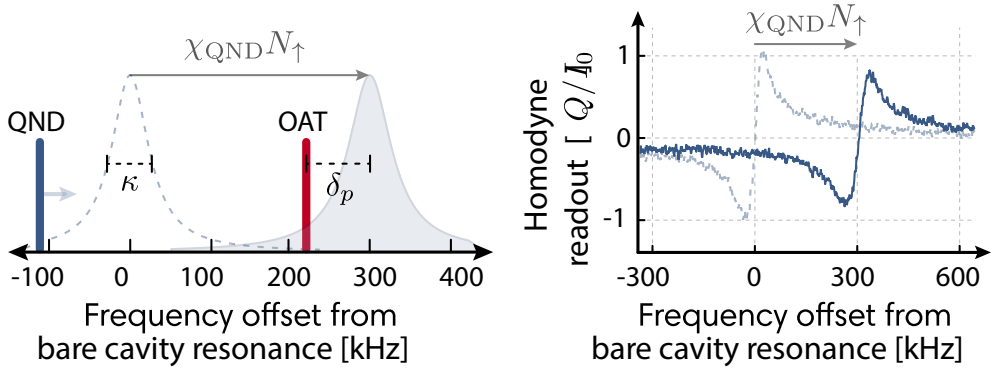

Figure 4.9: Left: frequency diagram for QND and OAT. Right: Homodyne signal when scanning atomic probe laser across cavity resonance with or without atom in the cavity

The cavity frequency shift is estimated by detecting the Q quadrature of probe light reflected from the cavity input mirror as the laser frequency is swept across resonance (Fig. 4.9). A typical measurement lasts 150μs. The population $N_\downarrow$ of atoms in the momentum state with spin label $|\downarrow\rangle$ is measured with the same technique after transferring the atoms to $|\uparrow\rangle$ using a Raman π pulse. The Raman π pulse serves the additional functions of re-overlapping the wavepackets and cancelling the average light shift of the probe.

Collective QND measurements are used in creating conditional spin squeezing. The spin-momentum projection in the population basis is measured once with the pre-measurement outcome $J_{zp} = \frac{1}{2}\left(N_\uparrow - N_\downarrow\right)|_{\mathrm{pre}}$. The same projection is then measured a second time with the final measurement outcome labeled $J_{zf} = \frac{1}{2}\left(N_\uparrow - N_\downarrow\right)|_{\mathrm{fin}}$. Each final population measurement is made after first optically pumping atoms in $|\uparrow\rangle$ to $|F = 2, m_F = 2\rangle$ to achieve lower readout noise (estimated at more than 15 dB below the projection noise level) by using the optical cycling transition to $|F = 3, m_F = 3\rangle$.

If sufficiently precise, the pre-measurement localizes the state to below the initial coherent spin state level, producing a squeezed state. It can be considered a measurement of the quantum fluctuation of the orientation of the state on a given trial, and the measurement outcome can then be used to partially subtract the quantum fluctuation from the final measurement outcome by considering the difference $J_{zd} = J_{zf} - J_{zp}$. The quantum fluctuation is common to the two

measurements, but any rotation of the state (i.e. the signal) that occurs in between the two measurements appears only in the final measurement outcome so that one can estimate the angular displacement as $\sin(\theta) \equiv J_{zd}/J_s$. The length of the Bloch vector J_s after the pre-measurement has prepared a squeezed state is measured in a separate set of experiments in which a $\pi/2$ pulse about azimuthal angle ϕ is inserted between the pre- and final measurements. The length of the Bloch vector is estimated from the fringe amplitude of J_{zf} versus ϕ as it is varied between 0 to 2π. The initial length of the Bloch vector J_c needed for estimating the spectroscopic enhancement is estimated in the same manner, but without the pre-measurement applied.

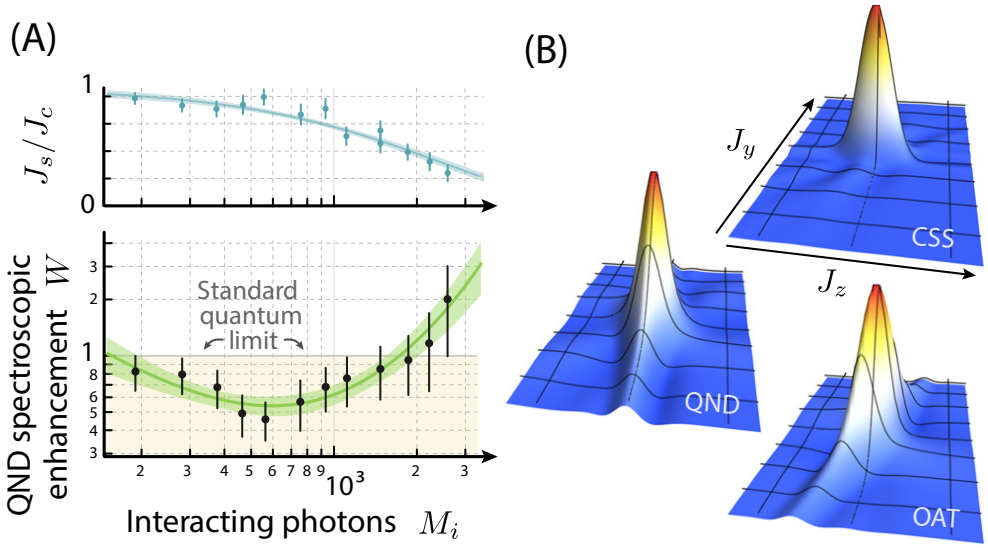

Figure 4.10: (A) Contrast lost (top) and spectroscopic enhancement W (bottom) as a function of the photon number inside the cavity. (B) State tomography of coherent spin state (CSS) and squeezed states generated by QND and OAT.

Fig. 4.10(A) shows the spectroscopic enhancement W versus the strength of the QND interaction as parameterized by M_i, the average number of incident photons that enter the cavity during each population pre-measurement window. At low M_i, the probe's vacuum noise limits the spectroscopic enhancement, while at high M_i, the spectroscopic enhancement is limited by free space scattering of the probe light that leads to a reduction in J_s and transitions to other ground states that decorrelate the pre- and final measurements. Near $M_\mathrm{i} = 600$, $N = 1170(30)$ atoms, and $\delta_c = 2\pi \times 175$ MHz, we achieve $W = 0.46(11)$ or $3.4^{+1.1}_{-0.9}$ dB of directly observed squeezing in the

momentum-spin basis.

We also realize momentum-spin entanglement via cavity-mediated interactions [73, 74, 80]. The one-axis twisting (OAT) Hamiltonian [16]

$$\hat{\mathcal{H}}_{\mathrm{OAT}} = \chi_{\mathrm{OAT}} \hat{J}_z^2 \tag{4.3}$$

is generated by applying a fixed frequency drive tone offset from the average dressed cavity resonance by $\delta_p \gtrsim \kappa/2$. Briefly, the populations in each momentum-spin state tune the cavity closer to or further from resonance with the fixed frequency drive tone, allowing more or less light into the cavity. After adiabatic elimination of the dressed cavity mode and neglecting terms that will be spin-echoed away, one finds that to first approximation, $\hat{c}^\dagger \hat{c} \propto \hat{N}_\uparrow$. As a result, the spin-dependent portion of the QND Hamiltonian is transformed after a spin-echo pulse into Eq. 4.3, a pure spin-spin Hamiltonian proportional to $\hat{N}_\uparrow^2 + \hat{N}_\downarrow^2 = 4\hat{J}_z^2$ with the cavity mode acting as a mediator of the interaction. The unitary interactions drive shearing of the atomic quantum noise distribution with a resulting squeezed state minimum noise projection oriented at a small angle α_0 from $\hat{z}$ (Fig. 4.11).

To suppress free-space scattering, it is ideal to operate at $\delta_p = \kappa/2$, however, we work at larger detunings. First, this reduces deleterious QND interactions (or equivalently, photon shot noise from the applied drive tone) that were neglected in the above description of the emergence of the unitary dynamics [86]. Secondly, this allows operation in a linearized regime even in the presence of shot-to-shot total atom number fluctuations. We empirically find an optimum detuning of $\delta_p = 2.7 \times \kappa/2$ with $\chi_{\mathrm{OAT}} \approx 2\pi \times 10$ Hz.

After the OAT interaction is applied, the state is rotated using the Raman beams to couple the momentum-spin states so that the minimum noise projection is along $\hat{z}$. The momentum-spin populations are destructively readout out as described previously with measurement outcome labeled J_{zf}. The Bloch vector lengths J_s (J_c) with (without) OAT squeezing are measured in the same manner as was done for the QND measurements by measuring the fringe amplitude of J_{zf} versus the azimuthal phase of a $\pi/2$ rotation prior to the final readout. We achieve a directly observed spectroscopic enhancement from OAT of $W = 0.56(8)$ or $2.5^{+0.6}_{-0.6}$ dB. The optimal

configuration was realized with $M_{\mathrm{i}} \approx 700$ photons, $\delta_c = 2\pi \times 350$ MHz, and $N = 730(10)$ atoms.

4.4 Wineland criterion

Here in this section, we will justified the definition Eq. 4.1 presented before. The Wineland criterion is often presented in the following form [26]

$$W = \frac{(\Delta J_z)^2 C_i}{\Delta J_{z,SQL}^2 C_f^2}, \tag{4.4}$$

where the contrasts are related to Bloch vector lengths here by $C_i \equiv 2J_C/N_0$ and $C_f \equiv 2J_s/N_0$ for total atom number N_0. By rearranging terms, it can also be expressed in a more physically meaningful form as the ratio $W = (\Delta\theta/\Delta\theta_{SQL})^2$ between the observed angular resolution $\Delta\theta = \frac{\Delta J_z}{J_s}$ with entanglement and the standard quantum limit $\Delta\theta_{SQL} = 1/\sqrt{N} \equiv 1/\sqrt{2J_C}$ for a pure state with the same Bloch vector length J_C as that of the actual mixed state when entanglement is not created.

We now establish the connection between the spin operators and actual experimental measurements. We define the cavity frequency shifts induced by a single atom in $|F = 2, m_F = 2\rangle$, $|F = 2, m_F = 0\rangle$ and $|F = 1, m_F = 0\rangle$ as $\chi_2, \chi_0 \equiv \chi_{\mathrm{QND}}$ and $\chi_\downarrow$ respectively.

For OAT squeezing, we estimate the angular resolution $\Delta\theta$ after the squeezing generation or the full squeezed interferometer sequence as follows. To measure the final spin projection J_{zf}, we optically pump the atoms in $|\uparrow\rangle$ to $|F = 2, m_F = 2\rangle$, measure the cavity frequency shift with outcome labeled ω_{1f}, blow away atoms in $|F = 2\rangle$, apply a Raman π pulse, optically pump the atoms in $|\uparrow\rangle$ to $|F = 2, m_F = 2\rangle$, and measure a second cavity frequency shift with outcome labeled ω_{2f}. We estimate the final spin projection J_{zf} from the difference between the two cavity frequency shifts $J_{zf} = \frac{\omega_{1f} - \omega_{2f}}{2\chi_2} - \frac{\epsilon}{\chi_2}\omega_{2f}$, where $\epsilon = \frac{\chi_\downarrow/2}{\chi_2}$. To convert the spin projection J_{zf} into an estimate of the Bloch vector polar angle θ_f, we measure the length of the Bloch vector J_s by scanning the azimuthal phase ϕ of the readout $\pi/2$ pulse. In the case of the squeezed interferometer, this is the final $\pi/2$ pulse of the interferometer and just prior to the measurement J_{zf}. In the case of OAT squeezed state generation, this is an added $\pi/2$ pulse after the squeezing and just prior to the measurement J_{zf}. We

fit the resulting differential cavity frequency shifts $(\omega_{1f} - \omega_{2f})\,|_\phi$ to the function $y_0 + A_f \sin(\phi - \phi_0)$. The Bloch vector length is then estimated by $J_s = \frac{A_f}{2\chi_2 - \chi_\downarrow}$. The Bloch vector polar angle θ_f from the final measurement is thus estimated by $\theta_f = \frac{J_{zf}}{J_s} = \frac{\omega_{1f}-\omega_{2f}}{A_f} - \epsilon\frac{\omega_{1f}+\omega_{2f}}{A_f} + 2\epsilon^2\frac{\omega_{2f}}{A_f}$. The angular resolution $\Delta\theta$ is approximated as $\Delta\theta = \Delta\theta_f \approx \frac{\Delta(\omega_{1f}-\omega_{2f})}{A_f}$, where we note the scale factors χ_2 etc. are canceled at the order of ϵ^0. With a typical $|\epsilon| < 1/50$ and the fractional total number fluctuation $\Delta\left(\frac{\omega_{1f}+\omega_{2f}}{A_f}\right)$ being less than 0.03, the corrections of order ϵ^1 would need to be included for squeezing 30 dB below the SQL.

For the QND measurements, we perform pre-measurements to localize the quantum state and use the final measurements to verify the squeezing generated by the pre-measurements as described before. The phase resolution is defined as the phase fluctuation between the pre- and final measurements $\Delta\theta = \Delta(\theta_p - \theta_f)$. The Bloch vector polar angle of the final measurements θ_f is estimated as in the OAT measurement with the atomic population optically pumped to $|F = 2, m_F = 2\rangle$. For the pre-measurements, we measure pairs of cavity frequency shifts ω_{1p} and ω_{2p} separated by π pulses but without the optical pumping so the atomic population is in $|\uparrow\rangle$ during the cavity frequency shift measurements. The spin projection J_{zp} in the pre-measurements is estimated from the differential frequency shift $J_{zp} = \frac{\omega_{1p}-\omega_{2p}}{2(\chi_0 - \chi_\downarrow)}$. The length of the Bloch vector J_s just after the pre-measurement is measured by adding a $\pi/2$ pulse just after the pre-measurement and scanning its azimuthal phase ϕ, after which we perform a single cavity frequency shift measurement with outcome labeled $\omega_{1f}|_\phi$. We then fit the resulting fringe to the function $y_0 + A_p \sin(\phi - \phi_0)$ and estimate the Bloch vector length $J_s = \frac{A_p}{\chi_0 - \chi_\downarrow}$. The Bloch vector polar angle θ_p is evaluated $\theta_p = \frac{J_{zp}}{J_p} = \frac{\omega_{1p}-\omega_{2p}}{2A_p}$. As before, the angular phase resolution is sufficiently approximated by keeping only to the order of ϵ^0 as $\Delta\theta = \Delta(\theta_p - \theta_f) \approx \Delta\left(\frac{\omega_{1p}-\omega_{2p}}{2A_p} - \frac{\omega_{1f}-\omega_{2f}}{A_f}\right)$ with no dependence on scale factors χ_2, χ_0 or $\chi_\downarrow$.

For estimating the standard quantum limit $\Delta\theta_{SQL}$, we measure the length of the Bloch vector $J_c = J_s|_{M_i=0} = \frac{A_p|_{M_i=0}}{\chi_0 - \chi_\downarrow}$ using the same sequence for measuring J_s in the QND pre-measurements described just above but setting the photon number M_i to zero during the pre-measurements or squeezing for QND measurement or OAT respectively. To estimate the standard quantum

limit $\Delta\theta_{SQL} = 1/\sqrt{N} = 1/\sqrt{2J_c}$ we therefore need to know accurate values of χ_0 and $\chi_\downarrow$. To sufficient approximation $\chi_0 = g^2\left(\frac{B_3}{\delta_c} + \frac{B_2}{\delta_c+\delta_2} + \frac{B_1}{\delta_c+\delta_1}\right)$ with atom-cavity coupling g discussed below, hyperfine splittings $\delta_2 = 2\pi \times 266.7$ MHz, $\delta_1 = 2\pi \times 423.6$ MHz and branching ratios $B_3 = \frac{6}{15}, B_2 = \frac{3}{12}, B_1 = \frac{1}{60}$ of the excited states $|F' = 3, 2, 1, m_F = 1\rangle$ to the ground state $|\uparrow\rangle$ transition that interact with the probe light. To sufficient approximation $\chi_\downarrow = g^2\left(\frac{B_{2,\downarrow}}{\delta_c+\delta_2-\omega_{\rm HF}} + \frac{B_{1,\downarrow}}{\delta_c+\delta_1-\omega_{\rm HF}}\right)$ with branching ratios $B_{2,\downarrow} = \frac{3}{12}, B_{1,\downarrow} = \frac{5}{12}$ of the $|F' = 2, 1, m_F = 1\rangle$ to the ground state $|\downarrow\rangle$ transition. Though not used in the calculation, the cavity frequency shift from a single atom in $|F = 2, m_F = 2\rangle$ is approximated by $\chi_2 = \frac{g^2}{\delta_c}$ for the cycling transition between the excited state $|F = 3, m_F = 3\rangle$ and ground state $|F = 2, m_F = 2\rangle$.

The maximum single-atom vacuum Rabi splitting $2g_0 = 2\sqrt{\frac{2D^2\omega_c}{\pi L w_0^2 \epsilon_0 \hbar}} = 2\times 2\pi \times 0.4853(5)$ MHz [34] with fractional uncertainty dominated by the fractional uncertainty (1.1×10^{-3}) on the dipole matrix element D for the $|F = 2, m_F = 2\rangle$ to $|F = 3, m_F = 3\rangle$ transition, and ϵ_0 the vacuum permeability. The cavity length L and mode waist w_0 are determined very precisely by measuring the free spectral range and transverse mode frequency splitting. Since the atoms traverse many standing waves of the cavity during the measurement windows, we can coarse grain over the standing waves to arrive at a time-averaged spatially dependent coupling $g_t(r, z) = \frac{g_0}{\sqrt{2}} \frac{e^{-r^2/w_0^2}}{\sqrt{1+\left(\frac{z}{Z_r}\right)^2}}$, where $Z_r = 2.1$ cm is the Rayleigh range of the cavity [50]. The effective single atom-cavity coupling frequency is given by the ensemble averaged moments of the spatially dependent $g_t(r, z)$ as $g = \sqrt{\frac{\langle g_t(r,z)^4 | g_t(r,z)^4 \rangle}{\langle g_t(r,z)^2 | g_t(r,z)^2 \rangle}} = \frac{g_0}{\sqrt{2}}(1 - f_{cor}) = 2\pi \times 0.341(2)$ MHz [34]. The final fractional uncertainty (6×10^{-3}) on g is dominated by the uncertainty on the correction factor $f_{cor} \approx \frac{z_0^2+\sigma_z^2}{2Z_r^2} + \frac{r_{rms}^2}{w_0^2}$, where $z_0 = 1\,(2)$ mm is the axial position of the cloud relative to the cavity center, $\sigma_z = 0.5(3)$ mm is the RMS axial spread of the cloud, and r_{rms} is the RMS cloud radius of the atoms. The fractional uncertainty on g contributed from z_0, σ_z and r_{rms} are 5×10^{-3}, 4×10^{-3} and 2×10^{-3} respectively.

The uncertainties on the cavity detuning $\delta_c = 175(2)$ MHz or $350(2)$ MHz lead to fractional uncertainties ≤ 0.01 on $\left(\chi_{\rm QND} - \chi_\downarrow\right)$. Because the atoms move along the cavity axis, the probe light is Doppler shifted by of order $\delta_{\rm vs}/2$; however, here $\delta_c \gg \delta_{\rm vs}$ so that there is only a negligible

fractional correction to χ_{QND} of order $(\delta_{\mathrm{vs}}/2\delta_c)^2 \lesssim 10^{-6}$. The effect of spread in momentum states is even more negligible.

Combining uncertainties from g and δ_c, the fractional uncertainty on $\left(\chi_{\mathrm{QND}} - \chi_{\downarrow}\right)$ is $\leq 1.4 \times 10^{-2}$. This uncertainty combined with the fractional uncertainty on the fitted fringe amplitude A_p of 9×10^{-3} yields a total fractional uncertainty on the standard quantum limit variance $\left(\Delta\theta_{\mathrm{SQL}}\right)^2$ of 1.7×10^{-2}. To estimate the angular resolutions $(\Delta\theta)^2$, we typically use 100 to 200 experimental trials, which leads to a typical statistical fractional uncertainty on $(\Delta\theta)^2$ of 0.1 to 0.2. The final reported uncertainties on the Wineland parameters are thus dominated by the statistical uncertainties on the phase resolution $(\Delta\theta)^2$.

Without the QND pre-measurements or one-axis twisting, the mixed state actually performs worse than the standard quantum limit, conceptually due to the spin noise from the dephased or decohered fraction of the atoms that contribute noise but no signal. This is why the observed improvement in the interferometer sensitivity is larger than the Wineland parameter; however, the Wineland parameter captures what fraction of the improvement can be certified to arise due to entanglement between the atoms and not due to just cancellation of spin noise alone.

4.5 Entangled matter-wave interferometry.

We now turn to injecting the prepared entangled states into a matter-wave interferometer. We use a slightly modified Mach-Zehnder Raman interferometer with ($\pi/2$ - π - $\pi/2$) pulse sequence to coherently separate, undo the separation, and interfere the atomic wavepackets. In analogy to an optical Mach-Zehnder interferometer, the $\pi/2$ pulses play the role of 50/50 beam splitters at the entrance and exit of the interferometer and the π pulse plays the role of the mirrors that redirect the beams from the input beam splitter to the output beam splitter.

After preparing a squeezed state with OAT, a Raman beam splitter rotation orients the squeezing along $\hat{y}$. The spin projection J_y will change if a small signal phase ϕ is applied. The orienting of the squeezing is accomplished via a $(\pi/2 + \alpha_0)$ pulse aligned to the atomic Bloch vector along $\hat{x}$. A relative phase accumulates between the wavepackets during a free evolution time T_{evol},

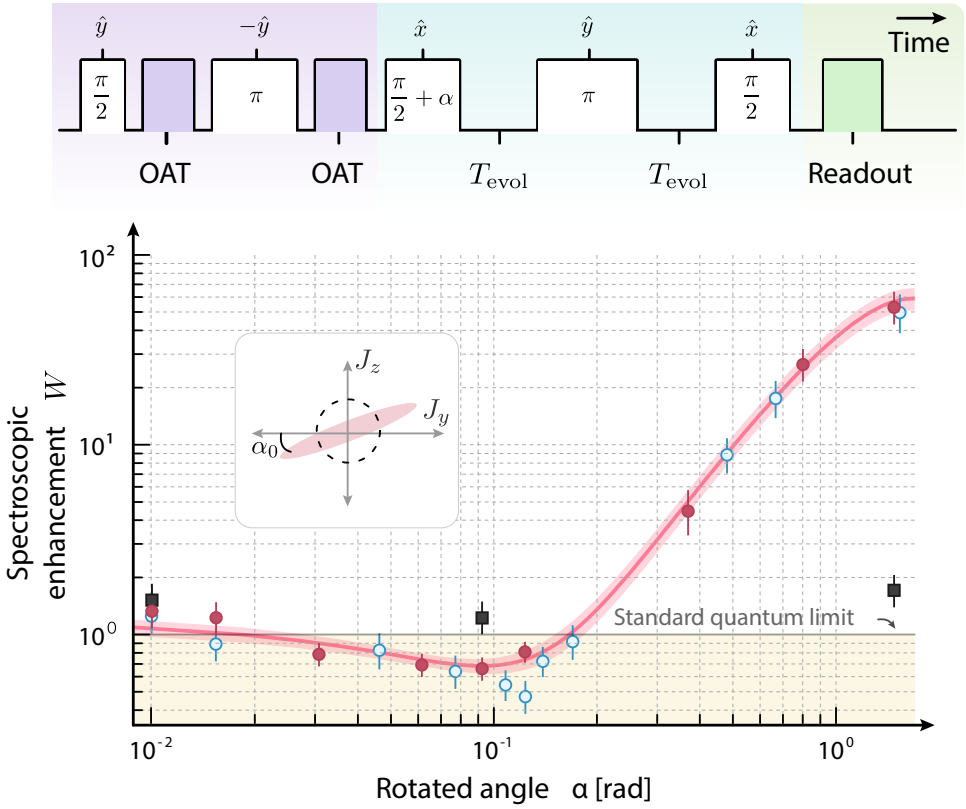

Figure 4.11: **Entangled matter-wave interferometer.** Top: The squeezed interferometer sequence, including entanglement generation (purple), the interferometer (blue), and state readout (green). Each Raman transition (white rectangle) is labeled with magnitude (within) and axis of rotation (above). Bottom: The spectroscopic enhancement W is compared for three configurations: a Mach-Zehnder interferometer with OAT (red circles, sequence above), an unentangled interferometer without OAT (black squares), and OAT-squeezed states without the interferometer (blue circles). The duration of a $\pi/2+\alpha$ rotation is scanned to minimize the projected spin noise at α_0. An ellipse is fit with 68% confidence bands to the OAT-squeezed interferometer data, giving a minimum variance of $W = 0.68(8)$ or $1.7^{+0.5}_{-0.5}$ dB. The interferometer here had $T_{evol} = 0.112$ ms.

a Raman π "mirror" pulse is applied, followed by another free evolution time T_{evol}. Finally, a readout $\pi/2$ pulse transfers the signal ϕ and the squeezing into a displacement in the momentum-spin population basis $\hat{z}$ with a measurement outcome J_{zf}. The Bloch vector lengths J_s and J_c are measured in separate experiments with and without OAT applied by scanning the azimuthal phase of the final $\pi/2$ pulse of the interferometer and measuring the fringe amplitude as before (see Fig. 4.12.

We achieve a directly observed spectroscopic enhancement as measured by the Wineland

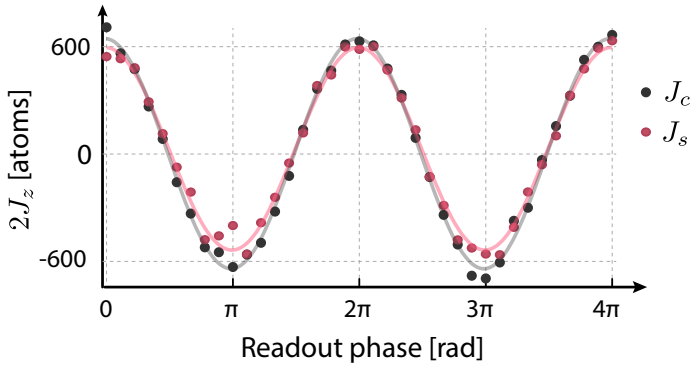

Figure 4.12: Interferometer contrast fringes with $T_{\text{evol}} = 0.112$ ms shown for no squeezing J_c (black) and with squeezing J_s (red).

parameter of $1.7^{+0.5}_{-0.5}$ dB beyond the standard quantum limit with $N = 660(15)$ atoms as shown in Fig. 4.11. We also note that the actual phase variance of the interferometer is enhanced by $3.4^{+0.9}_{-1.2}$ dB compared to with no one axis twisting, consistent with expectations from J_c.

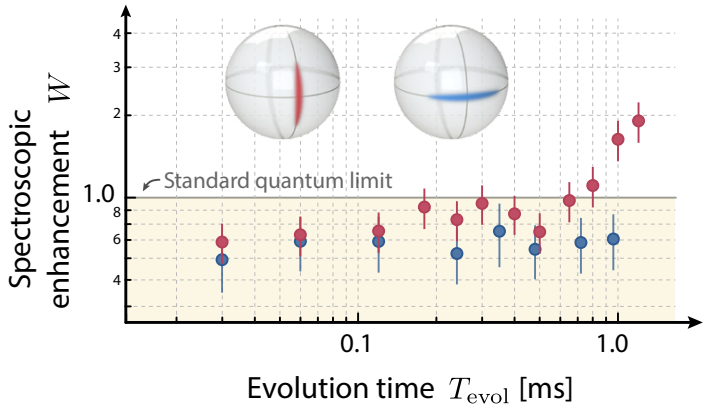

Figure 4.13: Phase sensitivity is maintained below the SQL for the squeezed interferometer (red circles, left Bloch sphere) up to $T_{evol} = 0.7$ ms. By contrast, if the squeezed spin projection is oriented along the population basis (blue circles, right Bloch sphere), spectroscopic enhancement was seen to persist beyond $T_{evol} = 1$ ms because this orientation is insensitive to phases accrued during the evolution time.

Phase sensitivity beyond the SQL was limited to evolution times $T_{\text{evol}} < 0.7$ ms (Fig. 4.13). Evidence from purely microwave interferometers with no momentum states involved suggests this loss of observable squeezing was primarily due to magnetic field fluctuations in the lab that lead

to added fluctuations in the azimuthal phase accrued during the interferometer evolution times. The matter-wave interferometer is sensitive to vibration noise, but the measured accelerations are not sufficient to explain the loss of directly observed entanglement. Single-particle decoherence is also inadequate as an explanation because J_c decreased by less than 5% over these evolution times. We also observe that if the squeezed spin projection is left in the population basis J_z during the interferometer, then the squeezing persists for several milliseconds. From this, we conclude that the entangled state persists for longer than we can directly confirm because the interferometer is detecting an undesired magnetic field signal that masks the quantum noise reduction as T_{evol} increases.

4.6 Vibration noise

Mechanical vibrations of the cavity mirrors are equivalent to a fluctuating phase reference for the atoms. We measure the vibration noise with two different approach. First, we form an optical Mach-Zehnder interferomter (setup is shown in Fig. 4.14) with the science cavity mirror and an extra fixed mirror on the optical table. The measured vibration noise is dominated by the vertical vibration of the optical table.

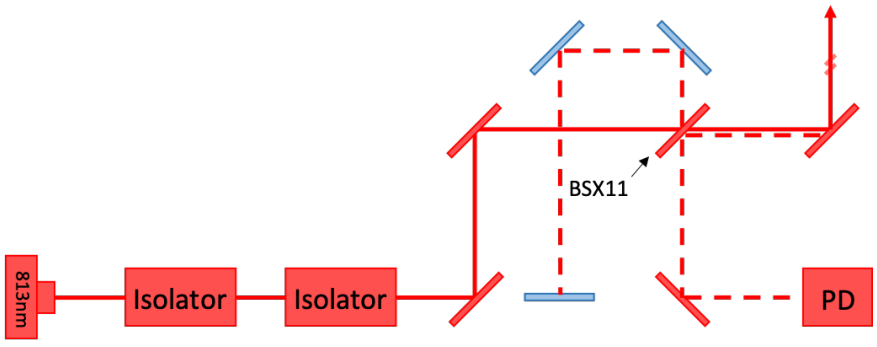

Figure 4.14: Measuring vibration noise with an optical Mach-Zehnder interferometer.

Secondly, a commercial vibrometer (Herzan VA-2) was used to measure the noise at a location on the optical table close to the portion that supports the vacuum chamber. The measurement results (power spectral density of vibration noise) are shown in Fig 4.15. In the limit of zero-

duration pulses, the transfer function for a matter-wave Mach-Zehnder interferometer $|T(\omega)|^2 = \frac{64k^2}{\omega^4}\sin\left(\frac{\omega T_{evo}}{2}\right)^4$ converts accelerations to an integrated phase noise $\phi^2 = \int_0^\infty |T(\omega)|^2 S_a(\omega)\, d\omega$. For a sequence with T_{evo} =0.3 ms, we estimate the phase noise caused by vibrations is 20 dB lower than the phase resolution set by the SQL of 1000 atoms.

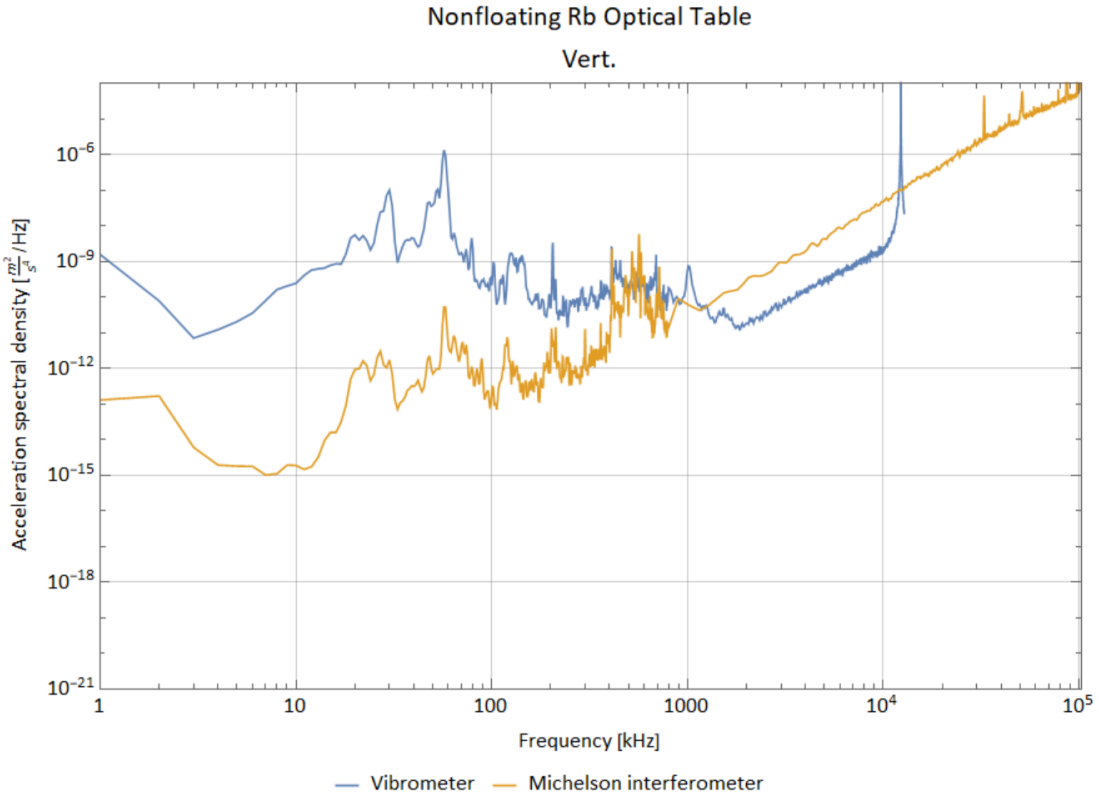

Figure 4.15: Power spectral density of the vibration noise as measured by the optical Mach-Zehnder interferomter and a commercial vibrometer.

4.7 Error budget for standard quantum limit

We estimated the observed squeezing by comparing the measured phase uncertainty $\Delta\theta$ to the calculated standard quantum limit $\Delta\theta_{SQL}$. The SQL is estimated based on the atom number measurements. The atom number is measured by the cavity frequency shift divided by the single atom frequency shift χ_{QND}, which relies on the details of the atom-cavity coupling.

The maximal atom-cavity coupling g_0 is calculated based on the atomic transition dipole

matrix element, cavity parameters and fundamental constants. The cavity parameters are estimated based on frequency measurements. Tough trapped inside the cavity, the finite radial temperature and finite axial extend could also affect the atom-cavity coupling. To account for different sources of error, different parameters and the resulting fractional error in terms of estimating the SQL are summarized in Table 4.1.

Parameters	Value	Error	Unit	Fractional uncertainty on $\Delta\theta_{SQL}$
Dipole matrix element for cycling transition	2.534×10^{-29}	0.003×10^{-29}	C*m	0.223 %
Free spectral range	6.7879	0.0001	GHz	0.002%
Mode splitting between TEM00 and TEM10 mode	2.1145	0.0003	GHz	0.016%
Atomic radial temperature	1.4	0.5	μK	0.307%
Radial trap depth of donut mode	58	5	μK	0.069%
Initial position of lattice from center	0	0.002	m	0.903%
Detuning of probe beam from atomic transition	175	1	MHz	0.497%
Cavity frequency shift with all atoms in $\|\uparrow\rangle$	238	3	kHz	1.266 %

Table 4.1: Table for different sources of error.

4.8 Conclusion and outlook

In the future, the magnetic field noise can be reduced and looking further ahead, the combination of Raman and Bragg techniques demonstrated here would enable the most delicate portion of the interferometer to be operated fully with the two portions of the superposition possessing the same spin label. To further improve interferometer sensitivity, the entanglement can be combined with large momentum transfer sequences, one could inject the squeezed state into a lattice interferometer to hold the atoms longer [82], or prepare the entanglement in the cavity and allow the atoms to undergo free fall and subsequent fluorescence measurement readout [77].

The amount of momentum squeezing could be improved with larger collective cooperativity NC. The need for velocity selection limits our final number of atoms, so higher atom density in momentum space through improved axial cooling or the use of a Bose-Einstein condensate could lead to significant improvements [87, 88, 28, 89]. It will also be possible to perform the entanglement generation utilizing optical cycling transitions in rubidium, strontium, and ytterbium [38, 90, 26, 50, 76] for which the fundamental scaling of the achievable Wineland parameter would improve to $W \propto 1/NC$ from the current scaling $W \propto 1/\sqrt{NC}$.

This proof-of-principle light-pulse matter-wave interferometer paves the way for utilizing cavity-generated entanglement as a quantum resource, enabling the next generation of interferometers with higher precision, enhanced measurement bandwidth, higher accuracy, and smaller size. Such devices will advance the frontiers of both practical applications and discoveries in fundamental science, from particles and fields to gravitational wave detection [5, 22, 58, 20, 21, 60, 61, 63, 40, 64, 19, 56, 4, 81, 87, 88, 89, 82, 59, 91], and build a bridge to a future where cavity-QED-based quantum many-body simulations will move beyond mean-field physics to probe and manipulate quantum fluctuations in large ensembles of atoms [92, 93, 94, 95, 96].

Chapter 5

Cavity mediated momentum-exchange interaction

Large ensembles of laser-cooled atoms interacting via infinite-range photon-mediated interactions are powerful platforms for quantum simulation and sensing. Here we realize for the first time momentum-exchange interactions in which pairs of atoms exchange their momentum states via collective emission and absorption of photons from a common cavity mode, a process equivalent to a spin-exchange or XX collective Heisenberg interaction. The momentum-exchange interaction leads to an observed all-to-all Ising-like interaction in a matter-wave interferometer, which is useful for entanglement generation. A many-body energy gap also emerges, effectively binding interferometer matter-wave packets together to suppress Doppler dephasing with analogies to Mössbauer spectroscopy. The tunable momentum-exchange interaction provides a new capability for quantum interaction-enhanced matter-wave interferometry and for realizing exotic behaviors including simulations of superconductors and dynamical gauge fields.

5.1 Background

Many-body quantum states of laser-cooled atoms can be exquisitely controlled, making them powerful platforms for quantum simulation, metrology, and computing. In particular, quantum sensing and metrology rely on understanding how to realize new forms of interactions between the atoms to achieve the next generation of ultra-precise quantum sensors and to emulate both complex quantum phases of matter as well as non-equilibrium systems that are difficult to access in real materials.

Optical cavities can be used to enhance the interaction of atoms with light in quantum many-body systems in which either the atomic internal [33, 97, 98, 99, 100], motional [101, 102, 103, 104, 105], or both [106, 11] degrees of freedom are coupled between different atoms. In addition, the strong light-atom interaction has enabled the largest directly observed entanglement generation to date in any system [107, 25], with applications in quantum sensing with matter-wave interferometers [11] and clocks [76, 108, 78, 25].

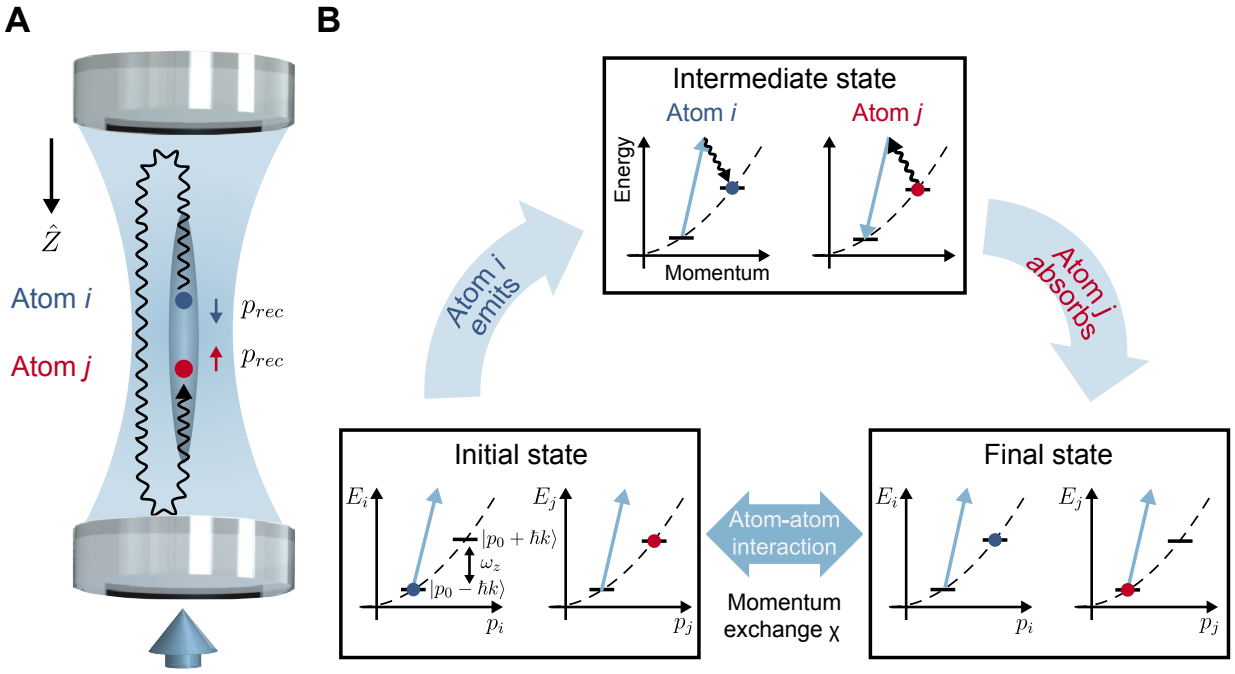

Figure 5.1: Experimental setup for observing momentum-exchange interaction. (A) A momentum-exchange interaction is realized between atoms in different momentum states $(p_0 \pm \hbar k)\,\hat{Z}$ by exchange of photons via a standing-wave optical cavity, illustrated for two particular atoms in red and blue. The dressing laser (light blue arrow) is injected into the cavity. (B) The energy versus momentum diagrams illustrate the steps of the momentum-exchange between the example red and blue atoms. Eliminating the intermediate states leads to an effective momentum-exchange Hamiltonian involving only the atoms.

Here, we realize a unitary cavity-mediated momentum-exchange interaction in a many-body system in which pairs of atoms exchange their momentum states, as shown in Fig. 5.1. The momentum exchange interaction arises from an atomic density grating creating sideband tones on an applied dressing laser, similar to as occurs in cavity opto-mechanical systems [109, 110,

111, 112, 113, 114, 115], as illustrated in Fig. 5.2. The momentum-exchange can be modeled as an all-to-all pseudo-spin-exchange interaction, analogous to that observed for internal spin states [98, 97, 116, 99, 100]. While previous theoretical proposals have considered the generation of such momentum-exchange in a ring cavity, as well as extensions to two-mode squeezing involving additional spin degrees of freedom [117, 118], here we experimentally realize a momentum-exchange interaction in a standing wave cavity by exploiting the Doppler shift of the falling atoms.

The observed momentum-exchange interaction allows for the realization of the collective XX-Heisenberg model, an iconic model in quantum magnetism and superconductivity [119, 120, 121], now generated in a momentum-only basis of states with no internal atomic degrees of freedom involved, as compared to previous [98, 97, 116, 99] and contemporaneous work [122]. The exchange interaction manifests firstly as a magnetization-dependent global spin precession of the collective pseudo-spin Bloch vector, referred to as one-axis twisting (OAT). Secondly, it generates a many-body energy gap that realizes a collective recoil mechanism that suppresses dephasing due to Doppler broadening (i.e. single-particle dispersion), analogous to, but distinct from Mössbauer and Lamb-Dicke spectroscopy, which have been keys to realizing state-of-the-art quantum metrology and searches for new physics [123, 124].

5.2 Experiment setup

In the experiment, ^{87}Rb atoms are laser-cooled inside a two-mirror standing wave cavity that is vertically-oriented along $\hat{Z}$, see Fig. 5.1 and [11, 125]. The atoms are allowed to fall along the cavity axis, guided by a blue detuned intracavity optical dipole trap. A pair of laser beams with different frequencies are injected non-resonantly into the cavity in order to drive velocity-sensitive two-photon Raman transitions between ground hyperfine states (for state preparation and readout) or Bragg transitions that only change momentum states (for manipulating the superposition of momentum states.)

The atoms are prepared in the ground hyperfine state $|F = 2, m_F = 2\rangle$ with momentum along the cavity axis $p_0 - \hbar k$ and rms momentum spread $\sigma_p < 0.1\hbar k$ after Raman velocity selection from

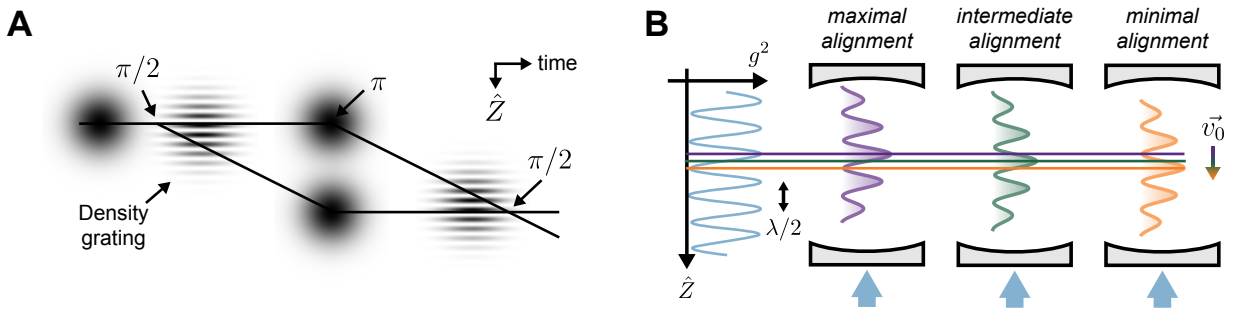

Figure 5.2: **Modulation sidebands created by atomic density grating** (A) Space-time diagram of the matter-wave interferometer. Bragg pulses are applied to manipulate atoms in superpositions of momentum states, causing the wave packets to separate in time with subsequent pulses reoverlapping the wave packets. When the wave packets overlap with each other, their interference forms a density grating along $\hat{Z}$. (B) As the atomic density grating moves, its spatial overlap with the standing-wave cavity mode (light blue on the left) varies, with three snapshots in time (purple, green and orange) shown on the right.

the laser-cooled cloud [11], where $\hbar$ is the reduced Planck constant, the wavenumber is $k = 2\pi/\lambda$, and the wavelength is $\lambda = 780$ nm. As shown in Fig. 5.2A, the Bragg lasers are then applied to place the atoms in a superposition of two wave packets with momenta centered on $p_0 \pm \hbar k$ with average momentum p_0 and separated by two photon recoil momenta $2\hbar k$. The average momentum p_0 continues to increase due to gravity, but we compensate this by appropriate chirping of applied laser frequencies [11, 12], such that one can consider p_0 to be constant in the following discussion for simplicity. Inserting additional Bragg pulses, we can realize a matter-wave interferometer, in which the atomic wave packets move apart and then reoverlap at later time. Just after the wave packet splitting and just before reoverlapping, the two portions of the wave packets interfere, leading to a spatially varying atomic density grating with periodicity $\lambda/2$ matching the periodicity of the standing-wave cavity mode.

As shown in Fig. 5.3, a cavity mode's frequency is detuned by about 500 MHz to the blue of the D2 cycling transition $|F = 2, m_F = 2\rangle \rightarrow |F' = 3, m_{F'} = 3\rangle$. A dressing laser with photon flux $|\alpha_d|^2$ (in unit of photons per second) drives the cavity at frequency ω_d that is typically within a MHz of the cavity resonance frequency. The input coupling of the cavity κ_1 is determined by the transmission of the input mirror. The detuning of the dressing laser from the atomic transition,

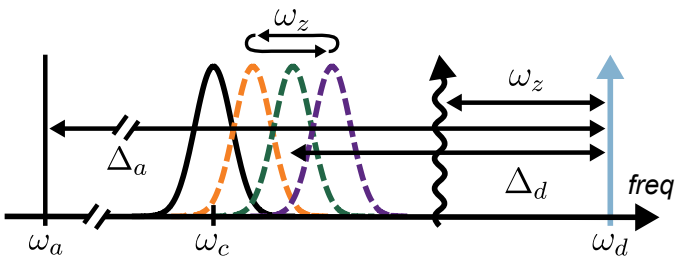

Figure 5.3: Frequency diagram of the optical atomic transition frequency ω_a (black solid line), bare cavity frequency ω_c with no atoms in the cavity (black solid Lorentzian), and the atom-dressed cavity resonance frequency (dashed purple, green, orange Lorentzians) for the corresponding snapshots in time from (C). The average dressing laser detuning Δ_d is shown. The cavity is frequency modulated at ω_z, leading to sidebands on the dressing laser at $\pm\omega_z$ (lower sideband shownas wiggly black line) that with the dressing laser couple the momentum states $p_0 \pm \hbar k$ to realize the momentum-exchange.

Δ_a is large compared to all other relevant frequency scales including the excited state decay rate $\Gamma = 2\pi \times 6$ MHz and the cavity power decay rate $\kappa = 2\pi \times 56(3)$ kHz. In this far-detuned limit, an atom at position Z shifts the cavity resonance by $\frac{g_0^2}{\Delta_a}\cos^2(kZ)$, where $g_0 = 2\pi \times 0.48$ MHz is the maximal Jaynes-Cummings atom-cavity coupling at a cavity anti-node [38].

5.3 Modulation sidebands created by atomic density grating.

As the atomic density grating moves along the cavity axis at velocity $v_0 = p_0/m$, with m the mass of ^{87}Rb, the density grating goes from being aligned to misaligned with the cavity standing wave shown in Fig. 5.2 from left to right. This leads to a modulation of the cavity resonance frequency at the two-photon Doppler frequency $\omega_z = 2kv_0$ as shown in Fig. 5.3. The modulation of the cavity resonance frequency leads to optical modulation sidebands on the dressing laser inside the cavity at frequencies $\omega_d \pm \omega_z$, with the closer to resonance sideband shown in Fig. 5.3 (black wiggly line), in a direct analogy to cavity opto-mechanical systems [115, 114, 113]. The modulation sidebands can also be understood as the Doppler-shifted reflection of the dressing laser from the moving matter-wave grating.

We directly observe that a modulation sideband combined with the dressing laser form a Bragg coupling that drives collective population transfer from $p_0 - \hbar k$ to $p_0 + \hbar k$ as shown by

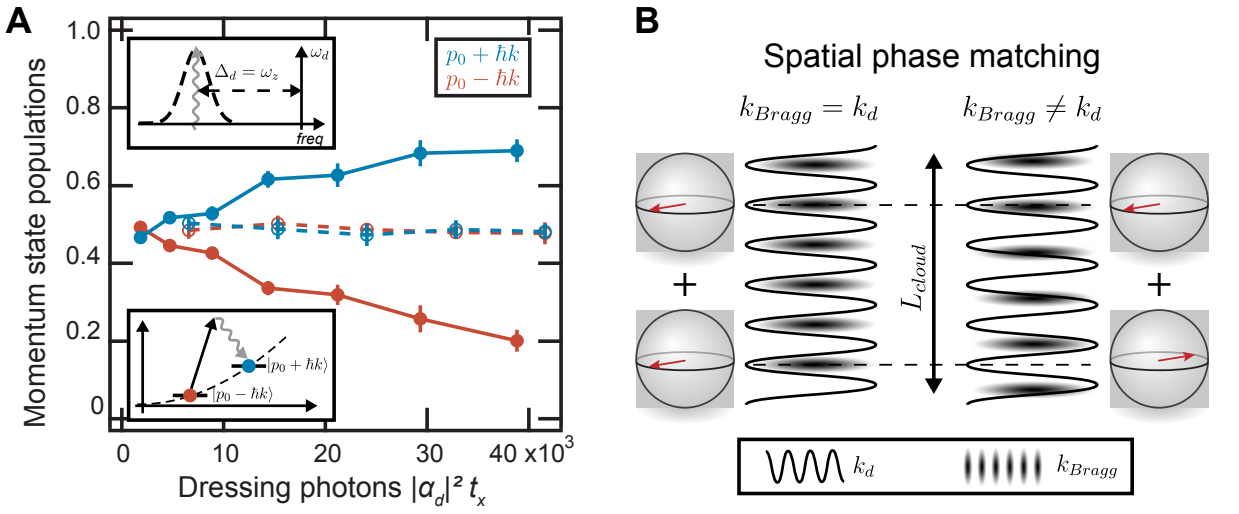

Figure 5.4: **Matter-wave superradiance.** (A) When a modulation sideband generated by the moving atomic density grating is tuned to resonance with the cavity (top inset), the light escapes the cavity and population is collectively or superradiantly transferred (bottom inset) between the two momentum states at $p_0 \pm \hbar k$ (solid points and lines.) (B) The system is well phase matched when the wave numbers of the Bragg laser (that generates the density grating) and the dressing laser (that drives the momentum-exchange interaction) closely match each other (on the left). A difference in wave number ($k_{Bragg} \neq k_d$) will lead to a spatially varying phase that eliminates the superradiance (on the right).

the solid points and lines in Fig. 5.4(A). This occurs when we tune a modulation sideband to be nominally on resonance with the dressed cavity by setting the dressing laser detuning from the average cavity resonance frequency (see Fig. 5.3 to $\Delta_d = \omega_z$. In this regime, the sideband light can escape from the cavity before being re-absorbed by the atoms, such that the collective population transfer can also be understood as a superradiant decay between momentum states [109, 111, 112]. To confirm the collective nature of the decay, in a separate experiment, we prepare the initial superposition of states using an initial Bragg $\pi/2$-pulse 85 GHz detuned from the dressing laser. The difference in wave numbers of the dressing laser k_d and the Bragg laser k_{Bragg} causes a slip in the spatial alignment of the cavity standing wave and the atomic density grating by a phase $2\,|k_d - k_{Bragg}|\,L_{cloud} = 3.5$ radians across the axial extent $L_{cloud} = 1$ mm of the atomic cloud (Fig. 5.4B). In this case, we observe no superradiant transfer of population in Fig. 5.4(A) (open circles and dashed lines).

We now realize the momentum-exchange interaction by tuning the dressing laser so that the modulation sidebands are far from resonance with the cavity, i.e. $|\Delta_d \pm \omega_z| \gg \kappa/2$. In this limit, photons emitted at the sideband frequencies are more likely to be re-absorbed by the atoms than to escape from the cavity. This process of emitting and absorbing sideband photons leads to a momentum-exchange as illustrated in Fig. 5.1A and B.

5.4 Different interpretations of modulation sidebands

In the former section, we have presented the creation of the frequency sidebands. We will now elaborate on different interpretations of the origin of the sideband creation to give more physical intuition. There are mainly three ways to understand this process.

- Atoms inside the cavity induce a phase shift on the light inside the cavity as discussed in Chapter 2. Therefore, classically, atoms can be consider as dielectric material with index of refraction proportional to the atomic density. Inside the cavity, the density grating can then be considered as stacks od dielectric material similar to a Bragg grating such as is used to make dielectric mirrors.. The cavity photons are reflected by this "grating" from both direction. But because the "grating" is moving along the cavity axis, the reflected light is Doppler shifted. The Doppler shifted light correspond to the blue and red sidebands.

- The microscopic picture of the red/blue sideband photons can be consider as the stimulated emission of the atoms. When atoms are in higher momentum state, absorbing a dressing laser photon and emitting a higher frequency photon leads to the transfer into a lower momentum state, and vice versa.

- With the same periodicity between the cavity mode and the atomic density grating, one can consider the cavity resonance being phase modulated, however, because the two sideband tones are not the same distance from cavity resonance, they are not equally well supported by the cavity, leading to an additional AM quality to the generated tones.

5.5 Effective Hamiltonian of momentum-exchange interaction.

To model the momentum exchange process, we begin by defining $\hat{\psi}^{\dagger}(p)$ and $\hat{\psi}(p)$ as creation and annihilation field operators of an atom with momentum p which are related to creation and annihilation operators in position space by $\hat{\psi}(Z) = \int \hat{\psi}(p) e^{ipZ/\hbar} dp$. Because the wave packets centered at $p_0 \pm \hbar k$ have a narrow momentum spread $\hbar k \gg \sigma_p$, we define $\hat{\psi}_{\uparrow}(p) = \hat{\psi}(p + p_0 + \hbar k)$, $\hat{\psi}_{\downarrow}(p) = \hat{\psi}(p + p_0 - \hbar k)$ operators that annihilate atoms at momentum $p + p_0 \pm \hbar k$ within a momentum range $p \in [-\hbar k, +\hbar k]$. Doing this will support understanding in terms of both wave packets and an effective pseudo-spin language.

We divide the differential kinetic energy between the two momentum states $p + p_0 \pm \hbar k$ into two terms: a homogeneous or common kinetic energy difference $\hat{H}_z(p) = \frac{\hbar\omega_z}{2}\left[\hat{\psi}^{\dagger}_{\uparrow}(p)\hat{\psi}_{\uparrow}(p) - \hat{\psi}^{\dagger}_{\downarrow}(p)\hat{\psi}_{\downarrow}(p)\right]$ and an inhomogeneous contribution $\hat{H}_{in}(p) = \frac{\hbar\omega_{in}(p)}{2}\left[\hat{\psi}^{\dagger}_{\uparrow}(p)\hat{\psi}_{\uparrow}(p) - \hat{\psi}^{\dagger}_{\downarrow}(p)\hat{\psi}_{\downarrow}(p)\right]$ with $\omega_{in}(p) = 2kp/m$.

We can adiabatically eliminate the cavity fields using second order perturbation theory (see Fig. 5.1B), and in the perturbative limit $|\Delta_d \pm \omega_z| \gg \sqrt{N}\left|\frac{\alpha_d\sqrt{\kappa_1}}{\Delta_d + i\kappa/2}\right| \frac{g_0^2}{4\Delta_a}$, we obtain an effective atomic-only momentum-exchange Hamiltonian

$$\hat{H}_{mx} = \iint_{-\hbar k}^{\hbar k} \left[\hbar\chi_{+}\hat{\psi}^{\dagger}_{\uparrow}(p)\hat{\psi}_{\downarrow}(p)\hat{\psi}^{\dagger}_{\downarrow}(q)\hat{\psi}_{\uparrow}(q) + \hbar\chi_{-}\hat{\psi}^{\dagger}_{\downarrow}(p)\hat{\psi}_{\uparrow}(p)\hat{\psi}^{\dagger}_{\uparrow}(q)\hat{\psi}_{\downarrow}(q)\right] dp\, dq \tag{5.1}$$

with the total Hamiltonian $\hat{H} = \hat{H}_{mx} + \int_{-\hbar k}^{\hbar k} \hat{H}_{in}(p)\, dp + \int_{-\hbar k}^{\hbar k} \hat{H}_z(p)\, dp$. The momentum exchange couplings are given by

$$\chi_{\pm} = \left(\frac{g_0^2}{4\Delta_a}\right)^2 \frac{|\alpha_d|^2\kappa_1}{\Delta_d^2 + \kappa^2/4} \frac{\Delta_d \pm \omega_z}{(\Delta_d \pm \omega_z)^2 + \kappa^2/4}\,, \tag{5.2}$$

where we have included finite cavity damping via appropriate Lindblad operators (see supplement.)

As discussed in Chap. 2 To map this to a pseudo-spin model, we define ladder operators $\hat{j}_{+}(p) = \hat{\psi}^{\dagger}_{\uparrow}(p)\hat{\psi}_{\downarrow}(p)$, $\hat{j}_{-}(p) = \hat{\psi}^{\dagger}_{\downarrow}(p)\hat{\psi}_{\uparrow}(p)$ and spin projection operators $\hat{j}_x(p) = \frac{1}{2}\left[\hat{j}_{+}(p) + \hat{j}_{-}(p)\right]$, $\hat{j}_y(p) = \frac{1}{2i}\left[\hat{j}_{+}(p) - \hat{j}_{-}(p)\right]$ and $\hat{j}_z(p) = \frac{1}{2}\left[\hat{\psi}^{\dagger}_{\uparrow}(p)\hat{\psi}_{\uparrow}(p) - \hat{\psi}^{\dagger}_{\downarrow}(p)\hat{\psi}_{\downarrow}(p)\right]$. Integrating over all momentum states, we can then define collective operators $\hat{J}_{\alpha} = \int_{-\hbar k}^{\hbar k} \hat{j}_{\alpha}(p)\, dp$ where $\alpha \in [x, y, z, +, -]$. The momentum-exchange Hamiltonian $\hat{H}_{mx}$ is then equivalent to an effective spin-exchange Hamilto-

nian $\hat{H}_{sx} = \chi_+ \hat{J}_+ \hat{J}_- + \chi_- \hat{J}_- \hat{J}_+$. This can be viewed as a collective XX-Heisenberg or Richardson-Gaudin integrable model where the non-local spin-spin couplings χ compete with an inhomogeneous axial field—a model often used in quantum magnetism and superconductivity via the spin Anderson mapping [119, 120, 121]. We also note that the standing-wave cavity mode's spatial intensity variation $\cos^2 kZ$ produces additional terms J_+^2 and J_-^2 that we can neglect due to the same perturbative limit because these terms do not conserve energy between the initial and final states shown in Fig. 5.1B (see supplement and [126].)

5.6 One-axis twisting dynamics.

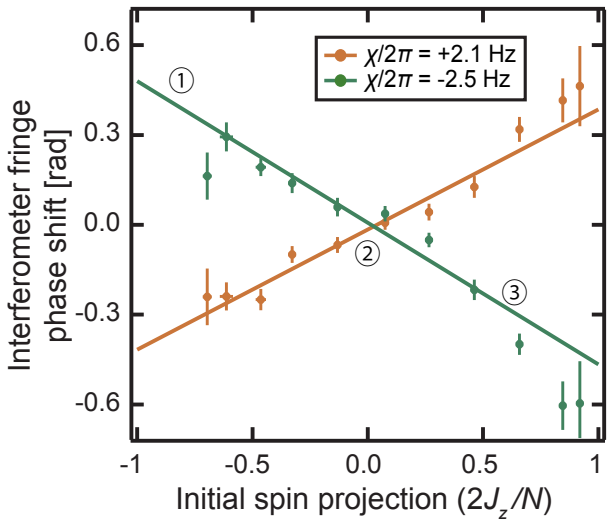

Figure 5.5: The measured interferometer phase shift scales linearly with the initial spin projection $J_z = \langle \hat{J}_z \rangle$, while now holding Δ_d fixed. The orange data points and fitted line is for $\chi/2\pi = +2.1$ Hz, and green for $\chi/2\pi = -2.5$ Hz).

The exchange Hamiltonian can be re-written as $\hat{H}_{sx} \approx \chi\left(\hat{J}^2 - \hat{J}_z^2\right)$ with $\chi = \chi_+ + \chi_-$, ignoring single-particle terms. At the mean field level, the one-axis twisting Hamiltonian $\chi \hat{J}_z^2 \approx 2\chi \langle \hat{J}_z \rangle \hat{J}_z$ induces a rotation of the collective Bloch vector about the z direction at a constant frequency, $2\chi \langle \hat{J}_z \rangle$, that depends on the initial momentum population difference $\langle \hat{J}_z \rangle$, which is conserved by the Hamiltonian $\hat{H}_{sx}$. In the equivalent matter-wave picture, the azimuthal phase, $\Delta\phi = 2\chi \langle \hat{J}_z \rangle t_x$ accumulated when the exchange interaction is applied for a time t_x, appears as a shift of the spatial

interference fringe between the two wave packets, see Fig. 5.5.

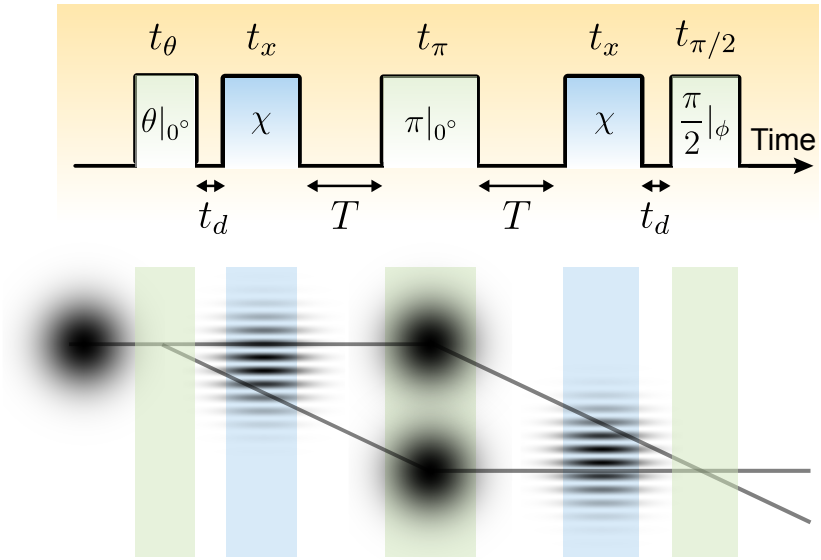

Figure 5.6: Matter-wave interferometer sequence and space-time diagram for observing all-to-all Ising or One-Axis Twisting dynamics. The interferometer fringe amplitude and phase shift $\Delta\phi$ are measured by scanning the phase of the final rotation ϕ.

To observe this phase shift, we run a matter-wave interferometer sequence (see Fig. 5.6) beginning with a Bragg $\pi/4$-pulse lasting 15 μs that prepares the atoms with population difference $\frac{\langle \hat{J}_z \rangle}{N/2} \approx -0.7$. After waiting a delay time $t_d = 25$ μs, we apply the dressing laser to create the exchange interaction for $t_x = 25$ μs. To re-overlap the wave packets or equivalently undo the inhomogeneity from $\hat{H}_{in}$, we then apply a Bragg π-pulse, and apply the dressing laser again before applying a final Bragg $\pi/2$-pulse with various phase ϕ. The final $\pi/2$-pulse maps the phase shift $\Delta\phi$ into a change in $\langle \hat{J}_z \rangle$. We measure the population in each momentum state by using velocity-sensitive Raman π-pulses and cavity-assisted quantum non-demolition measurements (see [11][G] and supplement.) We repeat the experiment while scanning the phase of the final $\pi/2$-pulse. The phase shift $\Delta\phi$ is then determined from the phase of the observed fringe $\left\langle \hat{J}_z \right\rangle$ versus ϕ.

The momentum-exchange coupling of Eq.(5.2) predicts a triple-dispersive structure as the detuning of the dressing laser Δ_d varies. We observe this predicted structure in Fig. 5.7 by measur-

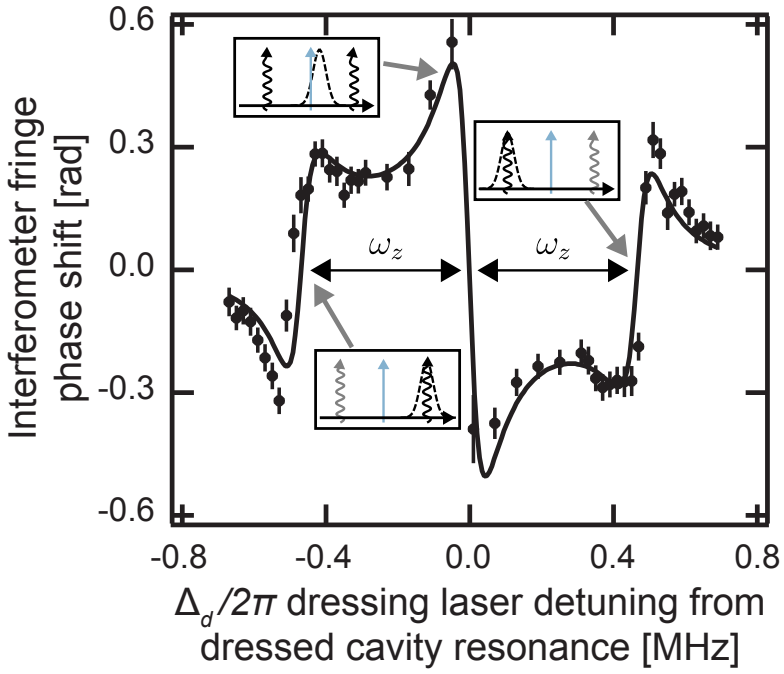

Figure 5.7: The observed phase shift $\Delta\phi$ of the interferometer fringe versus the dressing laser's detuning from the dressed cavity resonance, displaying the predicted (line) functional form of χ from Eq. 5.2. The insets illustrate the relative alignment of the modulation sideband to the cavity resonance for three characteristic detunings.

ing the induced phase shift $\Delta\phi$ as we vary the dressing laser detuning Δ_d from the dressed cavity resonance. In this data, the incident dressing laser power (350 photons/μs) is held fixed. The two outer dispersive features arise as the two sideband frequencies at $\pm\omega_z$ pass through resonance with the cavity as shown in the insets. The dispersive feature near $\Delta_d = 0$ arises from the carrier passing through resonance with the cavity. At $\Delta_d = 0$, the exchange interaction parameters are $\chi_+ \approx -\chi_-$ leading to a cancellation of the total exchange interaction ($\chi \approx 0$).

The phase shift $\Delta\phi$ is expected to scale linearly with $\left\langle \hat{J}_z \right\rangle$. We observe this by replacing the initial $\pi/4$-pulse with variable-length pulses to vary $\langle \hat{J}_z \rangle$ while holding Δ_d fixed instead. For the orange data in Fig. 5.5(A), the frequency of the relevant sideband is higher than the cavity resonance frequency leading to a measured $\chi/2\pi = +2.1$ Hz. For the green data, we retune the detuning Δ_d so that the relevant sideband frequency is lower than the cavity resonance frequency

leading to a measured $\chi/2\pi = -2.5$ Hz. We observe a linear phase shift $\Delta\phi$ for $\chi > 0$ and $\chi < 0$ with opposite slopes as expected.

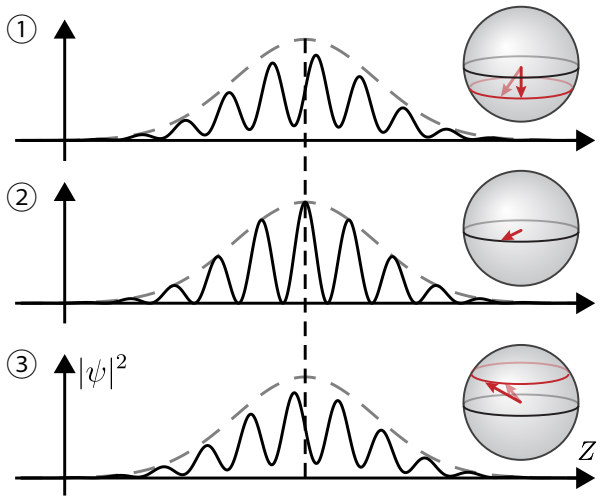

Figure 5.8: Visualizations of the phase shift $\Delta\phi$ in both the pseudo-spin picture (Bloch spheres) and in the atomic density grating picture.

We observe that the size of the phase shift $\Delta\phi$ decreases if the wave packets are allowed to separate for a time t_d before applying the dressing laser for time $t_x = 25$ μs to induce the momentum-exchange interaction. Fig. 5.6 (top) shows the pulse sequence used to measure this decay of the phase shift (bottom) for both positive and negative χ (orange and green points). For comparison, the solid lines indicate the predicted phase shifts for the full momentum-exchange Hamiltonian while the dashed lines indicate the predicted phase shift for an OAT Hamiltonian $-\chi\hat{J}_z^2$. The wave packet separation or equivalently the inhomogeneity $\hat{H}_{in}$ would not affect a pure OAT Hamiltonian as was the case in [11][G], whereas the phase shift is decreased by dephasing for exchange interaction as was observed in a spin system [98]. The wave packet separation leads to dephasing or shortening of the Bloch vector as visualized in Fig. 5.8. As the wave packets separate, the corresponding collective Bloch vectors are shortened while the projection $\langle\hat{J}_z\rangle$ is conserved.

5.7 Gap protection: binding wave packets together.

The additional non-linear term $\hat{J}^2$ in the momentum-exchange Hamiltonian gives rise to a many-body energy gap between states of higher symmetry (large J) and lower symmetry (smaller J) [98, 116]. To explore how matter-wave coherence is protected by the gap, we run a Mach-Zehnder interferometer as shown in Fig. 5.9 (top) in which we apply the dressing laser for a time t_x starting at the point of maximum reoverlap of the wave packets (with $T = 70$ μs).

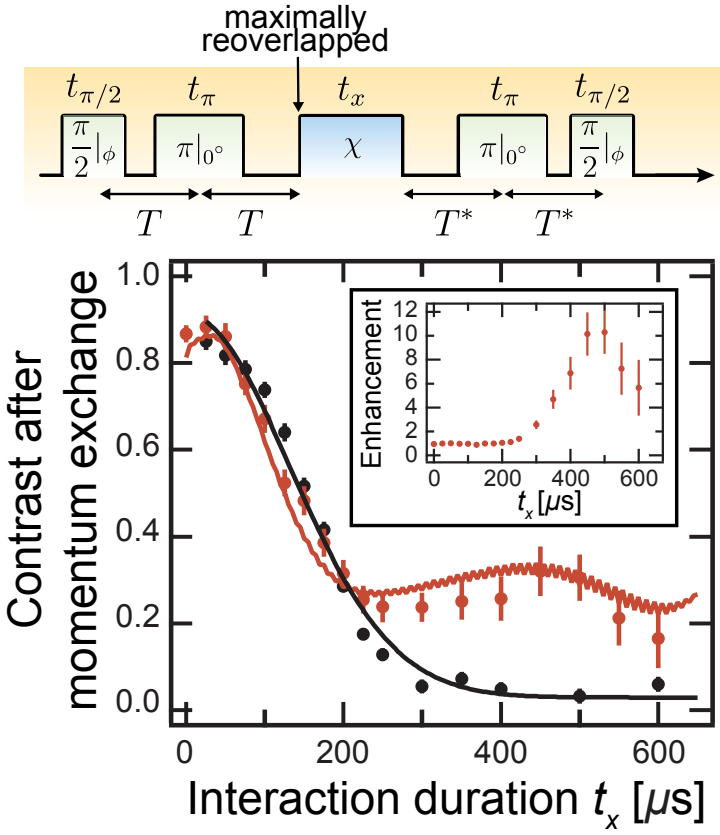

Figure 5.9: Using the sequence in the top panel, the bottom panel shows the contrasts of the interferometer fringe measured at the end of the exchange interaction period with $\chi = 0$ (black), $\chi/2\pi = 6$ Hz (red). The ratio between the two (inset) displays significant gap protection of coherence due to the momentum-exchange's $\hat{J}^2$ contribution. The simulated results (solid lines) show good agreement with the data.

The coherence at the end of the dressing laser application is estimated from the amplitude of the interferometer fringe using an appropriately timed π-pulse and a final $\pi/2$-pulse shown (with

$T^* = 70$ μs.) To account for the atomic loss resulting from free-space scattering and superradiance into higher momentum states, the contrast is calculated by normalizing the fitted fringe amplitude to the residual population in the two momentum states $p_0 \pm \hbar k$. The actual coherence of the system is higher due to the finite possibility of under-estimating the number of atoms that underwent free-space scattering. In Fig. 5.9, the experiment is performed with the dressing laser off ($\chi = 0$, black points and fitted black curve) and the dressing laser on ($\chi/2\pi = 6$ Hz, red points and theory curve), for which we observe appreciable fringe contrast survives out to 600 μs. In Fig. 5.9 inset, one sees that the momentum-exchange enhances the contrast by as much as a factor of 10(2). In Fig. 5.9, the coherence undergoes a slight rise before ultimately falling. This behavior can be accentuated by allowing the wave packets to undergo a small amount of separation for 40 μs before applying the momentum-exchange interactions for a duration t_x.

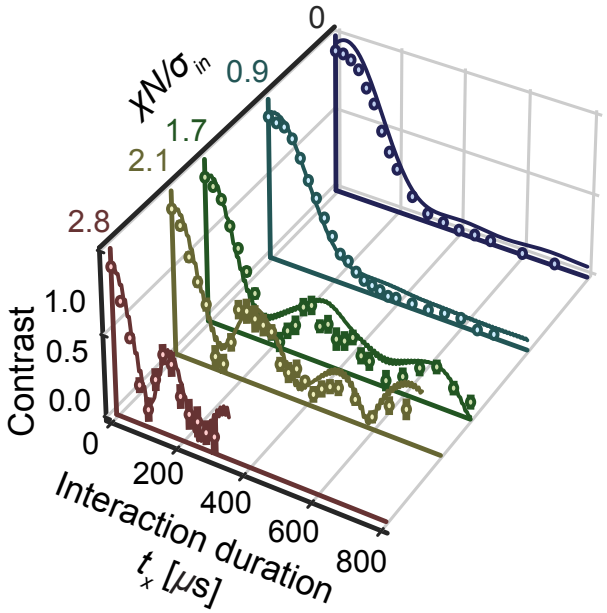

Figure 5.10: We run a similar sequence to that of Fig. 6.8C except with an additional 40 μs delay after wave packet overlap before application of the dressing laser for a variable time t_x. We see that as the interaction strength is increased relative to the rms inhomogeneous broadening $\sigma_{in} = 2\pi \times 2$ kHz, there is a transition in the dynamics for $N\chi/\sigma_{in} > 0.9$. Strikingly, there are also clear oscillations that were only hinted at in Fig. 6.8C. The lines are theory predictions.

The observed interferometer contrast versus t_x (see Fig. 5.10) is measured at different dressing laser powers to obtain different ratios of χN to the rms inhomogeneity from $\hat{H}_{in}$ expressed as a

frequency σ_{in}. We observe a sharp transition in the dynamical behavior between $\chi N/\sigma_{in} = 0.9$ and 1.7 with the emergence of oscillations of the contrast that extend to long times as χN increases. The oscillations become faster and have larger amplitudes at shorter times as χN increases. This behavior is reasonably consistent with the overlayed theory simulations (colored traces in Fig. 5.10) that include finite superradiance and where only σ_{in} is fit from the data with $\chi N = 0$.

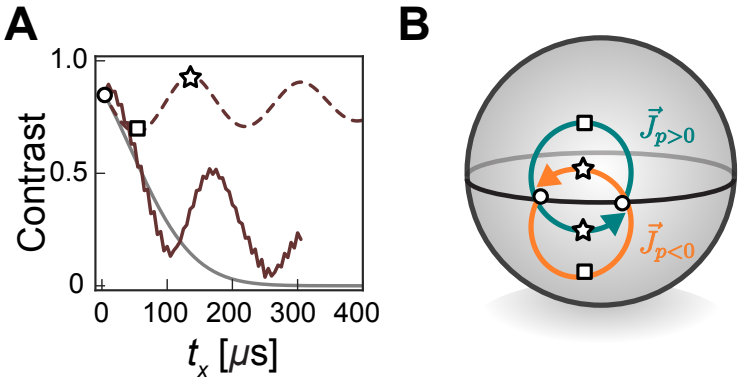

Figure 5.11: **(A)** The theory prediction with residual superradiance on (solid) and turned off (dashed) are shown with three example points in the oscillations labeled, and with no interactions (grey). **(B)** The total length of the pseudo-spin Bloch vector $\vec{J}$ oscillates in time because the individual Bloch vectors oscillate as shown for $\vec{J}_{p>0}$ and $\vec{J}_{p<0}$ in green and orange respectively, with $\chi N/\sigma_{in} = 2.8$.

The extension of coherence to longer times and the observed oscillations can be understood as the momentum-exchange interaction causing the wave packets to become bound to each other such that they no longer freely separate. In Fig. 5.11A, we show the simulated variation of the contrast versus time without superradiance, high lighting three example points that we explain using the simulated trajectories in Fig. 5.11B for the collective pseudo-spin Bloch vectors evaluated for $p > 0$ or $p < 0$ with $\vec{J}_{p>0} = \int_0^{\hbar k} \vec{j}(p)\, dp$ and $\vec{J}_{p<0} = \int_{-\hbar k}^{0} \vec{j}(p)\, dp$ where $\vec{j}(p) = \left\langle \hat{j}_x(p)\hat{x} + \hat{j}_y(p)\hat{y} + \hat{j}_z(p)\hat{z} \right\rangle$.

In Fig. 5.12, we also show the simulated results without superradiance for the individual wave packets in both momentum and position space. In the pseudo-spin picture, the momentum-exchange causes the displayed vectors $\vec{J}_{p>0}$ and $\vec{J}_{p<0}$ to undergo orbits that oscillate symmetrically above and below the equator such that the total Bloch vector length oscillates in time. In the wave packet picture, with no interactions, the wave packet centers would follow the diverging dashed

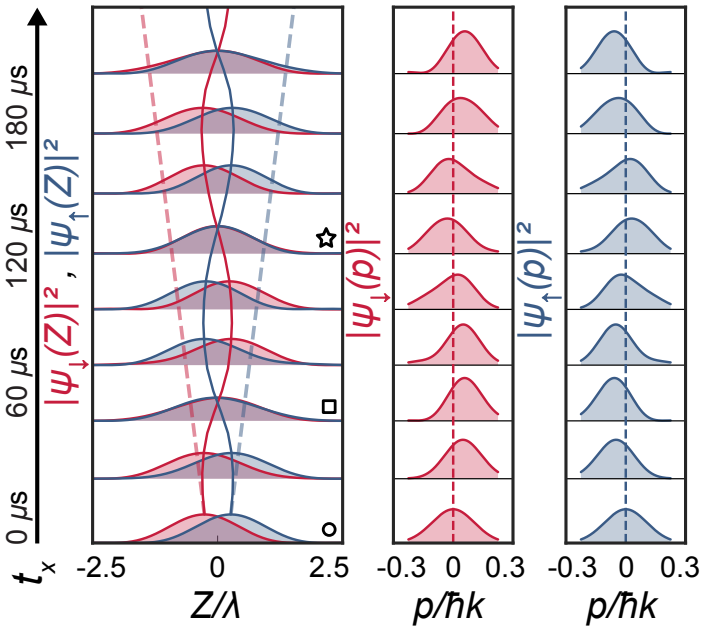

Figure 5.12: (left) In a co-moving frame, the wave packets oscillate in time about their average position in space (blue and red wave packets and centers solid lines, non-interacting system dashed lines.) The momentum-space wave packets (right) also oscillate but with a $\pi/2$ phase shift in time relative to the position space wave packets, as would be the case for a harmonic oscillator.

lines. With interactions, the wave packets oscillate in position with respect to each other, while also oscillating in their momentum p, as though the wave packets are now connected by a spring with characteristic frequency set by the exchange interaction strength χN in the limit that $\chi N \gg \sigma_{in}$ and for small wave packet separation. If the wave packets are allowed to initially separate before the spring-like coupling is turned on, then the amplitude of the oscillations of the wave packet separations (and hence the contrast) will be larger as was observed in Fig. 5.10.

To further explore this idea of wave packets becoming bound to each other, we run a Mach-Zehnder matter-wave interferometer with the sequence shown in Fig. 5.13 (top). If the exchange interaction is not applied (Fig. 5.13 red points and fit), then the fringe contrast is maximized when the echo time difference is $\Delta T = 0$ since this is when the wave packets have maximal reoverlap. If the momentum exchange interaction is applied just after the first splitting pulse, we see that the point of maximum contrast is shifted to $\Delta T = -55$ μs (blue points and simulation), and

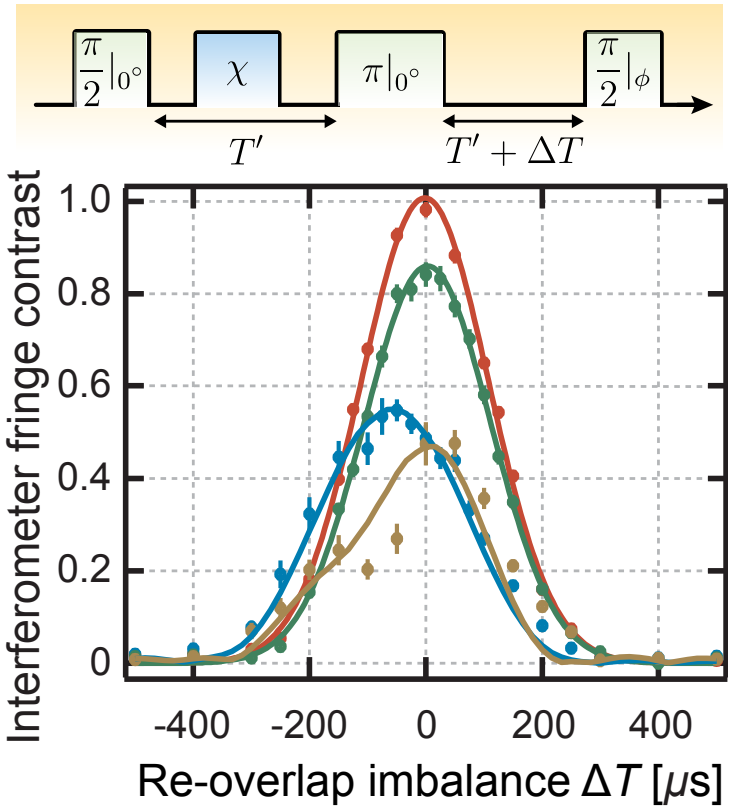

Figure 5.13: The interferometer contrast as a function of imbalance in the time from nominal perfect reoverlap of the wave packets with: no momentum-exchange (red data and fit), momentum-exchange applied right after first $\pi/2$ at intermediate power (blue data and theory) and high power (brown data and theory), and momentum-exchange applied when wave packets are separated (green data and fit).

becomes non-Gaussian (brown points and simulation) at even higher dressing laser power. We rule out single-particle effects that might also shift the maximal reoverlap time by repeating the experiment, but with the dressing laser applied 1 ms after the first splitting pulse when the wave packets are not overlapped (green points and fit), which also suppresses collective superradiance, leading to the higher observed contrast. The fact that the delay is modified by 55 μs rather than $t_x = 25$ μs (as one might naively expect should one think of the wave packet separation as being frozen in place during the exchange interaction) arises from a 25 μs delay between the end of the $\pi/2$-pulse and the beginning of the interaction, and the fact that the nature of the coupling of the wave packets is harmonic-oscillator-like.

In order to emphasize the extreme unusualness of the binding of the wave packets, consider a **gedanken** experiment in which a single photon combined with a coherent state of light drives the two-photon Bragg transition with total momentum transfer to the atomic cloud $2\hbar k$. Given that one can not tell which atom underwent the two-photon transition, the initial state should be symmetrized with respect to which atom absorbed the single photon, analogous to a Dicke or W state (see supplement). Without exchange interactions, at long times one would observe a single atom eventually emerge from the cloud with velocity $v_{rec} = (2\hbar k)/m$ while all other atoms remain at their initial momentum. In contrast, with the momentum-exchange interaction, one would never observe a single atom to emerge with velocity v_{rec}. Instead the whole cloud of N atoms would collectively recoil with velocity v_{rec}/N (see supplement).

This collective recoil is analogous to Mössbauer spectroscopy (or Lamb-Dicke spectroscopy) in which atoms embedded in a crystal cause the whole crystal to recoil when the atoms absorb light. In our case the collective recoil mechanism enabled by strong exchange interactions suppresses Doppler dephasing or line broadening. However, unlike Mössbauer spectroscopy, it does not suppress the photon recoil shift which here defines the transition frequency ω_z between the two momentum states.

5.8 Collective recoil and Suppression of Doppler Dephasing

To further elaborate on the unusualness of the momentum-exchange interaction and the **gedanken** experiment. Here, we expand and analyze this observation from three different perspectives. We first focus on the case with only one atom undergoing the two-photon transition and elucidate the collective recoil with an analytical derivation. We then generalize it to allow for more initial recoiling atoms using mean-field numerical simulations of the wave packet dynamics. The simulations explicitly show the the collective recoil of the total atomic wave packet which results in the enhanced coherence observed in the Ramsey-type experiment in the main text.

In Mössbauer spectroscopy, Doppler broadening of a Rabi spectrum is suppressed because the whole crystal collective recoils rather than just a single photon-absorbing atom embedded in the

crystal. We present numerical simulations that show that Doppler broadening of a Rabi spectrum is also suppressed by the gap protection term $\hat{J}^2$.

We first consider initializing the system with N atoms having the same momentum distributions centered at $p_0 - \hbar k$. The quantum state of the system can be expressed in second quantization as $|\psi_{ini}\rangle = \frac{1}{\sqrt{N!}} \left(\int_{-\hbar k}^{+\hbar k} \phi(p) \hat{\psi}^\dagger(p) dp \right)^N |vac\rangle$ with $|vac\rangle$ the vacuum state in which there are no atom present and $\phi(p) \propto \exp\{-p^2/4\sigma_p^2\}$ the probability amplitude distribution with rms spread in probability σ_p. We then introduce a different basis set $|N_a, N_b\rangle$ in which N_a denote the number of atoms with momentum $\in (p_0 - 2\hbar k, p_0)$ and N_b atoms the number of atoms with momentum $\in (p_0, p_0 + 2\hbar k)$. In this new basis, the initial state can be expressed as $|\psi_{ini}\rangle = |N, 0\rangle$.

The **gedanken** experiment described in the main text considers a single photon combined with a coherent state of light driving the two-photon Bragg transition. One can not tell which atom absorbed the single photon and underwent the two-photon transition, such that the state should be symmetrized with respect to which atom experiences the $2\hbar k$ momentum transfer. The resulting state can be expressed as

$$|\psi_0\rangle = |N-1, 1\rangle = \frac{\sum_p \hat{\psi}_\uparrow^\dagger(p) \hat{\psi}_\downarrow(p)}{\sqrt{N}} |N, 0\rangle \,, \tag{5.3}$$

with the sum implicitly over discrete states between $\pm\hbar k$. This initial state then evolves under the Hamiltonian $\hat{H} = \hat{H}_{kin} + \hat{H}_{int}$:

$$\hat{H}_{kin} = \sum_p \frac{(p_0 - \hbar k + p)^2}{2m} \hat{\psi}_\downarrow^\dagger(p) \hat{\psi}_\downarrow(p) + \sum_p \frac{(p_0 + \hbar k + p)^2}{2m} \hat{\psi}_\uparrow^\dagger(p) \hat{\psi}_\uparrow(p) \tag{5.4}$$

$$\hat{H}_{int} = \chi \sum_{p,q} \hat{\psi}_\uparrow^\dagger(p) \hat{\psi}_\downarrow(p) \hat{\psi}_\downarrow^\dagger(q) \hat{\psi}_\uparrow(q) \tag{5.5}$$

The first term is the kinetic energy and second the exchange-interaction.

Without applying the interaction ($\chi = 0$), after time evolution the final state becomes

$$|\psi_{free}(t)\rangle = \hat{U}_0 |\psi_0\rangle \,, \tag{5.6}$$

with $\hat{U}_0 = \exp\left[-i\hat{H}_{kin}t/\hbar\right]$. We can then calculate the spatial probability distribution:

$$\langle\psi_{free}(t)|\,\hat{c}_Z^\dagger\hat{c}_Z\,|\psi_{free}(t)\rangle \propto (N-1)\exp\left[-\frac{\left(Z-\frac{p_0-\hbar k}{m}t\right)^2}{2\sigma_Z^2(t)}\right]+\exp\left[-\frac{\left(Z-\frac{p_0+\hbar k}{m}t\right)^2}{2\sigma_Z^2(t)}\right], \quad (5.7)$$

where the $\hat{c}_Z^\dagger \propto \sum_p \hat{\psi}_\downarrow^\dagger(p)e^{-i(p_0-\hbar k+p)Z/\hbar}+\sum_p \hat{\psi}_\uparrow^\dagger(p)e^{-i(p_0+\hbar k+p)Z/\hbar}$ is the operator for creating an atom at position Z, and $\sigma_Z(t)=\frac{\hbar}{2\sigma_p}\sqrt{1+\left(\frac{2\sigma_p^2 t}{m\hbar}\right)^2}$ is the rms spread of the wave packets in position space. The result above corresponds to two Gaussian distributions moving at different velocities with heights proportional to the number of atoms in each momentum distribution centered at $p_0 \pm \hbar k$.

Now we turn to the case with interaction applied. The initial Dicke-like state $|\psi_0\rangle$ of Eq. 5.3 is an eigenstate of $\hat{H}_{int}$ with eigenvalue χN as discussed in before. On the other hand, $\hat{H}_{kin}$ couples the symmetrized Dicke-like state to other eigenstates of the interaction Hamiltonian that are separated by an energy gap χN [98]. In the limit $\chi N \gg \sigma_{in}$, we can consider $\hat{H}_{kin}$ as a perturbation of $\hat{H}_{int}$, with the time evolution being governed by the projection of $\hat{H}_{kin}$ onto the initial Dicke-like state with operator $\hat{P}=|N-1,1\rangle\langle N-1,1|$.

$$|\psi_{int}(t)\rangle = \hat{U}_0'\,|\psi_0\rangle\,, \quad (5.8)$$

with $\hat{U}_0' = \exp\left[-i\hat{P}\hat{H}_{kin}\hat{P}t/\hbar\right]$. We can then calculate the spatial probability distribution:

$$\langle\psi_{int}(t)|\,\hat{c}_Z^\dagger\hat{c}_Z\,|\psi_{int}(t)\rangle \propto \exp\left[-\frac{\left(Z-\frac{\bar{p}t}{m}\right)^2}{2\sigma_Z^2(t)}\right], \quad (5.9)$$

which corresponds to a single Gaussian wave packet moving at the velocity $\bar{p}/m=\frac{N-1}{N}\frac{p_0-\hbar k}{m}+\frac{1}{N}\frac{p_0+\hbar k}{m}$. Relative to the co-moving frame of the atoms before absorbing the single photon, this corresponds to a velocity of $\frac{1}{N}\frac{p_0+\hbar k}{m}$. Thus the momentum-exchange interaction leads to collective recoil of the atomic ensemble at a velocity reduced by $1/N$.

We now consider the case where N atoms starts with a momentum distribution centered at $p_0-\hbar k$ and a coherent two-photon Bragg coupling is applied to place the atoms in a superposition of momentum states such that on average $\bar{M}$ atoms undergo the two-photon transition. In this scenario, the Bragg pulse transfers $\bar{M}2\hbar k$ of total momentum to the atomic ensemble. In Fig. 5.14,

we perform mean-field numerical simulations of the wave-packet spatial probability distribution without interactions and with a Heisenberg interaction $\hat{J}^2$ provided by the momentum-exchange interactions but neglecting the Ising or OAT contribution $\hat{J}_z^2$. We consider three initial Bragg pulses areas ($\pi/4, \pi/2$ and $3\pi/4$) to achieve $\bar{M}/N \approx 0.15, 0.5$ and 0.85 and simulate the evolution of the spatial probability distributions of the atoms as a function of time of flight period T_{TOF} after the initial Bragg pulse.

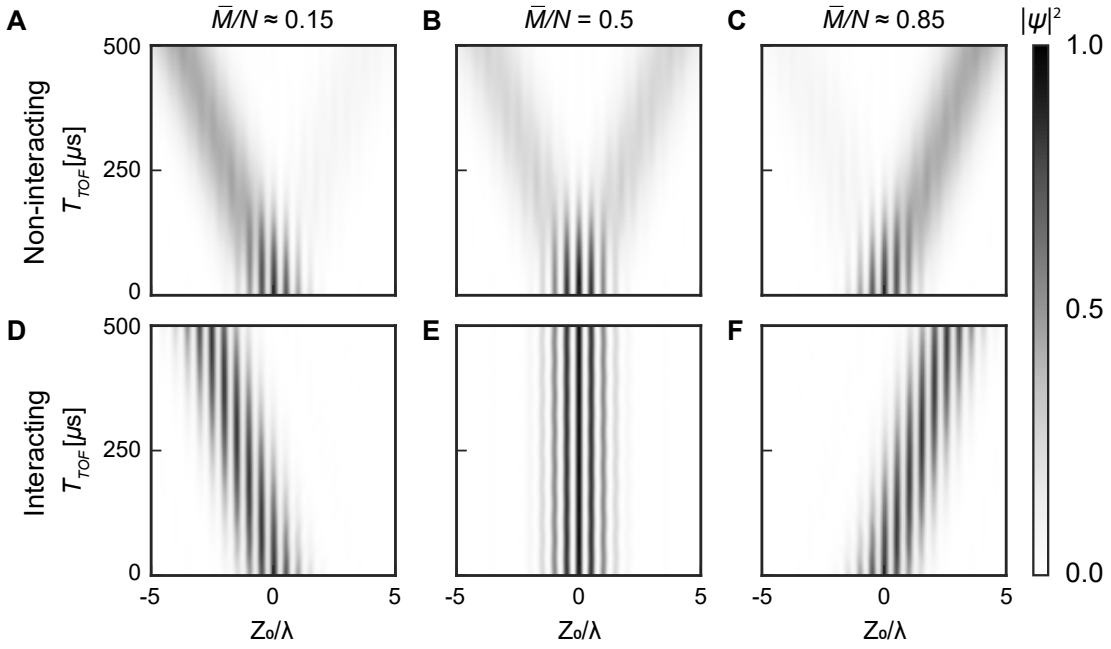

Figure 5.14: **Simulated evolution of the wave packets (credit: Haoqing Zhang.)** Evolution of the spatial probability distributions in the moving frame defined by the p_0 state with $Z_0 = Z - \frac{p_0}{m}t$. With all atoms initialized in $p_0 - \hbar k$ momentum state, $\pi/4$, $\pi/2$ and $3\pi/4$ Bragg pulses are applied to achieve different fractions of the initial recoiling atoms. With no interaction applied (χ=0), the interference fringes start to disappear as the wave packets separate into two for $\bar{M}/N$ =0.25 (A), 0.5 (B) and 0.75 (C). As a comparison, with the interaction applied ($\chi_{\pm} N \gg \sigma_{in}$), the wave packets do not separate but instead move at an averaged velocity determined by $\bar{M}/N$ as shown in (D), (E) and (F).

As shown in Fig. 5.14 (A) to (C), without the interaction ($\chi N = 0$), the wave packets separate into two with increasing T_{TOF}, which also leads to the vanishing interference fringes. The disappearance of the interference fringes caused by the two wave packets separating is precisely Doppler dephasing in this wave-packet picture. With the interaction applied ($\chi N \gg \sigma_{in}$), as

shown in Fig. 5.14 (D) to (F), the wave packets no longer separate but instead move at velocity proportional to $\bar{M}/N$. Note that the interference fringes now persist because the atoms collectively recoil as a single wave packet. This is why the collective recoil mechanism leads to a suppression of the Doppler dephasing.

One also notices that the fringes are stationary in the reference frame of Fig 5.14, independent of $\bar{M}/N$. This implies that the fringes always move at a velocity p_0/m in the lab frame. If one considers an acceleration a_Z (such as due to gravity), the momentum p_0 now goes to $p_0 \rightarrow p_0 + m\,a_Z\,t$. The changing velocity of the interference fringes provides the interferometric sensitivity to accelerations, even in the presence of the Heisenberg interaction $\hat{J}^2$.

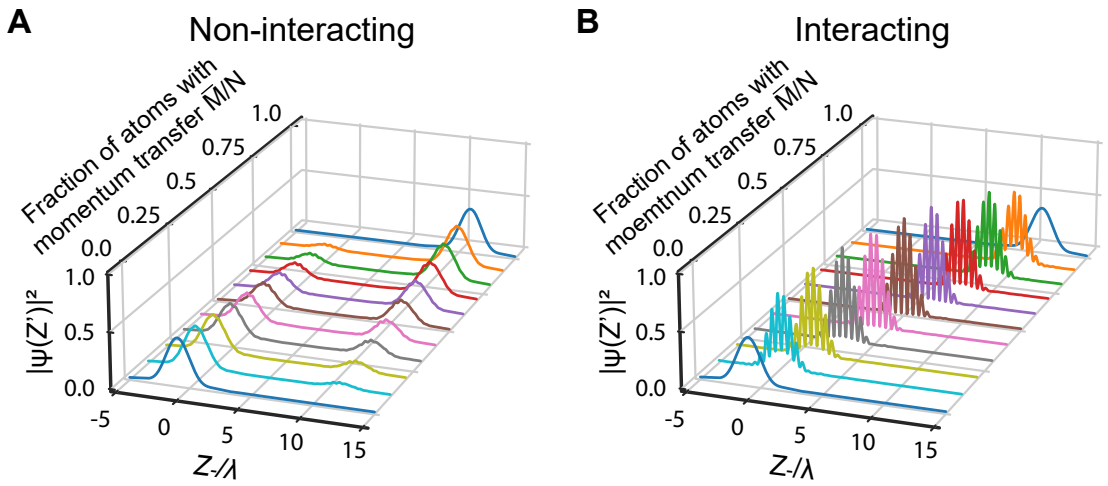

Figure 5.15: **Simulation of collective recoil (credit: Haoqing Zhang.)** Simulated spatial probability distributions of the wave functions after evolution in the moving frame defined by the $p_0 - \hbar k$ state with $Z_- = Z - \frac{p_0 - \hbar k}{m} t$. **(A)** Without the interaction applied, the wave packets split into two regardless of the fraction of initial recoiled atoms. **(B)**After turning on the interaction, the wave packets no longer separate but instead recoil together with an averaged momentum across the whole ensemble.

By fixing the time of flight period $T_{TOF} = 500\ \mu$s, we can also compare the results with different fractions of initial recoiling atoms $\bar{M}/N$. As shown in Fig. 5.15, when there is no interaction applied, as one expects, the atoms are only found in two spatially distinct regions corresponding to either having not absorbed two-photon recoil or having absorbed two-photon recoil and gaining a velocity $v_{rec} = 2\hbar k/m$. Varying the number of two-photon momentum kicks $\bar{M}$ only varies the

fraction of atoms found in one spatial region or the other, but not the centers of the two distinct spatial regions.

However, when the momentum-exchange interaction is much larger than the Doppler broadening $|\chi N| \gg \sigma_{in}$, one sees in Fig. 5.15B that now the atoms recoil as a single wave packet with wave packet velocity $v = \frac{\bar{M}}{N} v_{rec}$ that depends on the fraction of atoms $\bar{M}/N$ that underwent two-photon absorption. For simplicity, the simulations above included only the gap protection term $\hat{J}^2$ and neglected the Ising term $\hat{J}_z^2$ as this latter term only shifts the phase of the interference fringes within the wavepacket, but does not alter the collective wavepacket recoil velocity.

5.9 Summary.

We have realized a cavity-mediated momentum-exchange interaction between different momentum states for the first time. By measuring the phase shift induced by this momentum exchange interaction, we observe the collective OAT dynamics, which paves the way for entanglement generation between momentum states [117, 118] and the study of beyond mean-field physics. We also directly observe an extension of the coherence time of the system which we identify with a collective recoil mechanism. The collective recoil mechanism still allows for the sensing of accelerations a_Z such as due to gravity (see supplement), since the phase difference that accrues between the two momentum states still depends on ω_z which chirps as $\omega_z \to 2k\,(p_0/m + a_Z t)$. Equivalently, the atoms still act as a phase memory of the optical Bragg pulses with which they interact [40][G]. This opens interesting new paths for enhancing quantum memory lifetime [127], for Doppler-broadening-free spectroscopy, and for matter-wave interferometers that do not rely on spin-echo like sequences and therefore would also allow measurements of velocities rather than accelerations.

Finally, we note that the momentum-exchange Hamiltonian here is equivalent to the model Hamiltonian often used to describe BCS s-wave superconductors. From this perspective, the observed oscillations can be identified with Higgs oscillations following a quench of the exchange interaction strength [119, 128, 129]. This would enable quantum simulation of BCS superfluidity and also sets the stage for quantum simulation that goes beyond two-level systems by encoding

degrees of freedom in the larger ladder of momentum states [130, 131] as well as internal states [132, 133, 134, 135, 136, 137]. The large number of synthetic dimensions in combination with the long-range cavity mediated interactions, open unique opportunities for the emulation of self-generated spin-orbit coupling [138, 139], pair production [97, 140, 141, 142, 143, 144, 145, 146], long sought but never seen topological superfluids [147], and dynamical gauge fields [148, 149, 150, 151, 152]. Lastly, the generation of sideband tones may open a path to transduce excitations between matter waves and mesoscopic opto-mechanical systems [115, 114] or back-action evading measurements of matter waves as proposed for spins [153].

Chapter 6

Hamiltonian engineering of momentum states

Quantum control of momentum states is important for precision measurements. However, limited by the lack of controllable many-body interaction, momentum qubits are not ideal for quantum simulation and entanglement generation. Recent progress demonstrated an exchange interaction between two momentum states assisted by a high-finesse cavity [12]. Here, we generalize such approach to achieve more four-photon processes and realize an all-to-all interaction with arbitrary quadratic Hamiltonian or effectively an infinite range tunable Heisenberg XYZ model between two atomic momentum states. We demonstrate the tunability of the Hamiltonian by explicitly mapping out the evolution of Bloch vectors on the Bloch sphere at the mean-field level and witness the two-axis counter-twisting dynamics for the first time. Our work paves the way towards quantum simulation of more complex systems and fast robust entanglement generation with momentum states for future quantum enhanced metrology.

6.1 Introduction

The ability to create and control different many-body interactions is key for entanglement generation, optimization, quantum sensing, and quantum simulation. Long-range interacting systems have recently shown much promise for the engineering of Hamiltonians that generate interesting correlations that propagate across the system. Several experimental platforms are making rapid progress, including Rydberg atoms [154, 155, 156], polar molecules [157, 158], trapped ions [159, 160], cavity QED systems [138] and defect centers in solids [161, 162]. Short range contact

interactions in ultra-cold atomic systems are another promising approach [163, 164, 165], however, it remains an open challenge to reach the sufficiently low-temperatures.

So far, most efforts to engineer Hamiltonians have been limited to XXZ spin models or models that feature both exchange and Ising interactions. Common to these models is the fact that the total magnetization of the spin ensemble is preserved. However, limited progress has been achieved in engineering more general spin models, such as XYZ models, which can break both SU(2), and U(1) symmetries and lead to more general ground-state and out-of-equilibrium many-body behaviors. A few exceptions include experiments in Rydberg atoms using two-color dressing [166] with dynamics limited to pairs of atoms, or Floquet engineering in disordered arrays [155].

XYZ Hamiltonians can in fact provide important gains in the context of quantum sensing and metrology applications. For instance, the so called two-axis counter-twisting (TACT) [16] model is one type of XYZ model well known for its capability to generate entanglement exponentially fast all the way to the Heisenberg bound. It was proposed more than 30 years ago [167, 16] together with a simpler version, the so-called one-axis twisting (OAT) featuring only Ising interactions. So far, only the OAT has been realized in experiments including trapped ions [30, 168], Bose-Einstein Condensates [28, 29], atomic cavity-QED [33, 78, 98, 116], superconducting qubits [23] and optical interferometers [169]. Experiments have approximated TACT dynamics locally on the Bloch sphere by combining OAT with a transverse drive (the so-called Lipkin-Meshkov-Glick (LMG) model) [170, 171, 172] or equivalent approximations in spin-nematic dynamics in higher spin systems [66, 67]. However, there has been no demonstration of genuine TACT in any platforms due to the challenge of how to realize this more complex non-linear Hamiltonian.

Here we experimentally show that photon-mediated interactions between atoms inside an optical cavity can be tuned to realize a tunable all-to-all Heisenberg XYZ Hamiltonian, including the TACT model, with the added benefit of not requiring us to prepare extremely low entropy quantum degenerate gases. While there have been prior theory proposals to realize TACT models in atom-cavity systems using four laser tones [173, 174], here we experimentally realize the model using only two dressing lasers. We demonstrate the tunability of the XYZ Hamiltonian by explicitly

mapping out the evolution of Bloch vectors on the Bloch sphere at the mean-field level and witness the TACT dynamics for the first time.

The pseudo-spin system here is novel, consisting of two momentum states of atoms freely-falling inside the cavity, making our results of great interest for Bragg matter-wave interferometers [175] that are important for both inertial navigation and fundamental science such as searches for dark matter and dark energy, detection of gravitational waves, and determination of the fine structure constant [20, 21]. This approach can also be straightforwardly applied to systems with additional internal levels, making it ideal for developing next-generation quantum-enhanced sensors for technology and exploring a broad range of science from atomic clocks [76, 108] and magnetometers [176, 177, 178] to geodesy [179].

6.2 Experimental setup

In the experiment, ^{87}Rb atoms are laser-cooled inside a vertically-oriented two-mirror standing wave cavity, see Fig. 6.1 and [12, 11][G]. A repulsive intra-cavity doughnut dipole trap confines the atoms radially, but allows the atoms to fall along the cavity axis. To prepare atoms in a well-defined momentum state, a pair of laser beams are injected into the cavity to drive velocity-dependent two-photon Raman transitions between ground hyperfine states $|F = 1, m_F = 0\rangle$ and $|F = 2, m_F = 0\rangle$. After removing the unselected atoms with a resonant laser push beam, successive microwave pulses are applied to prepare the internal states of the selected atoms in the ground hyperfine state $|F = 2, m_F = 2\rangle$ (see [12][G]).

With about 700 atoms centered at momentum $p_0 - \hbar k$, another pair of laser beams is injected along the cavity axis to drive two-photon Bragg transitions connecting the two momentum states $|p_0 \pm \hbar k\rangle$ which defines a two-level spin-1/2 system [11, 12][G]. Here the average momentum is p_0, $\hbar$ is the reduced Plank constant, and $k = 2\pi/\lambda$ where λ is the wavelength of the Bragg laser beams. Due to finite momentum spread, one can consider momentum wave packets centered at these two momentum states as considered in detail previously [12][G]. Ignoring the finite momentum spread of the selected momentum states, we define $\hat{\psi}^\dagger_{\uparrow,\downarrow}$ and $\hat{\psi}_{\uparrow,\downarrow}$ as the operators for creating and

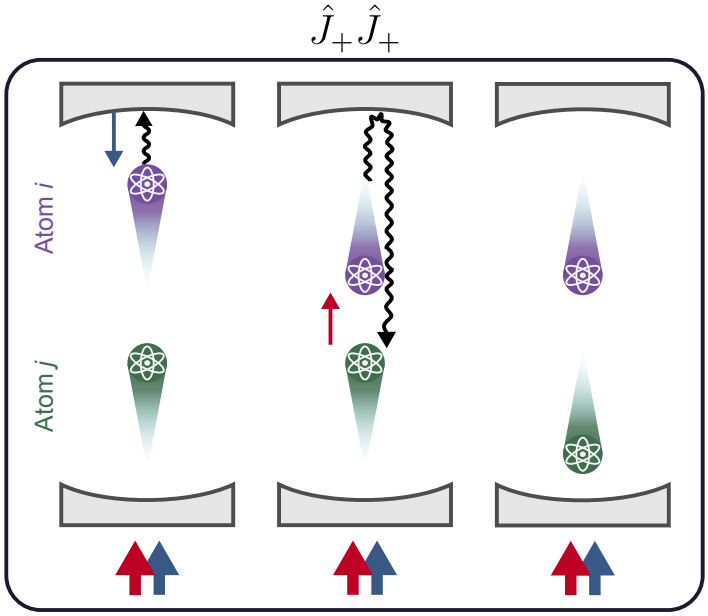

Figure 6.1: **Experimental overview.** Illustration of the microscopic momentum pair raising process described by the Hamiltonian $\hat{J}_+\hat{J}_+$, using two momentum states $p_0 \pm \hbar k$ as a pseudo-spin 1/2 degree of freedom. Initially, two atoms i and j are in the same momentum state along the cavity axis. Dressing lasers are applied to the cavity (red and blue arrows) that allow atom i to absorb a dressing laser photon and emit a photon (squiggly line) into the cavity such that the net photon recoil flips its momentum state by $2\hbar k$. The emitted photon is absorbed by atom j, also flipping its momentum state by $2\hbar k$. There also exists the separate momentum exchange process $\hat{J}_+\hat{J}_-$, where atoms initially in opposite momentum states flip their momentum states by emitting and absorbing photons.

annihilating an atom in momentum states $|\uparrow\rangle \equiv |p_0 + \hbar k\rangle$ and $|\downarrow\rangle \equiv |p_0 - \hbar k\rangle$. For mapping to a pseudo-spin model, we define ladder operators $\hat{J}_+ = \hat{\psi}^\dagger_\uparrow \hat{\psi}_\downarrow$, $\hat{J}_- = \hat{\psi}^\dagger_\downarrow \hat{\psi}_\uparrow$ and spin projection operators $\hat{J}_x = \frac{1}{2}\left(\hat{J}_+ + \hat{J}_-\right)$, $\hat{J}_y = \frac{1}{2i}\left(\hat{J}_+ - \hat{J}_-\right)$ and $\hat{J}_z = \frac{1}{2}\left(\hat{\psi}^\dagger_\uparrow \hat{\psi}_\uparrow - \hat{\psi}^\dagger_\downarrow \hat{\psi}_\downarrow\right)$.

As shown in Fig. 6.2, the cavity frequency ω_c is detuned from the atomic cycling transition $|F = 2, m_F = 2\rangle \rightarrow |F' = 3, m_{F'} = 3\rangle$ by $\Delta_a = \omega_c - \omega_a = 2\pi \times 500$ MHz, which is much larger than the excited state decay rate $\Gamma = 2\pi \times 6$ MHz and the cavity power decay rate $\kappa = 2\pi \times 56(3)$ kHz. A series of Bragg pulses can be applied to realize a Mach-Zehnder matter-wave interferometer (i.e. $\pi/2 - \pi - \pi/2$), in which the wave packets first separate in position and then re-overlap. When the two wave packets are overlapped, the interference between them forms an atomic density grating with period $\lambda/2$, which matches the standing wave of a cavity mode.

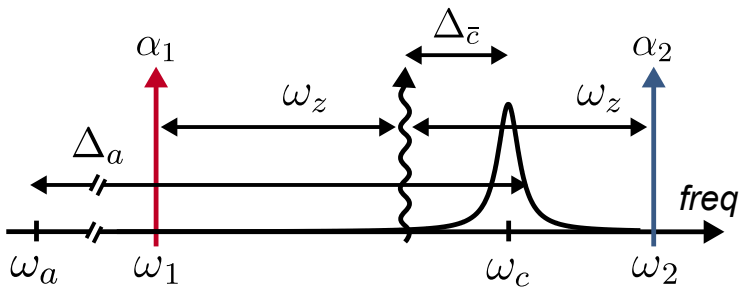

Figure 6.2: Frequency diagram of the applied dressing lasers with frequencies $\omega_{1,2}$ and coherent state amplitudes $\alpha_{1,2}$. The emitted photons (squiggly line) are Doppler shifted by ω_z from the dressing laser frequencies and detuned by Δ_c from the cavity resonance frequency ω_c. The cavity is far detuned from the atomic transition frequency ω_a.

As the atoms move along the cavity axis, the density grating is periodically aligned to the standing-wave of the cavity mode, leading to modulation of the cavity resonance frequency at the two-photon Doppler frequency $\omega_z = 2kp_0/m \approx 2\pi \times 500$ kHz, where m is the mass of ^{87}Rb. To have this modulation to mediate an effective atom-atom interaction, we typically apply two σ^+ polarized dressing laser tones (see Fig. 6.1) at frequencies $\omega_{1,2}$ within a few MHz of the cavity resonance frequency (see Fig. 6.2), with complex amplitudes $\alpha_{1,2}$ corresponding to the field that would be established inside the cavity were no atoms in the cavity and implicit units $\sqrt{\text{photons}}$. The atom–induced cavity frequency modulation leads to the generation of modulation sideband tones at frequencies $\omega_{1,2} \pm \omega_z$. In the following simplifications, we will assume $\omega_2 > \omega_1$.

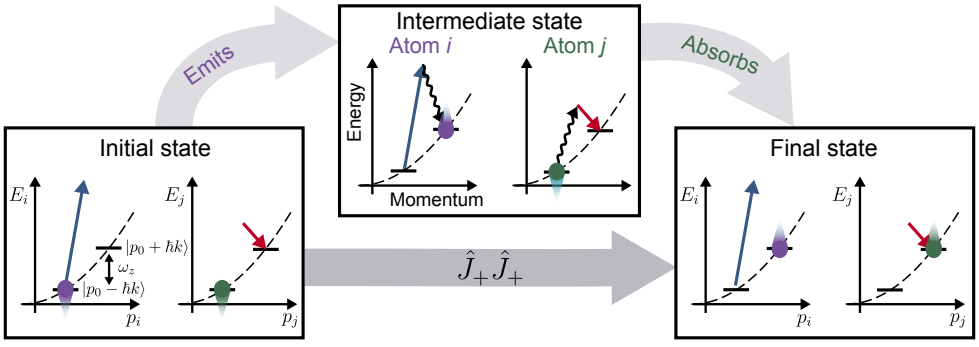

Figure 6.3: Representation of the emission/absorption processes described in (A) but depicted in terms of the atomic energy versus momentum for atoms i and j. The reverse process is also allowed, giving rise to a collective lowering operator described by $\hat{J}_-\hat{J}_-$.

The key insight is that different combinations of the dressing lasers and their atom-induced sideband tones will induce different virtual four-photon processes which will manifest as all-to-all exchange interactions $\hat{J}_+\hat{J}_-$ [12] and pair-raising $\hat{J}_+\hat{J}_+$ (lowering $\hat{J}_-\hat{J}_-$) processes as shown in Fig. 6.1 and 6.3. After adiabatically eliminating the cavity fields using second order perturbation theory (see [12][G]), we obtain an effective time-dependent atom-only Hamiltonian in an appropriate frame rotating at ω_z

$$\hat{H} = \chi_e \hat{J}_+\hat{J}_- + \left(\chi_p e^{i\delta t}\hat{J}_+\hat{J}_+ + \chi_p^* e^{-i\delta t}\hat{J}_-\hat{J}_-\right), \tag{6.1}$$

with the exchange and pair-raising/lowering couplings given by

$$\begin{aligned}\chi_e &= \left(\frac{g_0^2}{4\Delta_a}\right)^2 \left(\frac{|\alpha_1|^2}{\Delta_{\bar{c}}+\delta/2} + \frac{|\alpha_2|^2}{\Delta_{\bar{c}}-\delta/2}\right), \\ \chi_p &= \left(\frac{g_0^2}{4\Delta_a}\right)^2 \frac{|\alpha_1\alpha_2|e^{i\phi_{\text{int}}}}{2} \left(\frac{1}{\Delta_{\bar{c}}+\delta/2} + \frac{1}{\Delta_{\bar{c}}-\delta/2}\right).\end{aligned} \tag{6.2}$$

Here, $\Delta_{\bar{c}} = (\omega_2+\omega_1)/2 - \omega_c$ is the average detuning of the two dressing lasers from cavity resonance, typically set to be less than 1 MHz. $\delta = (\omega_2-\omega_1) - 2\omega_z$ is the detuning from four-photon resonance, $wg_0 = 2\pi \times 0.96$ MHz is the maximal atom-cavity Rabi coupling at an anti-node of the cavity mode, and $\phi_{\text{int}} = \arg(\alpha_2\alpha_1^*) - \phi_{\text{B}}$ is the differential phase between the two dressing laser tones relative to the phase of Bragg coupling ϕ_{B} which forms initial density grating. Collective cavity dissipation is dealt with separately.

We will focus on the resonant case $\delta = 0$ and $\phi_{\text{int}} = 0$, though we show example data in Fig. 6.4 that clearly exhibits a resonance in the interaction-induced dynamics at $\delta = 0$ as the pair raising/lowering processes are tuned into and out of resonance by tuning the dressing laser frequency difference. In the resonant case, the Hamiltonian of Eq. (6.1) reduces to:

$$\begin{aligned}\hat{H} &= (\chi_e+\chi_p)\hat{J}_x^2 + (\chi_e-\chi_p)\hat{J}_y^2 \\ &= \chi_e\hat{\mathbf{J}}\cdot\hat{\mathbf{J}} + \chi_p\left(\hat{J}_x^2 - \hat{J}_y^2\right) - \chi_e\hat{J}_z^2,\end{aligned} \tag{6.3}$$

where we defined the collective angular momentum operator, $\hat{\mathbf{J}} = \{\hat{J}_x, \hat{J}_y, \hat{J}_z\}$ and introduced the collective Heisenberg interaction $\hat{\mathbf{J}}\cdot\hat{\mathbf{J}}$. The latter acts as a constant for any eigenstate of the collective angular momentum operator $\hat{\mathbf{J}}\cdot\hat{\mathbf{J}}$, such as the collective states with eigenvalue $N/2(N/2+1)$. In

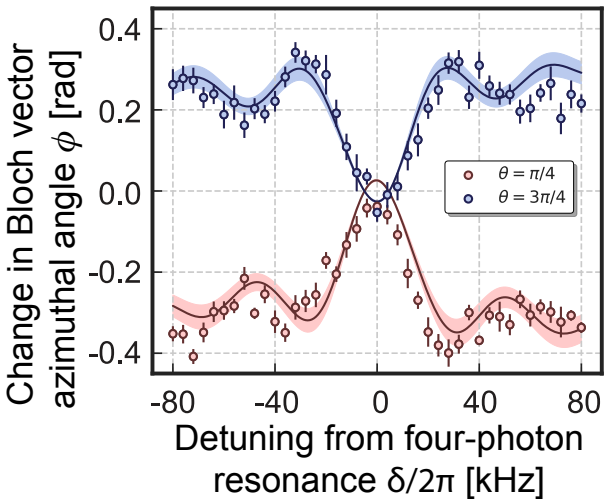

Figure 6.4: Observation of the four-photon resonance that generates pair raising and lowering processes. We scan the dressing laser frequency difference to vary the detuning δ. With equal dressing laser amplitudes corresponding to realizing the $\hat{J}_x^2$ Hamiltonian when $\delta = 0$, we see clear resonances in the observed change of the Bloch vector's azimuthal angle ϕ for a Bloch vector prepared near the south pole ($\theta = \pi/4$, red data points) and near the north pole ($\theta = 3\pi/4$, blue data points). All error bars reported are 1σ uncertainties. Simulation results are shown in solid lines with shaded area allowing for 5% uncertainty in interaction strength.

the presence of single particle inhomogeneities, this term opens a many-body gap that help promote spin locking which we explored before for the protection of coherences against dephasing [98, 12][G]. Here we instead focus on the fully collective dynamics and therefore without loss of generality we can add a generic $\chi_z \hat{\mathbf{J}} \cdot \hat{\mathbf{J}}$ term without affecting the dynamics. As such, in our system we are able to engineer dynamics governed by an XYZ Hamiltonian $\hat{H} = \chi_x \hat{J}_x^2 + \chi_y \hat{J}_y^2 + \chi_z \hat{J}_z^2$ with interaction strengths $\chi_x = (\chi_e + \chi_p + \chi_z)$ and $\chi_y = (\chi_e - \chi_p + \chi_z)$. The XYZ Hamiltonian is highly tunable by simply adjusting the relative power in the two applied dressing lasers since χ_e scales as $|\alpha_2|^2$, $|\alpha_1|^2$ and χ_p scales as $|\alpha_2 \alpha_1|$.

6.3 Four-photon spectroscopy

In Fig. 6.4, we have shown a spectroscopic result of the four-photon resonance. For this experiment, we prepare two different initial Bloch vectors to be $\pi/4$ above or below the equator with projections nominally along $\hat{y}$, as shown in Fig. 6.5.

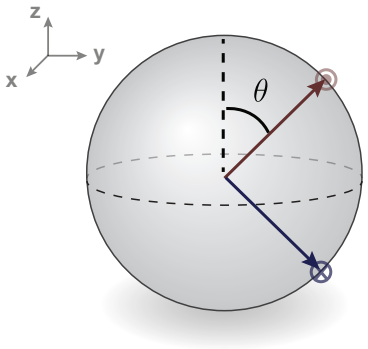

Figure 6.5: Initial states for four-photon spectroscopy.

When on resonance with $\delta = 0$, the ratio of the two dressing laser amplitudes is balanced to achieve an effective Hamiltonian in the form of $\hat{H} = \chi \hat{J}_x^2$, which preserve the azimuthal angle.

The four-photon detuning δ can be intuitively understood as inducing a time-dependent one-axis twisting interaction $\hat{H} = \chi \hat{J}_{\phi(t)}^2$ where the twisting axis rotates as $\hat{J}_{\phi(t)} = \cos(\delta t/2)\,\hat{J}_x + \sin(\delta t/2)\,\hat{J}_y$. With the four-photon detuning $\delta \gg \chi N$, the effective Hamiltonian recovers to the exchange interaction $\hat{H} = \chi\left(\hat{\mathbf{J}}\cdot\hat{\mathbf{J}} - \hat{J}_z^2\right)$ which induces finite changes in the azimuthal angle of the initial Bloch vectors with the signs depending on the initial projection along $\hat{z}$.

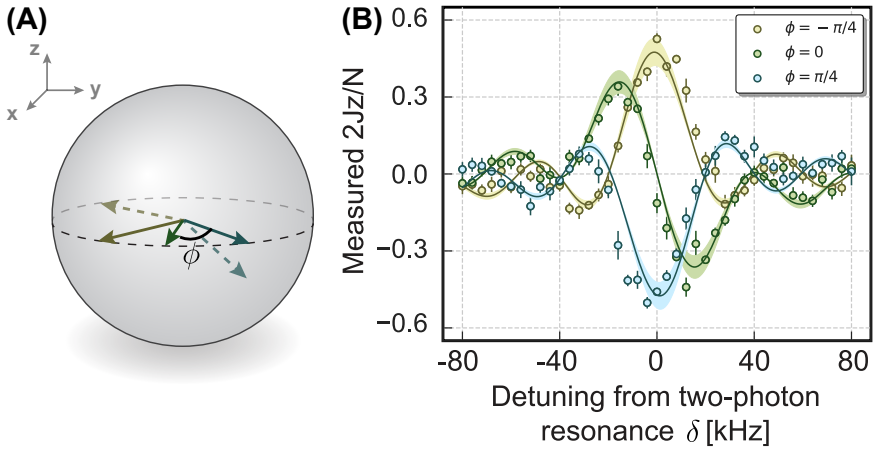

Figure 6.6: Four-photon spectroscopy with initial states on the equator. (A) The initial Bloch vectors. (B) Interaction induced change in J_z as a function of the four-photon detuning.

With a different set of initial states, the four-photon resonance can also be witnessed by the change in polar angle or equivalently spin projection J_z. In this experiment, we prepare initial

Bloch vectors on the equator but with different azimuthal angle $\phi = -\pi/4, 0$ and $+\pi/4$ as shown in Fig. 6.6. When on resonance with $\delta = 0$, the effective Hamiltonian $\hat{H} = \chi \hat{J}_x^2$ causes a positive/negative change in J_z for initial states with $\phi = \pm\pi/4$. While for $\phi = 0$, the initial Bloch vector is along $\hat{J}_x$ which commutes with the Hamiltonian and thus experience no change in J_z. With $\delta \gg \chi N$, J_z in conserved under the effective exchange interaction $\hat{H} = \chi \left(\hat{\mathbf{J}} \cdot \hat{\mathbf{J}} - \hat{J}_z \right)$ for all three initials states.

6.4 Mean-field dynamics

At the mean-field level, we can define the Bloch vector $\mathbf{J} \equiv (J_x, J_y, J_z) = (\langle \hat{J}_x \rangle, \langle \hat{J}_y \rangle, \langle \hat{J}_z \rangle)$ and approximate the Hamiltonian as $\hat{H} = \mathbf{B}(\mathbf{J}) \cdot \hat{\mathbf{J}}$. In this way, the collective dynamics are driven by a self-generated effective magnetic field $\mathbf{B}(\mathbf{J}) = (2\chi_x J_x, 2\chi_y J_y, 2\chi_z J_z)$ which depends on the instantaneous collective spin projections. We can derive the equations of motion of the collective Bloch vector, from Eq. (6.3), which simplify to a nonlinear torque equation $d\mathbf{J}/dt = \mathbf{B}(\mathbf{J}) \times \mathbf{J} \equiv \mathbf{T}(\mathbf{J})$. One can identify the fixed points $\mathbf{J}_{\text{fix}}$ as the points where $\mathbf{T}(\mathbf{J}_{\text{fix}}) = 0$.

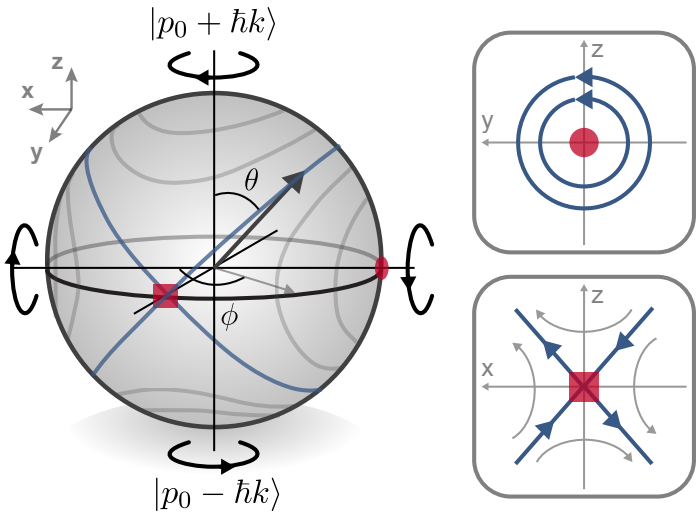

Figure 6.7: Dynamics induced by two-axis counter twisting in the form of a Hamiltonian $\hat{J}_x^2 - \hat{J}_z^2$ is represented on a Bloch sphere with north and south poles defined by $|p_0 \pm \hbar k\rangle$. Top right shows the local circular flows around the stable point at $-\hat{x}$. The local flows for unstable saddle points at $\hat{y}$ with exponential squeezing and anti-squeezing along $\hat{x} \pm \hat{z}$ are shown in bottom right.

To understand the dynamics near the fixed points, it is useful to follow a standard stability analysis by diagonalizing the Jacobian matrix $M(\mathbf{J}) = \partial\mathbf{T}/\partial\mathbf{J}|_{\mathbf{J}=\mathbf{J}_{\text{fix}}}$. The local motion near these fixed points is illustrated in Fig. 6.7 (right). We use red circles for stable points with purely imaginary eigenvalues. The Bloch vector evolves on stable closed orbits indicated by the blue circular traces. The red squares are used to denote unstable saddle points with real eigenvalues with opposite signs. The unstable saddle points are labelled by the red squares. The eigenvalues of the Jacobian matrix at the saddle points are real but with opposite signs. In Fig. 6.7(bottom right), the dynamics show exponential divergence from the origin (indicated by outward blue arrows) along $\hat{x}+\hat{z}$, corresponding to the positive eigenvalue [180]. The negative eigenvalues are indicated by the convergence towards the origin (inward blue arrows) along $\hat{x}-\hat{z}$.

6.5 Dynamics on the Bloch sphere

In the experiment, we probe the local dynamics induced by the above Hamiltonian with various values of χ_e and χ_p. To do this, we vary the phase and duration of the Bragg pulse to prepare an initial pseudo-spin coherent state $\mathbf{J}_i$. Before the atomic wave packets separate, we then apply the interaction for a short time Δt satisfying $\chi N \Delta t \ll 1$ and measure the change in azimuthal angle $d\phi$ and polar angle $d\theta$ to obtain the final Bloch vector $\mathbf{J}_f$ after the interaction. This is achieved by repeating the experiment and applying additional appropriate rotations before measuring populations in the two momentum states. The local flow vector is then determined by the torque $\mathbf{T}(\mathbf{J}_i) \approx \Delta\mathbf{J}/\Delta t = (\mathbf{J}_f - \mathbf{J}_i)/\Delta t$.

In Fig. 6.8**(A)**, we show the predicted flow vectors $\mathbf{T}(\mathbf{J}_i)$ on the Bloch sphere for three example Hamiltonians of interest. Different Hamiltonians are obtained by changing the ratio of the dressing laser amplitudes $|\alpha_2/\alpha_1| = 0, 0.17$, and 1.0.

We show the measured flow vector $\mathbf{T}(\mathbf{J}_i)$ in Fig. 6.8**(B)** with each row aligned to the corresponding example presented in Fig. 6.8**(A)**. In each case, the flow vector start at $\mathbf{J}_i$ and end at $\mathbf{J}_f$. The left and right panels are polar plots (radial coordinate linear in polar angle) of the dynamics on the south/north hemisphere looking from the north poles of the Bloch sphere. The middle panels

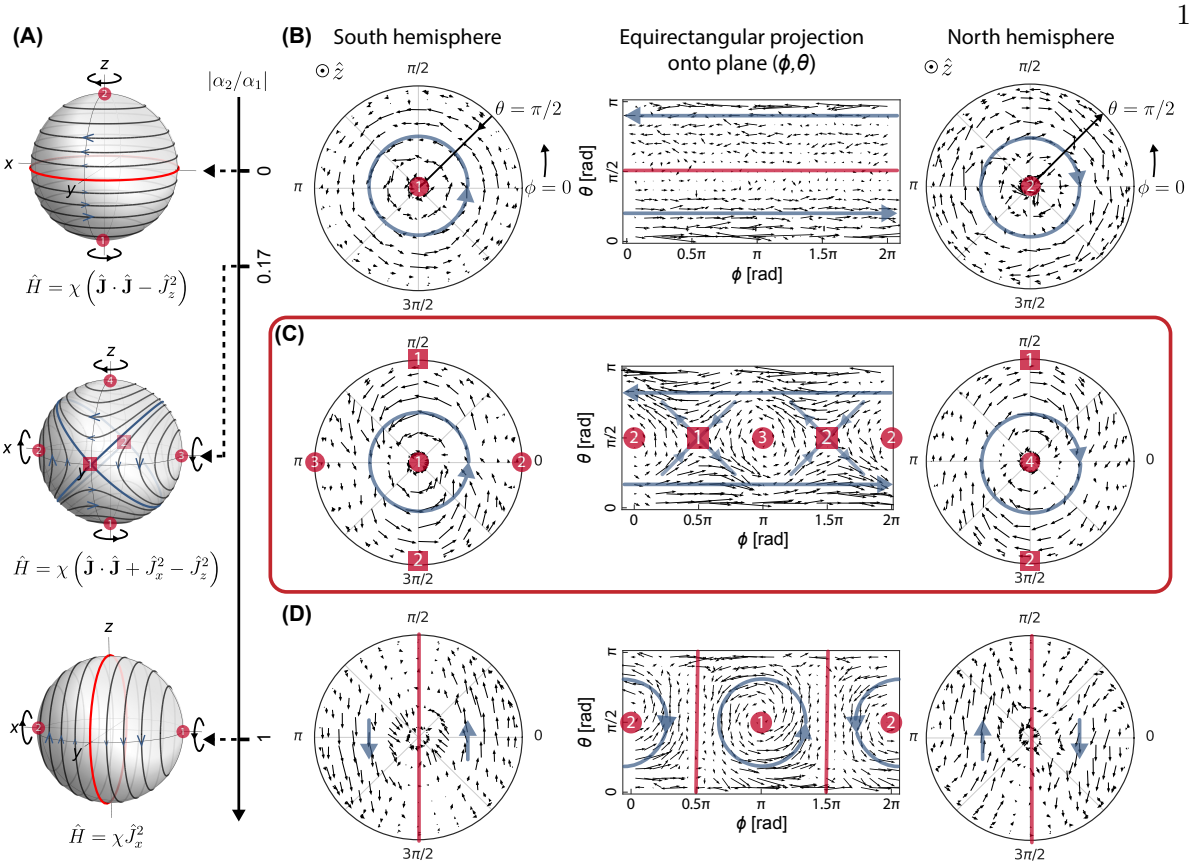

Figure 6.8: **Evolution under different Hamiltonians. (A)** Setting different amplitude ratios between the two dressing tones $|\alpha_2/\alpha_1|$ gives rise to different XYZ Hamiltonians, with specific examples shown here including one-axis twisting $\hat{\mathbf{J}}\cdot\hat{\mathbf{J}} - \hat{J}_z^2$, two-axis counter twisting $\hat{\mathbf{J}}\cdot\hat{\mathbf{J}} + \hat{J}_x^2 - \hat{J}_z^2$ and one-axis twisting $\hat{J}_x^2$. The experimentally observed dynamics are shown in corresponding rows in **(B, C, D)**, where the tail of each vector indicates the initial position of the Bloch vector $\mathbf{J}_i$ on the Bloch sphere, and the arrow indicates the displacement $\mathbf{T}$ after a brief period of evolution under the corresponding Hamiltonians. The left (right) panels are for initial Bloch vectors on the south (north) hemisphere. The polar angle θ of the initial Bloch vector linearly increase from $\pi/2$ at the rim to π in the middle for the left plot, whereas θ decrease from $\pi/2$ at the rim to 0 in the middle for the right plot. The middle panels are equirectangular projections. In each case, the qualitatively observed stable fixed points are marked with numbered red circles, and the unstable fixed points are marked with numbered red squares. The blue lines are shown to indicate directions of observed flow. The red lines indicate lines where the dynamics are zero and separate regions of opposite flows on the Bloch sphere.

are equirectangular projections to show dynamics near the equator. From these vector maps, we can make qualitative comparisons based on the geometry of the flow. For both theoretical and experimental results, the stable fixed points and unstable saddle points labeled as numbered red circles and squares respectively [180, 181].

In the first row of Fig. 6.8, we consider the simplest case with $\chi_p = 0$. This is achieved by turning off one of the dressing lasers ($|\alpha_2/\alpha_1| = 0$), leading to the Hamiltonian $\hat{H} = \chi_e \left(\hat{\mathbf{J}} \cdot \hat{\mathbf{J}} - \hat{J}_z^2\right)$. This Hamiltonian, referred to as the OAT Hamiltonian [16], maintains U(1) symmetry, thereby conserving J_z. At the mean-field level, it features a constant effective magnetic field along the $\hat{z}$ direction, which results in the rotation of the collective Bloch vector about the $\hat{z}$-axis at a uniform constant angular frequency,$-2\chi_e J_z$. As expected, we observe two stable fixed points (red 1 and 2 circles), and a reversal of the circulation across the equator (i.e. $J_z = 0$) where there are no dynamics (red line). This J_z dependent circulation leads to shearing of the quantum noise in the orientation of a Bloch vector on the Bloch sphere, a semiclassical explanation for how OAT dynamics generate spin-squeezed states [16, 11]. We note that while the term $\hat{\mathbf{J}} \cdot \hat{\mathbf{J}}$ is trivial for our current observations at short times, at longer times, when inhomogeneities in our system manifest, it can lead to important dynamical effects as shown in Ref. [12][G].

Next, we consider the last row in Fig. 6.8 with $\chi_p = \chi_e$. This is achieved by using equal dressing laser amplitudes $|\alpha_2/\alpha_1| = 1$. Here, the Hamiltonian is $\hat{H} = 2\chi_e \hat{J}_x^2$, leading to OAT dynamics along the $\hat{x}$ direction. The corresponding dynamics are induced at the mean-field level by a magnetic field along $\hat{x}$ that preserves J_x and induces a rotation about $\hat{x}$ with constant angular frequency $4\chi_e J_x$. It is noteworthy that the interaction strength here is twice that of the $\hat{J}_z^2$ case, attributed to the use of two dressing laser tones. The data qualitatively shows two stable fixed points along $\hat{x}$ labeled by red circles 1 and 2, and a reversal of the sign of circulation across J_x highlighted by the red lines.

Finally, we come to the case that achieves TACT, as shown in the middle row of Fig. 6.8. In this case, the ratio of dressing lasers amplitudes is set to be $|\alpha_2/\alpha_1| = \left(\sqrt{2}-1\right) / \left(\sqrt{2}+1\right) \approx 0.17$, which produces $\chi_e = 3\chi_p$. Starting with a single dressing tone α_1, by introducing a second dressing tone with tiny amount of power ($|\alpha_2/\alpha_1|^2 \approx 3\%$), the Hamiltonian become $\hat{H} = 2\chi_p \left(2\hat{J}_x^2 + \hat{J}_y^2\right) = 2\chi_p \left(\hat{\mathbf{J}} \cdot \hat{\mathbf{J}} + \hat{J}_x^2 - \hat{J}_z^2\right)$.

The corresponding mean-field magnetic field is now $\mathbf{B}(\mathbf{J}) = 4\chi_p \left(J_x, 0, -J_z\right)$, where we have again ignored the Heisenberg term since we will only consider dynamics at constant Bloch vector

length. The theoretical flow line for the dynamics is depicted in Fig. 6.8**(A)** (middle), showing four stable fixed points along $\pm\hat{x}$ and $\pm\hat{z}$, as well as two unstable fixed points along $\pm\hat{y}$ connected by great circles inclined at $\pm\pi/4$ to the equatorial plane (red circles). In comparison to OAT, there exist two twisting fields thus only the two points intersected by two blue circles with $J_x = J_z = 0$, exhibit the maximum shearing dynamics, which serve as the unstable saddle points.

We experimentally explore the flow lines. In the left and right panels, the observed stable fixed points are labeled with red circles numbered 1 to 4. The circulations of the flow lines are opposite for stable fixed points on opposite sides of the Bloch sphere. In the middle panel, we observe two unstable points labeled with red squared 1 and 2 in Fig. 6.8**(C)**. The two unstable fixed points have flow lines that either diverge from them (blue arrows outward) or converge towards them (blue arrows inward), with the two flows orthogonal to each other (see the discussion below). These findings constitute the first direct observation of genuine TACT dynamics. We note that for a particular set of parameters of the LMG Hamiltonian, for example when $\hat{H} = \chi\hat{J}_z^2 + \delta\hat{J}_y$ with $\delta \sim \chi N$, and when the Bloch vector initially points along the $\hat{y}$ direction [180, 181], the flow lines can resemble the ones close to a saddle point of the TACT model. However, the instability is restricted to this single point, in contrast to the full TACT which features two independent unstable points.

For a quantitative comparison, we examine the dynamics near the saddle point $\mathbf{J}_{\text{sad}}$ along the $\hat{y}$ axis on the Bloch sphere. In Fig. 6.9, we map the displacement $\mathbf{T}(\mathbf{J}_i)$ as a function of the initial Bloch vector orientation $\mathbf{J}_i = \mathbf{J}_{\text{sad}} + d\mathbf{J}_i$. We scan the initial Bloch vector angles θ_i and ϕ_i over a range $\pm\pi/12$ centered about $\pi/2$ (i.e. about $\hat{y}$) with discrete points sampled using a detailed 11×11 grid. The mean-field equations of motion for the two orthogonal directions $\hat{n}_\pm = (\hat{x} \pm \hat{z})/\sqrt{2}$ are:

$$\begin{aligned} \frac{d}{dt}(J_x + J_z) &= 4\chi_p J_y (J_x + J_z) \\ \frac{d}{dt}(J_x - J_z) &= -4\chi_p J_y (J_x - J_z). \end{aligned} \tag{6.4}$$

For the small range of angles around the $\hat{y}$ axis sampled in these measurements, one can assume $J_y \approx N/2$, and therefore find out that the displacement's time derivative increases linearly with

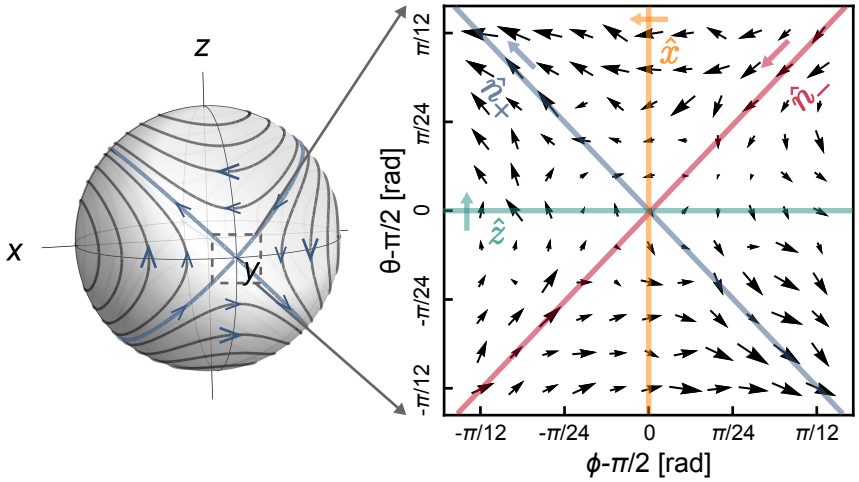

Figure 6.9: **Dynamics near saddle points.** Measured local flow vector map around the saddle point of the TACT dynamics.

the displacement itself, indicating dynamics that change exponentially over time.

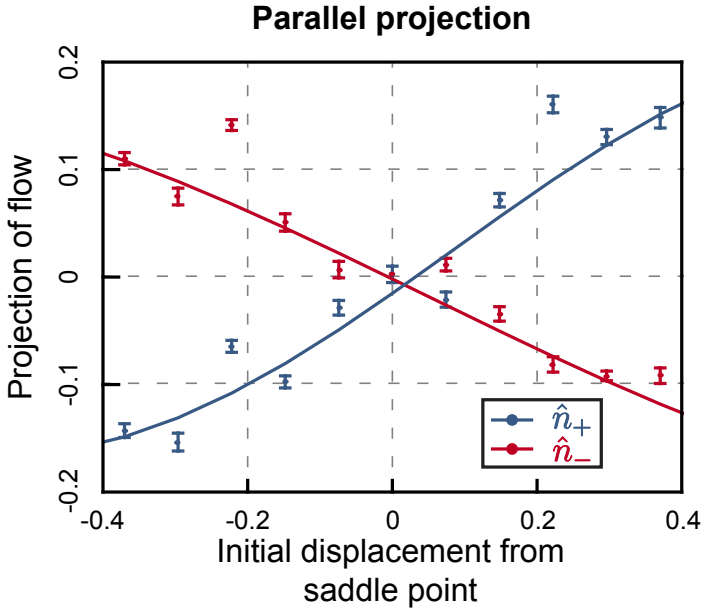

Figure 6.10: Blue and red points are parallel projections of the local flow vector onto the $\hat{n}_\pm$ axis $\Delta\mathbf{J}\cdot\hat{n}_\pm/(N/2)$ as a function of initial displacement $d\mathbf{J}_i\cdot\hat{n}_\pm/(N/2)$ from the saddle point along the blue and red lines in Fig. 6.9. Blue and red solid lines are simulation results. The linear dependence shows exponentially growing / shrinking dynamics along the squeezing / anti-squeezing axes.

We first focus on the data points along the two directions $\hat{n}_\pm$ (depicted by blue and red

lines in Fig. 6.9) and compute the parallel projection of the flow $\Delta\mathbf{J} \cdot \hat{n}_{\pm}/(N/2)$ as a function of initial displacement from the saddle point $d\mathbf{J}_i \cdot \hat{n}_{\pm}/(N/2)$, as shown in Fig. 6.10. The observed linear relationship between the projection of the flow and initial displacement matches well with the prediction from the simulation results (solid lines) which go beyond the linear approximation by solving the non-linear equations (Eq. (6.4)). The small differences observed between the $\Delta\mathbf{J} \cdot \hat{n}_{\pm}/(N/2)$ slopes stem from the finite duration of the interaction, which extends the dynamics beyond the linear response regime.

The unstable dynamics explain why an initial circular distribution centered around the saddle point shears as a function of time by squeezing (anti-squeezing) along the $\hat{n}_-$ ($\hat{n}_+$) direction at a rate exponentially faster than the linear growth seen in OAT. This combined with the global (over the full Bloch sphere) dynamical behavior allows the TACT to directly approach the fundamental Heisenberg limit on phase estimation [16, 180].

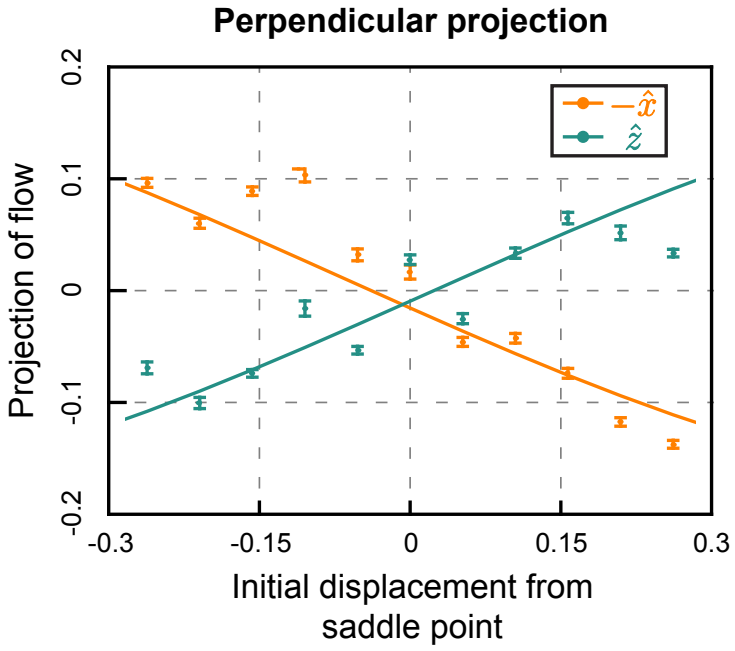

Figure 6.11: Green and orange points are the perpendicular projection of the local flow vector as a function of initial angular displacement from the saddle point along the green and orange lines in **(A)** ($\hat{n} = \hat{x}$ and $\hat{z}$) onto $\hat{n} \times \hat{y} = \hat{z}$ and $-\hat{x}$ axis ($\Delta\mathbf{J}_z$ and $-\Delta\mathbf{J}_x$). Orange and green solid lines are simulation results.

In Fig. 6.11, we analyze the orthogonal projection of interaction-induced flows, especially focus on the data points that initially displaced from the saddle point along $\hat{n} = \hat{x}$ and $\hat{z}$ axes (depicted by green and orange lines in Fig. 6.9), and calculate their projections along the $\hat{n} \times \hat{y} = \hat{z}$ and $-\hat{x}$ axes ($\Delta\mathbf{J}_z$ and $-\Delta\mathbf{J}_x$), respectively. The dynamics can be explained by noticing that when the Bloch vector is initially prepared in the y-z plane, the effective mean-field magnetic field is along the $\hat{z}$ axis with a magnitude of $-4\chi_p J_z$. Conversely, when prepared in the y-x plane, the field is along the $\hat{x}$ axis, with an amplitude of $4\chi_p J_x$. Thus one expects these two perpendicular displacements to grow linearly in magnitude with initial Bloch vector displacement, as we observed in Fig. 6.11.

6.6 Two-axis counter-twisting with unstable points at north and south poles

The original TACT Hamiltonian, as proposed by Kitagawa and Ueda [16], is defined as

$$\hat{H}' = \chi \left(\hat{J}_+^2 + \hat{J}_-^2 \right) = 2\chi \left(\hat{J}_x^2 - \hat{J}_y^2 \right), \tag{6.5}$$

with the theoretical flow lines shown in Fig. 6.12. This Hamiltonian bears resemblance to the previously discussed TACT, with an additional $\pi/2$ rotation around the y-axis. It is characterized by unstable points at the north and south poles of the Bloch sphere, along with four stable points located on the equator at $\pm\hat{x}$ and $\pm\hat{y}$.

In our setup, it seems to be impossible to choose the parameters canceling χ_e in Eq. (6.2) at first glance. However, this can be achieved by placing the two detuned dressing lasers tones on the same side of the cavity resonance as shown in Fig. 6.12. In this configuration, the previously ignored lower modulation sideband of the red dressing laser becomes significant. This sideband introduces an exchange interaction with the opposite sign of the other generated exchange interactions. By carefully selecting the detuning and the amplitude ratio of the two dressing laser tones, we can achieve a configuration where $\chi_e = 0$, effectively only leaving the χ_p term. $\hat{H}'$ offers the advantage of possibly being less sensitive to the presence of superradiance or collective decay for future squeezing generation in our system.

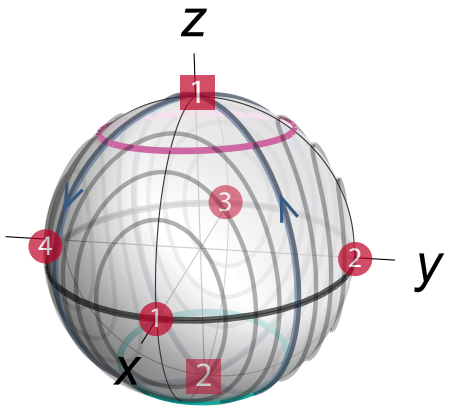

Figure 6.12: **Two-axis counter-twisting with unstable points at north/south poles.** Dynamics shown as flows on the Bloch sphere with three characteristic circles (purple: $\theta_i = 0.9\pi$, black: $\theta_i = 0.5\pi$ and green: $\theta_i = 0.1\pi$) highlighted.

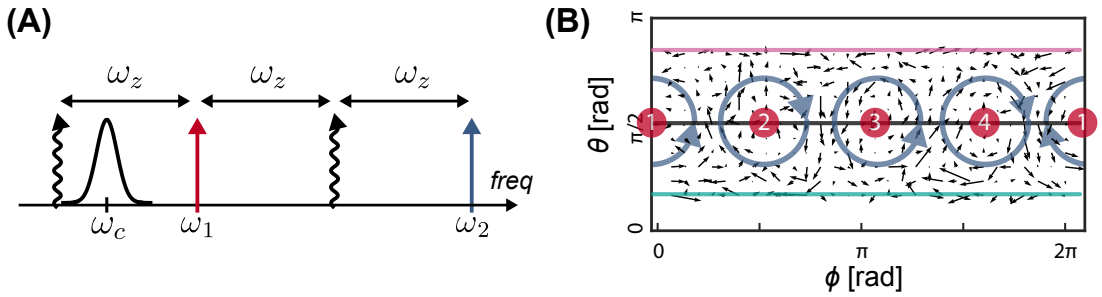

Figure 6.13: **(A)**Frequency diagram with both dressing lasers positioned on the same side relative to the cavity resonance. **(B)**The equirectangular projection of the resulting dynamics (bottom).

In Fig. 6.13**(B)**, we show the measured flow lines for $\hat{H}'$ in the equirectangular projection. One can clearly identify four stable fixed points on the equator as expected.

To have a better intuition of the dynamics, instead of focusing on the dynamics on the whole Bloch sphere, we take a few cuts with initial Bloch vectors $\mathbf{J}_i$ prepared with $\theta_i = 0.1\pi, 0.5\pi$ and 0.9π and study the dynamics separately. For the initial Bloch vectors prepared on the two circles with $\theta_i = 0.1\pi$ and 0.9π (green and purple in Fig. 6.12 and Fig. 6.14 **(A)** and **(B)** near the north/south poles, the distribution of the states after the interaction $\mathbf{J}_f$ is plotted in Fig. 6.14 **(A)**

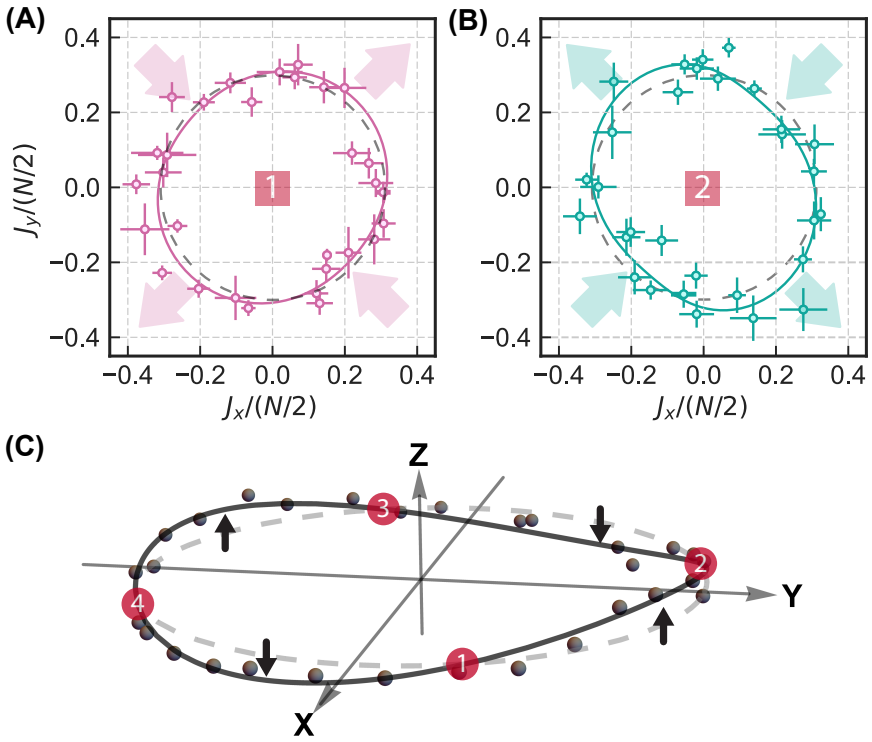

Figure 6.14: **Deformation of initial state distributions.** **(A)**, **(B)** and **(C)** are the distributions of the states after the interaction with the prepared initial state $\theta_i = 0.1\pi$ (green circle), 0.9π (purple circle) and 0.5π (black circle). The deviations from the initial state distribution (gray dashed circles) are shown by the colored arrows.

and **(B)**(solid lines with fitted curves). The elliptical distributions with major axis orthogonal to each other explicitly show the squeezing and anti-squeezing axis near the north and south poles in this small displacement limit. In Fig. 6.14 **(C)**, the initial Bloch vector is prepared on the equator with different azimuthal angles (grey dashed line) and we plot $\mathbf{J}_f$ (black dot). The four zero crossings correspond to the four stable points on the equator. Between the stable points, the observed final states are deflected alternately above or below the equator as expected.

6.7 Conclusion

Here we have demonstrated the flexibility of our optical cavity simulator to engineer tunable XYZ Hamiltonians using two selected momentum states, without the need for Floquet engineering which in some cases might be challenging to allow access beyond mean-field dynamics in large many-

body systems due to amplitude and phase noise on the Floquet control fields [182][G]. The pair-raising/lowering processes are verified to be present for the first time by the resonant spectroscopic signal when the detuning δ is scanned as well as the direct cancellation of the exchange interactions that yielded dynamics of the Hamiltonian $\hat{H}' = \chi\left(\hat{J}_+^2 + \hat{J}_-^2\right)$. By combining the correct relative balance of exchange and pair-raising/lowering contributions, we observed TACT dynamics for the first time.

While so far our focus has been on the characterization of the Hamiltonian by probing the short-time dynamics, extension to longer times can open untapped opportunities for quantum simulation and metrology. For example, by using an implementation where two dressing lasers are used to generate one-axis twisting dynamics, one should be able to balance the collective dissipation generated by the absorbed and emitted photons facilitating the emergence of beyond mean-field effects and entanglement generation.

Furthermore, while here we focused on only two momentum states as a first step, by combining them with actual internal states of the atoms or by adding more selected momentum states and dressing tones one should be able to engineer a toolbox for quantum state engineering, similar to what has been done with momentum states in Bose-Einstein condensate [130, 131, 183]. In our case however, in addition to the internal and external level control that tunes the synthetic dimensions, we can further enjoy the rich opportunities offered by the tunable cavity-mediated interactions to engineer phenomena ranging from superfluidity and supersolidity [102, 184, 185, 103] to dynamical gauge fields and non-trivial topological behaviors [186, 93, 151, 138, 150].

Chapter 7

Conclusion and outlook

In this thesis, I have discussed how a high finesse cavity can be used to measure, bind together and introduce interaction between atoms in superpositions of momentum states. Specifically, the matter-wave-cavity coupled system has demonstrated an entangled matter-wave interferometer, a novel collective recoil mechanism and a new way for simulating XYZ model. Not only can we entangle different momentum state using different spins, we can now also directly introduce tunable interactions between momentum states with the same spin label.

In terms of the performance of the matter-wave interferometer, we are able to achieve a resolution of $\Delta g/g = 10^{-5} - 10^{-6}$ with about 1000 atoms and a separation period of few ms. Although not comparable with state-of-the-art matter wave interferometer, it's an exciting platform with many possible prospects. In this chapter, I will give a brief overview on some future directions, the associating technical challenges and what might be the possible solutions.

7.1 Direct entanglement generation between momentum states

One missing opportunity for my PhD work is the direct entanglement generation between the momentum states. With the momentum-exchange interaction, there is a clear path towards squeezing using the one-axis-twisting dynamics. However, we are limited to above SQL due to a few technical issues.

(1) Finite laser linewidth as discussed in Chapter 5 and Chapter 6. The kHz linewidth laser we use to drive interactions is also inducing noisy rotations between the two momentum

states and thus spoils the squeezing. In a simple experiment, we prepare the initial state on the equator of the Bloch sphere, scan the dressing laser power applied at the cavity, and measure the excess noise on the population difference induced by the dressing laser. The extra noise quickly increases above few times of SQL, faster as compared to squeezing dynamics. This is one of the key reasons why did we not observe entanglement. To suppress this effect, we either need to increase the collective cooperativity (NC) of the system, such that the twisting dynamics is fasting than the introduced noise, or to narrow the dressing laser more, with the critical reduction of phase noise required for phase noise components at offsets from carrier $\omega_z = 2\pi \times 500$ kHz. In collaboration with Blumenthal's group from UCSB, we believe that we can significantly reduce the phase noise at 500 kHz offset from carrier by one to two orders of magnitude [187]. Given the relatively large offset from carrier, we also believe that we can improve our system using more traditional filter cavity to reduce the relevant phase noise components.

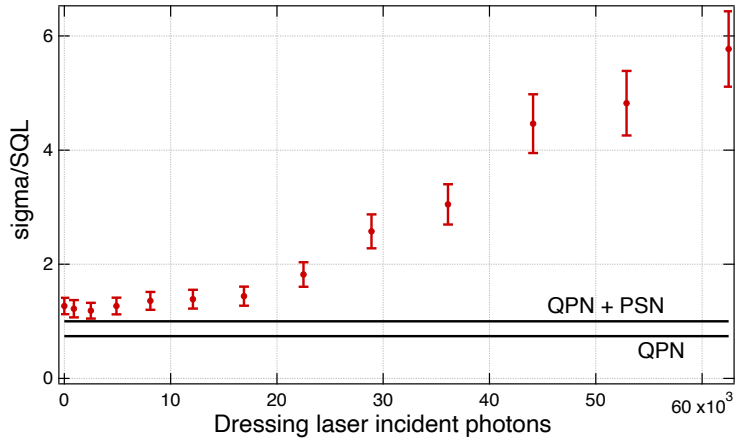

Figure 7.1: Excess noise in the measured spin projection J_z induced by dressing laser. The two black lines correspond to quantum projection noise (QPN) for the amount of atoms used in the experiments, and the combined noise of QPN and photon-shot noise (PSN) related to the detection processes.

(2) Secondly, the strong free-space scattering due to the finite detuning of the dressing/Bragg laser reduce the interferometer contrast significantly. In order to satisfy the phase matching

condition, the same laser is used for driving Bragg rotation and interactions. At the moment it is only 500 MHz detuned from the atomic transition, such that every Bragg π-pulse causes 10% loss in contrast. The atomic loss from the scattering leads to a reduced contrast of the interferometer and washes out the squeezing if any. This can be fixed by simply detuning the cavity and dressing laser further away from the atomic transition, however, at the cost of increased sensitivity to the laser phase noise, which in terms also requires a better laser with lower phase noise at ≈ 500 kHz offset frequency.

(3) Lastly, finite efficiency for transferring atomic population for the readout also reduces the observe metrological gain. Equivalently, the atomic loss due to the state transfer leads to a reduced size in signal and could therefore wash out the squeezing if any. In the experiment, for enhancing the interaction between momentum states with larger Clebsh-Gordon coefficients, the atomic internal state is first transferred to $|F = 2, m_F = 2\rangle$ to utilize the cycling transition $|F = 2, m_F = 2\rangle \rightarrow |F' = 3, m'_F = 3\rangle$. However the efficiency of the current readout process is limited by the complex combination of microwave rotations and Raman rotations, leading to an extra loss of atoms. Microwave rapid adiabatic passage may be employed in the future to improve the efficiency. It may also be possible to simply perform the velocity-selective readout and measurement using the F=1, mF=1 to F=2,mF=2 if inhomogeneous broadening and time dependent variation of the micrwave transition frequency can be made smaller than 5 kHz.

7.2 Squeezing with balanced dissipation

Squeezing with unitary evolution (OAT) and quantum measurement (QND) have been realized in many systems. There are recent proposals for squeezing generation with engineered dissipation[188, 189, 190]. One example is to drive balanced superradiance processes (J_- and J_+). Specifically for our experiment, one can apply two laser tones at $\pm\omega_z$ away from the dressed cavity resonance to purposefully induce balanced superradiance between the two momentum states,

as shown in Fig. 7.2. Theory has predicted that the steady state shows appreciable amount of squeezing (> 7 dB) even for low atom number (700, as in our current setup.)

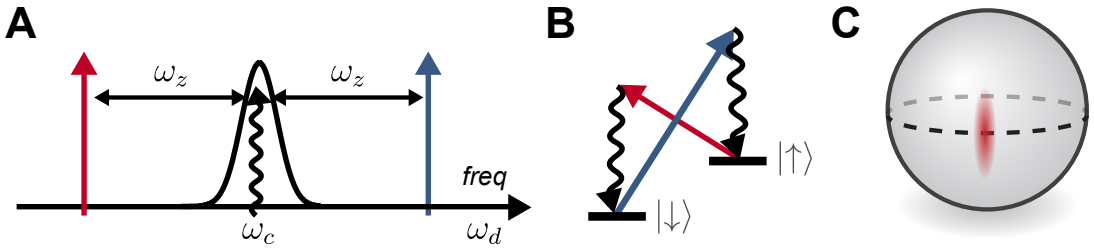

Figure 7.2: **Generating squeezing with dissipation. (A)** Applying two dressing laser tones at $\pm\omega_z$ from the cavity resonance can induce the balanced dissipation processes $\hat{J}_-$ and $\hat{J}_+$ as shown in **(B)**. As a result, the steady state is a squeezed state with squeezing on the phase quadrature as shown in **(C)**.

The challenge here is how well balanced can we achieve for the two superradiance processes. Aside from the classical noise for the laser power at the two frequencies, a key problem here is the fluctuating dressed cavity resonance. In other words, the atom number fluctuation could leads to the dressed cavity resonance fluctuate from shot to shot, such that it is hard to keep the two dressing laser tones equally detuned from the cavity resonance. One way to circumvent this issue is to detune the cavity resonance much further away from the atomic transition to reduce the cavity frequency shift induced by the presence of the atoms. This will again require that we work to narrow the dressing lasers to avoid making the noise of the first issue greater.

7.3 Continuous quantum phase measurement

Quantum sensing relies on measuring the accumulated phase between the two levels. The classic paradigm for phase measurement is the Ramsey sequence, because population measurement is more viable as compared to phase measurement. However, the finite pulse lengths and phase accumulation time reduce the measurement bandwidth. It would be a big win to directly measure the quantum phase.

In collaboration with our lab, Athreya from Holland's group proposed a new approach for performing phase measurement[153]. This idea is directly related to the balanced dissipation pro-

cesses as described above. In this experiment, in stead of only applying photons at the cavity, we also need to collect the photons (black squiggly line in Fig. 7.2) coming out of the cavity. A simple intuitive way to understand this measurement is that the photon created by the two superradiance processes carry the atomic information $\langle \hat{a} \rangle \propto \langle \hat{J}_+ \rangle$ and $\langle \hat{J}_- \rangle$. Because photons coming from the two processes are indistinguishable, the total output is determined by the sum $\langle \hat{J}_+ \rangle + \langle \hat{J}_- \rangle = \langle \hat{J}_x \rangle$, which carries the phase information.

With the complex level structure, it might be challenging to do this experiment with atomic hyperfine states. But with two momentum states, we could isolate a pure two-level system. The relative phase between momentum states is directly related to the phase of atomic density grating as discussed below.

7.4 QND measurement of the atomic density grating

OAT and QND essentially share the same Hamiltonian as discussed in Chapter. 2. Since we can induce OAT between two momentum states, one should be able to perform QND measurement on the momentum states as well. There are two different steps.

The first one is the atom number counting in a specific momentum state. For QND measurement of the spin state (rubidium hyperfine states), one need to tune the cavity resonance close to the transition between the excited state and one of the spin state. The QND measurement on momentum states is only proposed for the narrow linewidth transition in strontium[191]. This is however difficult for rubidium, due to the small energy difference between momentum state as compared to the excited state lifetime. A possible approach is to use an extra laser tones to dress an auxiliary spin state to realize an effective excited state with narrow and tunable linewidth, which allows one can probe one leg of the two-photon transition between the two momentum states. Or in other words, one can perform QND measurement of the two-photon transition to selectively measure the atoms number in a specific momentum state.

A step further will be the direct phase measurement between two momentum states. This is connected to the balanced superradiance idea or the XYZ interaction experiment. Again, one can

apply two dressing laser at the cavity driving two superradiance processes, the photons coming out of the cavity carry phase information between the two momentum states. Direct phase measurement can be performed by collecting and detecting the photon exiting the cavity. Combined with the wave packet binding mechanism, a continuous gravity measurement can be performed, akin to dropping a ruler and continuously reading the position while falling.

7.5 Going beyond two-body interactions

The momentum-exchange interaction and the XYZ models realized in this thesis are both two-body interactions involving pair of atoms. In other words, the associated Hamiltonian are quadratic in terms of pseudo-spin operators, including the one-axis twisting and two-axis counter-twisting dynamics. There are recent proposals on fast entanglement generations with three-body interaction[192], or more complex squeezing protocol for phonon states in trapped ion systems[193]. Engineering controllable all-to-all three-body interactions is challenging, however, this might be achievable for cavity-QED systems with six-photon processes as drawn below:

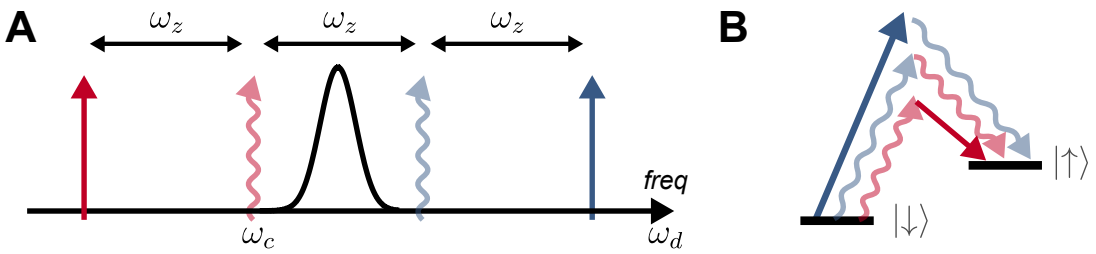

Figure 7.3: **Three-body interactions with six-photon processes. (A)** Frequency diagram with two dressing lasers separated by $3\omega_z$. **(B)** Six-photon process that raises three atoms from lower momentum state $|\downarrow\rangle$ to the higher momentum state$|\uparrow\rangle$.

By separating two dressing laser tones for $(3\omega_z)$, there exist a resonant six-photon process that promote three atoms into higher momentum states at once, and thus leads to a Hamiltonian $\hat{H}_{6ph} = \chi_{6ph}\left(\hat{J}_+^3 + \hat{J}_-^3\right)$. Bigger frequency separation might lead to even higher order processes. However, detailed calculation and analysis is still needed to verify the interaction strength is strong enough as compared to other dissipative processes (superradiance, free-space scattering, etc.) in

order to study these complex dynamics.

7.6 Simulating BEC-BCS cross-over with momentum qubits

In a recent work from the Sr experiment in our lab [9], dynamical phases of the BCS model are observed with the Higgs oscillation due to the spin-exchange interaction. With the momentum-exchange interaction, the dephasing process is more controlled and predictable such that one can simulate the BEC-BCS crossover by preparing initial state with different decoherence and observing the coherence oscillation under the momentum-exchange interaction.

Simulations have shown an obvious change in the time constants for the decay of oscillation with different initial states. The challenge here is to suppress superradiance process to allow for longer interaction time. One should be able to solve it by carefully balancing the dressing laser powers above and below the cavity resonances.

7.7 Summary

Apart from the future directions listed above, Zhijing Niu is now having rapid progress on suppressing Doppler shift on a narrow optical transition with momentum-exchange interactions realized between strontium atoms in a ring cavity. All these fun physics are realized by coupling matter waves to a high-finesse cavity. With this new approach for introducing interactions between wave packets, momentum states could potentially become an interesting qubit system with many new opportunities for quantum metrology and simulations.

Bibliography

[1] Particle control in a quantum world. `https://www.nobelprize.org/uploads/2018/06/popular-physicsprize2012.pdf`. Accessed: 2024-03-19.

[2] Louis De Broglie. Recherches sur la théorie des quanta. PhD thesis, Migration-université en cours d'affectation, 1924.

[3] Mark Kasevich and Steven Chu. Atomic interferometry using stimulated raman transitions. Phys. Rev. Lett., 67:181–184, Jul 1991.

[4] T L Gustavson, A Landragin, and M A Kasevich. Rotation sensing with a dual atom-interferometer sagnac gyroscope. Classical and Quantum Gravity, 17(12):2385–2398, jun 2000.

[5] Mahiro Abe, Philip Adamson, Marcel Borcean, Daniela Bortoletto, Kieran Bridges, Samuel P Carman, Swapan Chattopadhyay, Jonathon Coleman, Noah M Curfman, Kenneth DeRose, Tejas Deshpande, Savas Dimopoulos, Christopher J Foot, Josef C Frisch, Benjamin E Garber, Steve Geer, Valerie Gibson, Jonah Glick, Peter W Graham, Steve R Hahn, Roni Harnik, Leonie Hawkins, Sam Hindley, Jason M Hogan, Yijun Jiang, Mark A Kasevich, Ronald J Kellett, Mandy Kiburg, Tim Kovachy, Joseph D Lykken, John March-Russell, Jeremiah Mitchell, Martin Murphy, Megan Nantel, Lucy E Nobrega, Robert K Plunkett, Surjeet Rajendran, Jan Rudolph, Natasha Sachdeva, Murtaza Safdari, James K Santucci, Ariel G Schwartzman, Ian Shipsey, Hunter Swan, Linda R Valerio, Arvydas Vasonis, Yiping Wang, and Thomas Wilkason. Matter-wave atomic gradiometer interferometric sensor (MAGIS-100). Quantum Science and Technology, 6(4):044003, jul 2021.

[6] Yousef Abou El-Neaj, Cristiano Alpigiani, Sana Amairi-Pyka, Henrique Araújo, Antun Balaž, Angelo Bassi, Lars Bathe-Peters, Baptiste Battelier, Aleksandar Belić, Elliot Bentine, et al. Aedge: atomic experiment for dark matter and gravity exploration in space. EPJ Quantum Technology, 7(1):1–27, 2020.

[7] Ludwig Zehnder. Ein neuer interferenzrefraktor, 1891.

[8] Ludwig Mach. Ueber einen interferenzrefraktor. Zeitschrift für Instrumentenkunde, 12(3):89, 1892.

[9] Dylan J Young, Anjun Chu, Eric Yilun Song, Diego Barberena, David Wellnitz, Zhijing Niu, Vera M Schäfer, Robert J Lewis-Swan, Ana Maria Rey, and James K Thompson. Observing dynamical phases of bcs superconductors in a cavity qed simulator. Nature, 625(7996):679–684, 2024.

[10] Jiazhong Hu, Lei Feng, Zhendong Zhang, and Cheng Chin. Quantum simulation of unruh radiation. Nature Physics, 15(8):785–789, 2019.

[11] Graham P Greve, Chengyi Luo, Baochen Wu, and James K Thompson. Entanglement-enhanced matter-wave interferometry in a high-finesse cavity. Nature, 610(7932):472–477, 2022.

[12] Chengyi Luo, Haoqing Zhang, Vanessa PW Koh, John D Wilson, Anjun Chu, Murray J Holland, Ana Maria Rey, and James K Thompson. Cavity-mediated collective momentum-exchange interactions. arXiv preprint arXiv:2304.01411, 2023.

[13] Chengyi Luo, Haoqing Zhang, Anjun Chu, Chitose Maruko, Ana Maria Rey, and James K Thompson. Hamiltonian engineering of collective xyz spin models in an optical cavity: From one-axis twisting to two-axis counter twisting models. arXiv preprint arXiv:2402.19429, 2024.

[14] Vittorio Giovannetti, Seth Lloyd, and Lorenzo Maccone. Quantum metrology. Phys. Rev. Lett., 96:010401, Jan 2006.

[15] W. M. Itano, J. C. Bergquist, J. J. Bollinger, J. M. Gilligan, D. J. Heinzen, F. L. Moore, M. G. Raizen, and D. J. Wineland. Quantum projection noise: Population fluctuations in two-level systems. Phys. Rev. A, 47:3554–3570, May 1993.

[16] Masahiro Kitagawa and Masahito Ueda. Squeezed spin states. Phys. Rev. A, 47:5138–5143, Jun 1993.

[17] D. J. Wineland, J. J. Bollinger, W. M. Itano, and D. J. Heinzen. Squeezed atomic states and projection noise in spectroscopy. Phys. Rev. A, 50:67–88, Jul 1994.

[18] Alexander D. Cronin, Jörg Schmiedmayer, and David E. Pritchard. Optics and interferometry with atoms and molecules. Rev. Mod. Phys., 81:1051–1129, Jul 2009.

[19] Achim Peters, Keng Yeow Chung, and Steven Chu. Measurement of gravitational acceleration by dropping atoms. Nature, 400(6747):849–852, 1999.

[20] Richard H. Parker, Chenghui Yu, Weicheng Zhong, Brian Estey, and Holger Müller. Measurement of the fine-structure constant as a test of the standard model. Science, 360(6385):191–195, 2018.

[21] Léo Morel, Zhibin Yao, Pierre Cladé, and Saïda Guellati-Khélifa. Determination of the fine-structure constant with an accuracy of 81 parts per trillion. Nature, 588(7836):61–65, Dec 2020.

[22] Paul Hamilton, Matt Jaffe, Philipp Haslinger, Quinn Simmons, Holger Müller, and Justin Khoury. Atom-interferometry constraints on dark energy. Science, 349(6250):849–851, 2015.

[23] Chao Song, Kai Xu, Hekang Li, Yu-Ran Zhang, Xu Zhang, Wuxin Liu, Qiujiang Guo, Zhen Wang, Wenhui Ren, Jie Hao, et al. Generation of multicomponent atomic schrödinger cat states of up to 20 qubits. Science, 365(6453):574–577, 2019.

[24] Mi Lei, Rikuto Fukumori, Jake Rochman, Bihui Zhu, Manuel Endres, Joonhee Choi, and Andrei Faraon. Many-body cavity quantum electrodynamics with driven inhomogeneous emitters. Nature, pages 1–6, 2023.

[25] Onur Hosten, Nils J Engelsen, Rajiv Krishnakumar, and Mark A Kasevich. Measurement noise 100 times lower than the quantum-projection limit using entangled atoms. Nature, 529(7587):505, 2016.

[26] Kevin C. Cox, Graham P. Greve, Joshua M. Weiner, and James K. Thompson. Deterministic squeezed states with collective measurements and feedback. Phys. Rev. Lett., 116:093602, Mar 2016.

[27] J. Esteve, C. Gross, A. Weller, S. Giovanazzi, and M. K. Oberthaler. Squeezing and entanglement in a bose-einstein condensate. Nature, 455(7217):1216–1219, October 2008.

[28] C. Gross, T. Zibold, E. Nicklas, J. Estève, and M. K. Oberthaler. Nonlinear atom interferometer surpasses classical precision limit. Nature, 464(7292):1165–1169, April 2010.

[29] Max F Riedel, Pascal Böhi, Yun Li, Theodor W Hänsch, Alice Sinatra, and Philipp Treutlein. Atom-chip-based generation of entanglement for quantum metrology. Nature, 464(7292):1170–1173, 2010.

[30] Cass A Sackett, David Kielpinski, Brian E King, Christopher Langer, Volker Meyer, Christopher J Myatt, M Rowe, QA Turchette, Wayne M Itano, David J Wineland, et al. Experimental entanglement of four particles. Nature, 404(6775):256–259, 2000.

[31] Dietrich Leibfried, Emanuel Knill, Signe Seidelin, Joe Britton, R Brad Blakestad, John Chiaverini, David B Hume, Wayne M Itano, John D Jost, Christopher Langer, et al. Creation of a six-atom 'schrödinger cat' state. Nature, 438(7068):639–642, 2005.

[32] Thomas Monz, Philipp Schindler, Julio T. Barreiro, Michael Chwalla, Daniel Nigg, William A. Coish, Maximilian Harlander, Wolfgang Hänsel, Markus Hennrich, and Rainer Blatt. 14-qubit entanglement: Creation and coherence. Phys. Rev. Lett., 106:130506, Mar 2011.

[33] Ian D. Leroux, Monika H. Schleier-Smith, and Vladan Vuletić. Implementation of cavity squeezing of a collective atomic spin. Phys. Rev. Lett., 104:073602, Feb 2010.

[34] Monika H. Schleier-Smith, Ian D. Leroux, and Vladan Vuletić. States of an ensemble of two-level atoms with reduced quantum uncertainty. Phys. Rev. Lett., 104:073604, Feb 2010.

[35] A. Kuzmich, L. Mandel, and N. P. Bigelow. Generation of spin squeezing via continuous quantum nondemolition measurement. Phys. Rev. Lett., 85:1594–1597, Aug 2000.

[36] Daniel Steck. Rubidium 87 D Line Data. Jan 2003.

[37] Baochen Wu, Graham P Greve, Chengyi Luo, and James K Thompson. Site-dependent selection of atoms for homogeneous atom-cavity coupling. arXiv preprint arXiv:2104.01201, 2021.

[38] Zilong Chen, Justin G. Bohnet, Joshua M. Weiner, Kevin C. Cox, and James K. Thompson. Cavity-aided nondemolition measurements for atom counting and spin squeezing. Phys. Rev. A, 89:043837, Apr 2014.

[39] Diego Barberena, Anjun Chu, James K Thompson, and Ana Maria Rey. Trade-offs between unitary and measurement induced spin squeezing in cavity qed. arXiv preprint arXiv:2309.15353, 2023.

[40] Matthew A. Norcia, Julia R. K. Cline, and James K. Thompson. Role of atoms in atomic gravitational-wave detectors. Phys. Rev. A, 96:042118, Oct 2017.

[41] John E Tanner and Edward O Stejskal. Restricted self-diffusion of protons in colloidal systems by the pulsed-gradient, spin-echo method. The Journal of Chemical Physics, 49(4):1768–1777, 1968.

[42] Baochen Wu. Homogeneous Atom-Cavity Coupling for Quantum Metrology. PhD thesis, University of Colorado at Boulder, 2021.

[43] Graham P Greve. Entanglement-Enhanced Matter-Wave Interferometry. PhD thesis, University of Colorado at Boulder, 2021.

[44] J. Schoser, A. Batär, R. Löw, V. Schweikhard, A. Grabowski, Yu. B. Ovchinnikov, and T. Pfau. Intense source of cold rb atoms from a pure two-dimensional magneto-optical trap. Phys. Rev. A, 66:023410, Aug 2002.

[45] Ronald WP Drever, John L Hall, Frank V Kowalski, James Hough, GM Ford, AJ Munley, and Hywel Ward. Laser phase and frequency stabilization using an optical resonator. Applied Physics B, 31:97–105, 1983.

[46] DJ McCarron, SA King, and SL Cornish. Modulation transfer spectroscopy in atomic rubidium. Measurement science and technology, 19(10):105601, 2008.

[47] William N Plick and Mario Krenn. Physical meaning of the radial index of laguerre-gauss beams. Physical Review A, 92(6):063841, 2015.

[48] Xavier Baillard, Alexandre Gauguet, Sébastien Bize, Pierre Lemonde, Ph Laurent, André Clairon, and Peter Rosenbusch. Interference-filter-stabilized external-cavity diode lasers. Optics Communications, 266(2):609–613, 2006.

[49] Isidoro Kimel and Luis R Elias. Relations between hermite and laguerre gaussian modes. IEEE Journal of quantum electronics, 29(9):2562–2567, 1993.

[50] Kevin C. Cox, Graham P. Greve, Baochen Wu, and James K. Thompson. Spatially homogeneous entanglement for matter-wave interferometry created with time-averaged measurements. Phys. Rev. A, 94:061601, Dec 2016.

[51] Qian Lin, Mackenzie A. Van Camp, Hao Zhang, Branislav Jelenković, and Vladan Vuletić. Long-external-cavity distributed bragg reflector laser with subkilohertz intrinsic linewidth. Opt. Lett., 37(11):1989–1991, Jun 2012.

[52] Megan Yamoah, Boris Braverman, Edwin Pedrozo-Pe nafiel, Akio Kawasaki, Bojan Zlatković, and Vladan Vuletić. Robust khz-linewidth distributed bragg reflector laser with optoelectronic feedback. Opt. Express, 27(26):37714–37720, Dec 2019.

[53] Travis C. Briles, Dylan C. Yost, Arman Cingöz, Jun Ye, and Thomas R. Schibli. Simple piezoelectric-actuated mirror with 180 khz servo bandwidth. Opt. Express, 18(10):9739–9746, May 2010.

[54] Zilong Chen, Justin G. Bohnet, Joshua M. Weiner, and James K. Thompson. A low phase noise microwave source for atomic spin squeezing experiments in ^{87}Rb. Review of Scientific Instruments, 83(4):044701, 2012.

[55] Vladan Vuletić, Cheng Chin, Andrew J. Kerman, and Steven Chu. Degenerate raman sideband cooling of trapped cesium atoms at very high atomic densities. Phys. Rev. Lett., 81:5768–5771, Dec 1998.

[56] F. Riehle, Th. Kisters, A. Witte, J. Helmcke, and Ch. J. Bordé. Optical ramsey spectroscopy in a rotating frame: Sagnac effect in a matter-wave interferometer. Phys. Rev. Lett., 67:177–180, Jul 1991.

[57] Chengyi Luo, Jiahao Huang, Xiangdong Zhang, and Chaohong Lee. Heisenberg-limited sagnac interferometer with multiparticle states. Phys. Rev. A, 95:023608, Feb 2017.

[58] D. O. Sabulsky, I. Dutta, E. A. Hinds, B. Elder, C. Burrage, and Edmund J. Copeland. Experiment to detect dark energy forces using atom interferometry. Phys. Rev. Lett., 123:061102, Aug 2019.

[59] Y. Bidel, N. Zahzam, C. Blanchard, A. Bonnin, M. Cadoret, A. Bresson, D. Rouxel, and M. F. Lequentrec-Lalancette. Absolute marine gravimetry with matter-wave interferometry. Nature Comm., 9:627, 2018.

[60] G. Rosi, G. D'Amico, L. Cacciapuoti, F. Sorrentino, M. Prevedelli, M. Zych, Č Brukner, and G. M. Tino. Quantum test of the equivalence principle for atoms in coherent superposition of internal energy states. Nature Communications, 8(1):15529, Jun 2017.

[61] Peter Asenbaum, Chris Overstreet, Minjeong Kim, Joseph Curti, and Mark A. Kasevich. Atom-interferometric test of the equivalence principle at the 10^{-12} level. Phys. Rev. Lett., 125:191101, Nov 2020.

[62] Peter Asenbaum, Chris Overstreet, Tim Kovachy, Daniel D. Brown, Jason M. Hogan, and Mark A. Kasevich. Phase shift in an atom interferometer due to spacetime curvature across its wave function. Phys. Rev. Lett., 118:183602, May 2017.

[63] Peter W. Graham, Jason M. Hogan, Mark A. Kasevich, and Surjeet Rajendran. New method for gravitational wave detection with atomic sensors. Phys. Rev. Lett., 110:171102, Apr 2013.

[64] B Canuel, A Bertoldi, L Amand, E Pozzo Di Borgo, T Chantrait, C Danquigny, M Dovale Álvarez, B Fang, Andreas Freise, R Geiger, et al. Exploring gravity with the miga large scale atom interferometer. Scientific Reports, 8(1):14064, Sep 2018.

[65] Robert Bücker, Julian Grond, Stephanie Manz, Tarik Berrada, Thomas Betz, Christian Koller, Ulrich Hohenester, Thorsten Schumm, Aurélien Perrin, and Jörg Schmiedmayer. Twin-atom beams. Nature Physics, 7(8):608–611, 2011.

[66] Chris D. Hamley, C. S. Gerving, T. M. Hoang, E. M. Bookjans, and Michael S. Chapman. Spin-nematic squeezed vacuum in a quantum gas. Nature Physics, 8(4):305–308, February 2012.

[67] Xin-Yu Luo, Yi-Quan Zou, Ling-Na Wu, Qi Liu, Ming-Fei Han, Meng Khoon Tey, and Li You. Deterministic entanglement generation from driving through quantum phase transitions. Science, 355(6325):620–623, 2017.

[68] Karsten Lange, Jan Peise, Bernd Lücke, Ilka Kruse, Giuseppe Vitagliano, Iagoba Apellaniz, Matthias Kleinmann, Géza Tóth, and Carsten Klempt. Entanglement between two spatially separated atomic modes. Science, 360(6387):416–418, 2018.

[69] Matteo Fadel, Tilman Zibold, Boris Décamps, and Philipp Treutlein. Spatial entanglement patterns and einstein-podolsky-rosen steering in bose-einstein condensates. Science, 360(6387):409–413, 2018.

[70] Dietrich Leibfried, Emanuel Knill, Signe Seidelin, Joe Britton, R Brad Blakestad, John Chiaverini, David B Hume, Wayne M Itano, John D Jost, Christopher Langer, et al. Creation of a six-atom 'schrödinger cat' state. Nature, 438(7068):639–642, 2005.

[71] F. Anders, A. Idel, P. Feldmann, D. Bondarenko, S. Loriani, K. Lange, J. Peise, M. Gersemann, B. Meyer-Hoppe, S. Abend, N. Gaaloul, C. Schubert, D. Schlippert, L. Santos, E. Rasel, and C. Klempt. Momentum entanglement for atom interferometry. Phys. Rev. Lett., 127:140402, Sep 2021.

[72] Zilong Chen, Justin G. Bohnet, Shannon R. Sankar, Jiayan Dai, and James K. Thompson. Conditional spin squeezing of a large ensemble via the vacuum Rabi splitting. Phys. Rev. Lett., 106(13):133601–133604, Mar 2011.

[73] Ian D. Leroux, Monika H. Schleier-Smith, and Vladan Vuletić. Implementation of cavity squeezing of a collective atomic spin. Phys. Rev. Lett., 104:073602, Feb 2010.

[74] Monika H. Schleier-Smith, Ian D. Leroux, and Vladan Vuletić. Squeezing the collective spin of a dilute atomic ensemble by cavity feedback. Phys. Rev. A, 81:021804, Feb 2010.

[75] O. Hosten, R. Krishnakumar, N. J. Engelsen, and M. A. Kasevich. Quantum phase magnification. Science, 352(6293):1552–1555, 2016.

[76] Edwin Pedrozo-Peñafiel, Simone Colombo, Chi Shu, Albert F. Adiyatullin, Zeyang Li, Enrique Mendez, Boris Braverman, Akio Kawasaki, Daisuke Akamatsu, Yanhong Xiao, and Vladan Vuletić. Entanglement on an optical atomic-clock transition. Nature, 588(7838):414–418, Dec 2020.

[77] Benjamin K. Malia, Julián Martínez-Rincón, Yunfan Wu, Onur Hosten, and Mark A. Kasevich. Free space ramsey spectroscopy in rubidium with noise below the quantum projection limit. Phys. Rev. Lett., 125:043202, Jul 2020.

[78] Ian D. Leroux, Monika H. Schleier-Smith, and Vladan Vuletić. Orientation-dependent entanglement lifetime in a squeezed atomic clock. Phys. Rev. Lett., 104:250801, Jun 2010.

[79] Boris Braverman, Akio Kawasaki, Edwin Pedrozo-Peñafiel, Simone Colombo, Chi Shu, Zeyang Li, Enrique Mendez, Megan Yamoah, Leonardo Salvi, Daisuke Akamatsu, Yanhong Xiao, and Vladan Vuletić. Near-unitary spin squeezing in ^{171}Yb. Phys. Rev. Lett., 122:223203, Jun 2019.

[80] J Borregaard, E J Davis, G S Bentsen, M H Schleier-Smith, and A S Sørensen. One- and two-axis squeezing of atomic ensembles in optical cavities. New Journal of Physics, 19(9):093021, sep 2017.

[81] Paul Hamilton, Matt Jaffe, Justin M. Brown, Lothar Maisenbacher, Brian Estey, and Holger Müller. Atom interferometry in an optical cavity. Phys. Rev. Lett., 114:100405, Mar 2015.

[82] Victoria Xu, Matt Jaffe, Cristian D. Panda, Sofus L. Kristensen, Logan W. Clark, and Holger Müller. Probing gravity by holding atoms for 20 seconds. Science, 366(6466):745–749, 2019.

[83] Alexander D. Cronin, Jörg Schmiedmayer, and David E. Pritchard. Optics and interferometry with atoms and molecules. Rev. Mod. Phys., 81:1051–1129, Jul 2009.

[84] Mark Kasevich, David S. Weiss, Erling Riis, Kathryn Moler, Steven Kasapi, and Steven Chu. Atomic velocity selection using stimulated raman transitions. Phys. Rev. Lett., 66:2297–2300, May 1991.

[85] Richard P Feynman, Frank L Vernon Jr, and Robert W Hellwarth. Geometrical representation of the schrödinger equation for solving maser problems. Journal of applied physics, 28(1):49–52, 1957.

[86] Yan-Lei Zhang, Chang-Ling Zou, Xu-Bo Zou, Liang Jiang, and Guang-Can Guo. Detuning-enhanced cavity spin squeezing. Phys. Rev. A, 91:033625, Mar 2015.

[87] Ying-Ju Wang, Dana Z. Anderson, Victor M. Bright, Eric A. Cornell, Quentin Diot, Tetsuo Kishimoto, Mara Prentiss, R. A. Saravanan, Stephen R. Segal, and Saijun Wu. Atom michelson interferometer on a chip using a bose-einstein condensate. Phys. Rev. Lett., 94:090405, Mar 2005.

[88] G.-B. Jo, Y. Shin, S. Will, T. A. Pasquini, M. Saba, W. Ketterle, D. E. Pritchard, M. Vengalattore, and M. Prentiss. Long phase coherence time and number squeezing of two bose-einstein condensates on an atom chip. Phys. Rev. Lett., 98:030407, Jan 2007.

[89] Martina Gebbe, Jan-Niclas Siemß, Matthias Gersemann, Hauke Müntinga, Sven Herrmann, Claus Lämmerzahl, Holger Ahlers, Naceur Gaaloul, Christian Schubert, Klemens Hammerer, Sven Abend, and Ernst M. Rasel. Twin-lattice atom interferometry. Nature Communications, 12(1):2544, May 2021.

[90] J. G. Bohnet, K. C Cox, M. A. Norcia, J. M. Weiner, Z. Chen, and J. K. Thompson. Reduced spin measurement back-action for a phase sensitivity ten times beyond the standard quantum limit. Nature Photon., 8:731–736, July 2014.

[91] Matt Jaffe, Philipp Haslinger, Victoria Xu, Paul Hamilton, Amol Upadhye, Benjamin Elder, Justin Khoury, and Holger Müller. Testing sub-gravitational forces on atoms from a miniature in-vacuum source mass. Nature Physics, 13(10):938–942, 2017.

[92] Ronen M. Kroeze, Yudan Guo, and Benjamin L. Lev. Dynamical spin-orbit coupling of a quantum gas. Phys. Rev. Lett., 123:160404, Oct 2019.

[93] M. Landini, N. Dogra, K. Kroeger, L. Hruby, T. Donner, and T. Esslinger. Formation of a spin texture in a quantum gas coupled to a cavity. Phys. Rev. Lett., 120:223602, May 2018.

[94] Hans Keßler, Phatthamon Kongkhambut, Christoph Georges, Ludwig Mathey, Jayson G. Cosme, and Andreas Hemmerich. Observation of a dissipative time crystal. Phys. Rev. Lett., 127:043602, Jul 2021.

[95] S. C. Schuster, P. Wolf, S. Ostermann, S. Slama, and C. Zimmermann. Supersolid properties of a bose-einstein condensate in a ring resonator. Phys. Rev. Lett., 124:143602, Apr 2020.

[96] Brian Skinner, Jonathan Ruhman, and Adam Nahum. Measurement-induced phase transitions in the dynamics of entanglement. Phys. Rev. X, 9:031009, Jul 2019.

[97] Emily J. Davis, Gregory Bentsen, Lukas Homeier, Tracy Li, and Monika H. Schleier-Smith. Photon-mediated spin-exchange dynamics of spin-1 atoms. Phys. Rev. Lett., 122:010405, Jan 2019.

[98] Matthew A Norcia, Robert J Lewis-Swan, Julia RK Cline, Bihui Zhu, Ana M Rey, and James K Thompson. Cavity-mediated collective spin-exchange interactions in a strontium superradiant laser. Science, 361(6399):259–262, 2018.

[99] Juan A Muniz, Diego Barberena, Robert J Lewis-Swan, Dylan J Young, Julia RK Cline, Ana Maria Rey, and James K Thompson. Exploring dynamical phase transitions with cold atoms in an optical cavity. Nature, 580(7805):602–607, 2020.

[100] Nick Sauerwein, Francesca Orsi, Philipp Uhrich, Soumik Bandyopadhyay, Francesco Mattiotti, Tigrane Cantat-Moltrecht, Guido Pupillo, Philipp Hauke, and Jean-Philippe Brantut. Engineering random spin models with atoms in a high-finesse cavity. Nature Physics, 19:1128–1134, 2023.

[101] Adam T Black, Hilton W Chan, and Vladan Vuletić. Observation of collective friction forces due to spatial self-organization of atoms: from rayleigh to bragg scattering. Physical Review Letters, 91(20):203001, 2003.

[102] Kristian Baumann, Christine Guerlin, Ferdinand Brennecke, and Tilman Esslinger. Dicke quantum phase transition with a superfluid gas in an optical cavity. Nature, 464(7293):1301–1306, 2010.

[103] SC Schuster, P Wolf, S Ostermann, S Slama, and C Zimmermann. Supersolid properties of a bose-einstein condensate in a ring resonator. Physical Review Letters, 124(14):143602, 2020.

[104] Yudan Guo, Ronen M Kroeze, Brendan P Marsh, Sarang Gopalakrishnan, Jonathan Keeling, and Benjamin L Lev. An optical lattice with sound. Nature, 599(7884):211–215, 2021.

[105] Phatthamon Kongkhambut, Jim Skulte, Ludwig Mathey, Jayson G Cosme, Andreas Hemmerich, and Hans Keßler. Observation of a continuous time crystal. Science, 377(6606):670–673, 2022.

[106] Ronen M Kroeze, Yudan Guo, Varun D Vaidya, Jonathan Keeling, and Benjamin L Lev. Spinor self-ordering of a quantum gas in a cavity. Physical Review Letters, 121(16):163601, 2018.

[107] Kevin C Cox, Graham P Greve, Joshua M Weiner, and James K Thompson. Deterministic squeezed states with collective measurements and feedback. Physical Review Letters, 116(9):093602, 2016.

[108] John M Robinson, Maya Miklos, Yee Ming Tso, Colin J Kennedy, Tobias Bothwell, Dhruv Kedar, James K Thompson, and Jun Ye. Direct comparison of two spin-squeezed optical clock ensembles at the 10- 17 level, 2024.

[109] D. Kruse, C. von Cube, C. Zimmermann, and Ph. W. Courteille. Observation of lasing mediated by collective atomic recoil. Phys. Rev. Lett., 91:183601, Oct 2003.

[110] Ferdinand Brennecke, Stephan Ritter, Tobias Donner, and Tilman Esslinger. Cavity optomechanics with a bose-einstein condensate. Science, 322(5899):235–238, 2008.

[111] Matthias Wolke, Julian Klinner, Hans Keßler, and Andreas Hemmerich. Cavity cooling below the recoil limit. Science, 337(6090):75–78, 2012.

[112] H Keßler, J Klinder, M Wolke, and A Hemmerich. Optomechanical atom-cavity interaction in the sub-recoil regime. New Journal of Physics, 16(5):053008, may 2014.

[113] Nicolas Spethmann, Jonathan Kohler, Sydney Schreppler, Lukas Buchmann, and Dan M Stamper-Kurn. Cavity-mediated coupling of mechanical oscillators limited by quantum backaction. Nature Physics, 12(1):27–31, 2016.

[114] Rodrigo A Thomas, Michał Parniak, Christoffer Østfeldt, Christoffer B Møller, Christian Bærentsen, Yeghishe Tsaturyan, Albert Schliesser, Jürgen Appel, Emil Zeuthen, and Eugene S Polzik. Entanglement between distant macroscopic mechanical and spin systems. Nature Physics, 17(2):228–233, 2021.

[115] RD Delaney, MD Urmey, S Mittal, BM Brubaker, JM Kindem, PS Burns, CA Regal, and KW Lehnert. Superconducting-qubit readout via low-backaction electro-optic transduction. Nature, 606(7914):489–493, 2022.

[116] Emily J Davis, Avikar Periwal, Eric S Cooper, Gregory Bentsen, Simon J Evered, Katherine Van Kirk, and Monika H Schleier-Smith. Protecting spin coherence in a tunable heisenberg model. Physical Review Letters, 125(6):060402, 2020.

[117] Athreya Shankar, Leonardo Salvi, Maria Luisa Chiofalo, Nicola Poli, and Murray J Holland. Squeezed state metrology with bragg interferometers operating in a cavity. Quantum Science and Technology, 4(4):045010, oct 2019.

[118] John Drew Wilson, Simon B. Jäger, Jarrod T. Reilly, Athreya Shankar, Maria Luisa Chiofalo, and Murray J. Holland. Beyond one-axis twisting: Simultaneous spin-momentum squeezing. Phys. Rev. A, 106:043711, Oct 2022.

[119] Jamir Marino, Martin Eckstein, Matthew S. Foster, and Ana Maria Rey. Dynamical phase transitions in the collisionless pre-thermal states of isolated quantum systems: theory and experiments. Reports on Progress in Physics, 85(11):116001, 2022.

[120] RW Richardson and Noah Sherman. Exact eigenstates of the pairing-force hamiltonian. Nuclear Physics, 52:221–238, 1964.

[121] RW Richardson and Noah Sherman. Pairing models of pb206, pb204 and pb202. Nuclear Physics, 52:253–268, 1964.

[122] Fabian Finger, Rodrigo Rosa-Medina, Nicola Reiter, Panagiotis Christodoulou, Tobias Donner, and Tilman Esslinger. Spin- and momentum-correlated atom pairs mediated by photon exchange and seeded by vacuum fluctuations. Phys. Rev. Lett., 132:093402, Feb 2024.

[123] Robert V Pound and Glen A Rebka Jr. Apparent weight of photons. Physical Review Letters, 4(7):337, 1960.

[124] Tobias Bothwell, Colin J Kennedy, Alexander Aeppli, Dhruv Kedar, John M Robinson, Eric Oelker, Alexander Staron, and Jun Ye. Resolving the gravitational redshift across a millimetre-scale atomic sample. Nature, 602(7897):420–424, 2022.

[125] Kevin C. Cox, Graham P. Greve, Baochen Wu, and James K. Thompson. Spatially homogeneous entanglement for matter-wave interferometry created with time-averaged measurements. Phys. Rev. A, 94:061601, Dec 2016.

[126] Johannes Borregaard, EJ Davis, Greg S Bentsen, Monika H Schleier-Smith, and Anders S Sørensen. One-and two-axis squeezing of atomic ensembles in optical cavities. New Journal of Physics, 19(9):093021, 2017.

[127] Adam T. Black, James K. Thompson, and Vladan Vuletić. On-demand superradiant conversion of atomic spin gratings into single photons with high efficiency. Phys. Rev. Lett., 95:133601, Sep 2005.

[128] Robert J. Lewis-Swan, Diego Barberena, Julia R. K. Cline, Dylan J. Young, James K. Thompson, and Ana Maria Rey. Cavity-qed quantum simulator of dynamical phases of a bardeen-cooper-schrieffer superconductor. Phys. Rev. Lett., 126:173601, Apr 2021.

[129] Scott Smale, Peiru He, Ben A Olsen, Kenneth G Jackson, Haille Sharum, Stefan Trotzky, Jamir Marino, Ana Maria Rey, and Joseph H Thywissen. Observation of a transition between dynamical phases in a quantum degenerate fermi gas. Science advances, 5(8):eaax1568, 2019.

[130] Fangzhao Alex An, Eric J. Meier, Jackson Ang'ong'a, and Bryce Gadway. Correlated dynamics in a synthetic lattice of momentum states. Phys. Rev. Lett., 120:040407, Jan 2018.

[131] Eric J. Meier, Fangzhao Alex An, Alexandre Dauphin, Maria Maffei, Pietro Massignan, Taylor L. Hughes, and Bryce Gadway. Observation of the topological anderson insulator in disordered atomic wires. Science, 362(6417):929–933, 2018.

[132] A. Celi, P. Massignan, J. Ruseckas, N. Goldman, I. B. Spielman, G. Juzeliūnas, and M. Lewenstein. Synthetic gauge fields in synthetic dimensions. Phys. Rev. Lett., 112:043001, Jan 2014.

[133] Thomas Chalopin, Tanish Satoor, Alexandre Evrard, Vasiliy Makhalov, Jean Dalibard, Raphael Lopes, and Sylvain Nascimbene. Probing chiral edge dynamics and bulk topology of a synthetic hall system. Nature Physics, 16(10):1017–1021, 2020.

[134] B. K. Stuhl, H. I. Lu, L. M. Aycock, D. Genkina, and I. B. Spielman. Visualizing edge states with an atomic bose gas in the quantum hall regime. Science, 349(6255):1514–1518, 2015.

[135] S. Kolkowitz, S. L. Bromley, T. Bothwell, M. L. Wall, G. E. Marti, A. P. Koller, X. Zhang, A. M. Rey, and J. Ye. Spin–orbit-coupled fermions in an optical lattice clock. Nature, 542(7639):66–70, 2017.

[136] M. Mancini, G. Pagano, G. Cappellini, L. Livi, M. Rider, J. Catani, C. Sias, P. Zoller, M. Inguscio, M. Dalmonte, and L. Fallani. Observation of chiral edge states with neutral fermions in synthetic hall ribbons. Science, 349(6255):1510–1513, 2015.

[137] Farokh Mivehvar, Helmut Ritsch, and Francesco Piazza. Cavity-quantum-electrodynamical toolbox for quantum magnetism. Phys. Rev. Lett., 122:113603, Mar 2019.

[138] Farokh Mivehvar, Francesco Piazza, Tobias Donner, and Helmut Ritsch. Cavity qed with quantum gases: new paradigms in many-body physics. Advances in Physics, 70(1):1–153, 2021.

[139] Titas Chanda, Rebecca Kraus, Giovanna Morigi, and Jakub Zakrzewski. Self-organized topological insulator due to cavity-mediated correlated tunneling. Quantum, 5:501, July 2021.

[140] Ruichao Ma, M. Eric Tai, Philipp M. Preiss, Waseem S. Bakr, Jonathan Simon, and Markus Greiner. Photon-assisted tunneling in a biased strongly correlated bose gas. Phys. Rev. Lett., 107:095301, Aug 2011.

[141] F. Meinert, M. J. Mark, K. Lauber, A. J. Daley, and H.-C. Nägerl. Floquet engineering of correlated tunneling in the bose-hubbard model with ultracold atoms. Phys. Rev. Lett., 116:205301, May 2016.

[142] Wenchao Xu, William Morong, Hoi-Yin Hui, Vito W. Scarola, and Brian DeMarco. Correlated spin-flip tunneling in a fermi lattice gas. Phys. Rev. A, 98:023623, Aug 2018.

[143] Bernd Lücke, Manuel Scherer, Jens Kruse, Luca Pezzé, Frank Deuretzbacher, Phillip Hyllus, Jan Peise, Wolfgang Ertmer, Jan Arlt, Luis Santos, Augusto Smerzi, and Carston Klempt. Twin matter waves for interferometry beyond the classical limit. Science, 334(6057):773–776, 2011.

[144] Christian Gross. Spin squeezing, entanglement and quantum metrology with bose–einstein condensates. J. Phys. B: At. Mol. Opt. Phys., 45(10):103001, 2012.

[145] Stuart J. Masson, M. D. Barrett, and Scott Parkins. Cavity qed engineering of spin dynamics and squeezing in a spinor gas. Phys. Rev. Lett., 119:213601, Nov 2017.

[146] Avikar Periwal, Eric S Cooper, Philipp Kunkel, Julian F Wienand, Emily J Davis, and Monika Schleier-Smith. Programmable interactions and emergent geometry in an array of atom clouds. Nature, 600(7890):630–635, 2021.

[147] Christina V. Kraus, Marcello Dalmonte, Mikhail A. Baranov, Andreas M. Läuchli, and P. Zoller. Majorana edge states in atomic wires coupled by pair hopping. Phys. Rev. Lett., 111:173004, Oct 2013.

[148] W. Zheng and N. R. Cooper. Superradiance induced particle flow via dynamical gauge coupling. Phys. Rev. Lett., 117:175302, Oct 2016.

[149] Christian Schweizer, Fabian Grusdt, Moritz Berngruber, Luca Barbiero, Eugene Demler, Nathan Goldman, Immanuel Bloch, and Monika Aidelsburger. Floquet approach to z2 lattice gauge theories with ultracold atoms in optical lattices. Nature Physics, 15(11):1168–1173, 2019.

[150] Elvia Colella, Arkadiusz Kosior, Farokh Mivehvar, and Helmut Ritsch. Open quantum system simulation of faraday's induction law via dynamical instabilities. Phys. Rev. Lett., 128:070603, Feb 2022.

[151] Rodrigo Rosa-Medina, Francesco Ferri, Fabian Finger, Nishant Dogra, Katrin Kroeger, Rui Lin, R. Chitra, Tobias Donner, and Tilman Esslinger. Observing dynamical currents in a non-hermitian momentum lattice. Phys. Rev. Lett., 128:143602, Apr 2022.

[152] Haoqing Zhang, Anjun Chu, Chengyi Luo, James K. Thompson, and Ana Maria Rey. Control and amplification of bloch oscillations via photon-mediated interactions. Phys. Rev. Res., 5:L032039, Sep 2023.

[153] Athreya Shankar, Graham P Greve, Baochen Wu, James K Thompson, and Murray Holland. Continuous real-time tracking of a quantum phase below the standard quantum limit. Physical Review Letters, 122(23):233602, 2019.

[154] Antoine Browaeys and Thierry Lahaye. Many-body physics with individually controlled rydberg atoms. Nature Physics, 16(2):132–142, 2020.

[155] Sebastian Geier, Nithiwadee Thaicharoen, Clément Hainaut, Titus Franz, Andre Salzinger, Annika Tebben, David Grimshandl, Gerhard Zürn, and Matthias Weidemüller. Floquet hamiltonian engineering of an isolated many-body spin system. Science, 374(6571):1149–1152, 2021.

[156] Xiaoling Wu, Xinhui Liang, Yaoqi Tian, Fan Yang, Cheng Chen, Yong-Chun Liu, Meng Khoon Tey, and Li You. A concise review of rydberg atom based quantum computation and quantum simulation. Chinese Physics B, 30(2):020305, 2021.

[157] John L. Bohn, Ana Maria Rey, and Jun Ye. Cold molecules: Progress in quantum engineering of chemistry and quantum matter. Science, 357(6355):1002–1010, 2017.

[158] Jun-Ru Li, Kyle Matsuda, Calder Miller, Annette N Carroll, William G Tobias, Jacob S Higgins, and Jun Ye. Tunable itinerant spin dynamics with polar molecules. Nature, 614(7946):70–74, 2023.

[159] Jiehang Zhang, Paul W Hess, A Kyprianidis, Petra Becker, A Lee, J Smith, Gaetano Pagano, I-D Potirniche, Andrew C Potter, Ashvin Vishwanath, et al. Observation of a discrete time crystal. Nature, 543(7644):217–220, 2017.

[160] C. Monroe, W. C. Campbell, L.-M. Duan, Z.-X. Gong, A. V. Gorshkov, P. W. Hess, R. Islam, K. Kim, N. M. Linke, G. Pagano, P. Richerme, C. Senko, and N. Y. Yao. Programmable quantum simulations of spin systems with trapped ions. Rev. Mod. Phys., 93:025001, Apr 2021.

[161] Joonhee Choi, Hengyun Zhou, Helena S. Knowles, Renate Landig, Soonwon Choi, and Mikhail D. Lukin. Robust dynamic hamiltonian engineering of many-body spin systems. Phys. Rev. X, 10:031002, Jul 2020.

[162] Joseph H.D. Munns, Laura Orphal-Kobin, Gregor Pieplow, and Tim Schröder. Quantum Optics with Solid-State Color Centers, chapter 19, pages 509–562. John Wiley & Sons, Ltd, 2023.

[163] Immanuel Bloch, Jean Dalibard, and Wilhelm Zwerger. Many-body physics with ultracold gases. Rev. Mod. Phys., 80:885–964, Jul 2008.

[164] Florian Schäfer, Takeshi Fukuhara, Seiji Sugawa, Yosuke Takasu, and Yoshiro Takahashi. Tools for quantum simulation with ultracold atoms in optical lattices. Nature Reviews Physics, 2(8):411–425, 2020.

[165] Christian Gross and Immanuel Bloch. Quantum simulations with ultracold atoms in optical lattices. Science, 357(6355):995–1001, 2017.

[166] Lea-Marina Steinert, Philip Osterholz, Robin Eberhard, Lorenzo Festa, Nikolaus Lorenz, Zaijun Chen, Arno Trautmann, and Christian Gross. Spatially tunable spin interactions in neutral atom arrays. Phys. Rev. Lett., 130:243001, Jun 2023.

[167] Masataka Shirasaki and Hermann A Haus. Squeezing of pulses in a nonlinear interferometer. JOSA B, 7(1):30–34, 1990.

[168] Jan Benhelm, Gerhard Kirchmair, Christian F Roos, and Rainer Blatt. Towards fault-tolerant quantum computing with trapped ions. Nature Physics, 4(6):463–466, 2008.

[169] Nikolay Kalinin, Thomas Dirmeier, Arseny A Sorokin, Elena A Anashkina, Luis L Sánchez-Soto, Joel F Corney, Gerd Leuchs, and Alexey V Andrianov. Quantum-enhanced interferometer using kerr squeezing. Nanophotonics, (0), 2023.

[170] W. Muessel, H. Strobel, D. Linnemann, T. Zibold, B. Juliá-Díaz, and M. K. Oberthaler. Twist-and-turn spin squeezing in bose-einstein condensates. Phys. Rev. A, 92:023603, Aug 2015.

[171] Souma Chaudhury, Seth Merkel, Tobias Herr, Andrew Silberfarb, Ivan H. Deutsch, and Poul S. Jessen. Quantum control of the hyperfine spin of a cs atom ensemble. Phys. Rev. Lett., 99:163002, Oct 2007.

[172] Zeyang Li, Simone Colombo, Chi Shu, Gustavo Velez, Saúl Pilatowsky-Cameo, Roman Schmied, Soonwon Choi, Mikhail Lukin, Edwin Pedrozo-Peñafiel, and Vladan Vuletić. Improving metrology with quantum scrambling. Science, 380(6652):1381–1384, 2023.

[173] J Borregaard, E J Davis, G S Bentsen, M H Schleier-Smith, and A S Sørensen. One- and two-axis squeezing of atomic ensembles in optical cavities. New Journal of Physics, 19(9):093021, sep 2017.

[174] Yong-Chang Zhang, Xiang-Fa Zhou, Xingxiang Zhou, Guang-Can Guo, and Zheng-Wei Zhou. Cavity-assisted single-mode and two-mode spin-squeezed states via phase-locked atom-photon coupling. Physical Review Letters, 118(8):083604, 2017.

[175] David M. Giltner, Roger W. McGowan, and Siu Au Lee. Atom interferometer based on bragg scattering from standing light waves. Phys. Rev. Lett., 75:2638–2641, Oct 1995.

[176] W. Wasilewski, K. Jensen, H. Krauter, J. J. Renema, M. V. Balabas, and E. S. Polzik. Quantum noise limited and entanglement-assisted magnetometry. Phys. Rev. Lett., 104:133601, Mar 2010.

[177] M. Koschorreck, M. Napolitano, B. Dubost, and M. W. Mitchell. Sub-projection-noise sensitivity in broadband atomic magnetometry. Phys. Rev. Lett., 104:093602, Mar 2010.

[178] W. Muessel, H. Strobel, D. Linnemann, D. B. Hume, and M. K. Oberthaler. Scalable spin squeezing for quantum-enhanced magnetometry with bose-einstein condensates. Phys. Rev. Lett., 113:103004, Sep 2014.

[179] WF McGrew, X Zhang, RJ Fasano, SA Schäffer, K Beloy, D Nicolodi, RC Brown, N Hinkley, G Milani, M Schioppo, et al. Atomic clock performance enabling geodesy below the centimetre level. Nature, 564(7734):87–90, 2018.

[180] Manuel H. Muñoz Arias, Ivan H. Deutsch, and Pablo M. Poggi. Phase-space geometry and optimal state preparation in quantum metrology with collective spins. PRX Quantum, 4:020314, Apr 2023.

[181] Dariusz Kajtoch and Emilia Witkowska. Quantum dynamics generated by the two-axis countertwisting hamiltonian. Phys. Rev. A, 92:013623, Jul 2015.

[182] Zilong Chen, Justin G. Bohnet, Joshua M. Weiner, and James K. Thompson. General formalism for evaluating the impact of phase noise on bloch vector rotations. Phys. Rev. A, 86:032313, Sep 2012.

[183] Fangzhao Alex An, Bhuvanesh Sundar, Junpeng Hou, Xi-Wang Luo, Eric J Meier, Chuanwei Zhang, Kaden RA Hazzard, and Bryce Gadway. Nonlinear dynamics in a synthetic momentum-state lattice. Physical Review Letters, 127(13):130401, 2021.

[184] Julian Léonard, Andrea Morales, Philip Zupancic, Tilman Esslinger, and Tobias Donner. Supersolid formation in a quantum gas breaking a continuous translational symmetry. Nature, 543(7643):87–90, 2017.

[185] Julian Léonard, Andrea Morales, Philip Zupancic, Tobias Donner, and Tilman Esslinger. Monitoring and manipulating higgs and goldstone modes in a supersolid quantum gas. Science, 358(6369):1415–1418, 2017.

[186] Helmut Ritsch, Peter Domokos, Ferdinand Brennecke, and Tilman Esslinger. Cold atoms in cavity-generated dynamical optical potentials. Rev. Mod. Phys., 85:553–601, Apr 2013.

[187] Andrei Isichenko, Nitesh Chauhan, Kaikai Liu, Mark W Harrington, and Daniel J Blumenthal. Chip-scale, sub-hz fundamental sub-khz integral linewidth 780 nm laser through self-injection-locking a fabry-perot laser to an ultra-high q integrated resonator. arXiv preprint arXiv:2307.04947, 2023.

[188] Emanuele G. Dalla Torre, Johannes Otterbach, Eugene Demler, Vladan Vuletic, and Mikhail D. Lukin. Dissipative preparation of spin squeezed atomic ensembles in a steady state. Phys. Rev. Lett., 110:120402, Mar 2013.

[189] Peter Groszkowski, Martin Koppenhöfer, Hoi-Kwan Lau, and A. A. Clerk. Reservoir-engineered spin squeezing: Macroscopic even-odd effects and hybrid-systems implementations. Phys. Rev. X, 12:011015, Jan 2022.

[190] Diego Barberena and Ana Maria Rey. Critical steady states of all-to-all driven-dissipative models: An analytic approach. arXiv preprint arXiv:2307.05115, 2023.

[191] Leonardo Salvi, Nicola Poli, Vladan Vuletić, and Guglielmo M. Tino. Squeezing on momentum states for atom interferometry. Phys. Rev. Lett., 120:033601, Jan 2018.

[192] Xuanchen Zhang, Zhiyao Hu, and Yong-Chun Liu. Fast generation of ghz-like states using collective-spin XYZ model. Phys. Rev. Lett., 132:113402, Mar 2024.

[193] O Băzăvan, S Saner, DJ Webb, EM Ainley, P Drmota, DP Nadlinger, G Araneda, DM Lucas, CJ Ballance, and R Srinivas. Squeezing, trisqueezing, and quadsqueezing in a spin-oscillator system. arXiv preprint arXiv:2403.05471, 2024.